

Dissertation
submitted to the
Combined Faculties of the Natural Sciences and Mathematics
of the Ruperto–Carola–University of Heidelberg, Germany
for the degree of
Doctor of Natural Sciences

Put forward by
Giovanni Natale
born in: Caserta, Italy
Oral examination: 16th July, 2010

Dust emission and Star formation in the
Stephan's Quintet compact group of
galaxies

Referees: Prof. Werner Hofmann

Prof. Francois Boulanger

Supervisor: Dr. Richard Tuffs

Abstract

Understanding the intergalactic medium (IGM) gas cooling processes, which are necessary to fuel star formation in galaxies, and the effect of galaxy–galaxy and galaxy–IGM interactions, which modify stellar and gas distributions of galaxies in groups and clusters, is vital to construct realistic models of galaxy formation and evolution. The Stephan’s Quintet (SQ) compact group of galaxies is a natural laboratory for studying these phenomena because the galaxies of this group are heavily interacting between each other and with the group IGM. Furthermore its vicinity allows to study the details of the interaction phenomena, which are believed to be much more common in the early universe, and its compactness on the sky permits studies of diffuse components associated with the group IGM.

In this thesis we present an analysis of a comprehensive set of MIR/FIR observations of Stephan’s Quintet, taken with the Spitzer Space Observatory. The emission seen at these wavelengths is produced by dust particles and can be used to trace star formation events, AGN activity and also hot gas cooling, in the case dust emission is powered by collisions between plasma particles and dust.

Applying a novel fitting technique to the Spitzer FIR maps, we have been able to separate the different sources of dust emission in this group and perform their photometry at FIR as well as MIR wavelengths. Our study has revealed for the first time the presence of a luminous and extended component of infrared dust emission, not connected with the mainbodies of the group galaxies, and roughly coincident with the X-ray halo of the group. We fitted the inferred dust emission spectral energy distribution of this extended source and the other main infrared emission components of SQ, including the intergalactic shock, to elucidate the mechanisms powering the dust and PAH emission, taking into account dust collisional heating and heating through UV and optical photons.

Combining the fraction of dust luminosity powered by UV photons, as derived from the SED fitting, with the UV luminosity directly observed on the GALEX FUV map of SQ, we estimated the star formation rate (SFR) for each dust emit-

ting source, thus providing a complete picture of star formation in SQ embracing obscured and unobscured components. The total SFR of SQ is $7.5 M_{\odot}/\text{yr}$, similar to the value expected for non interacting galaxies of the same mass of SQ galaxies. However the star formation sites are found mainly at the periphery of the galaxies or in the intergalactic medium, at variance with the usual pattern of star formation in field galaxies which is typically distributed in the central regions or main bodies of galaxies. Despite the unusual location of star formation sites, we have found that, for the brightest sources in SQ, the SFR per unit physical area is similar to that characteristic of disk galaxy star formation regions when compared to the corresponding gas column density on a Kennicutt–Schmidt diagram. We also show that even though the detected extended component of dust emission trace the distributed group star formation, available sources of dust in the group halo can provide enough dust to produce up to $L_{IR} \approx 10^{42}$ erg/s powered by collisional heating. This amount, several times higher than the X-ray halo luminosity, could provide an important cooling mechanism for the IGM hot gas.

At the end of the thesis we present a theoretical model of a high velocity shock, similar to the one occurring in SQ IGM, taking into account dust cooling and dust destruction. This model shows that, although the efficiency of dust cooling drops quickly because of dust removal by sputtering, the gas cooling time is reduced by a factor of 2-3, compared to the case where only radiative cooling is considered.

Zusammenfassung

Um realistische Modelle für die Entstehung und Entwicklung von Galaxien zu entwickeln, ist das Verständnis von zwei Dingen notwendig: die Gaskühlungsprozesse des intergalaktischen Mediums (IGM), welche die Sternbildung in Galaxien antreiben, und die Interaktionen zwischen Galaxien und Galaxien und IGM, welche die Stern- und Gasverteilungen von Galaxien in Gruppen und Clustern beeinflussen. Das Stephans Quintett (SQ) ist eine kompakte Gruppe von stark untereinander und mit dem IGM wechselwirkenden Galaxien und daher eine ideale Umgebung für die Untersuchung dieser Prozesse. Seine Kompaktheit am Himmel erlaubt eine Studie der ausgedehnten Komponenten, die dem IGM der Gruppe zugeordnet werden.

Des weiteren erlaubt seine geringe Entfernung eine detaillierte Studie der Wechselwirkungen zwischen Galaxien, von denen man glaubt, dass sie im frühen Universum häufiger waren.

In dieser Arbeit präsentieren wir die Ergebnisse der Untersuchung von Spitzer Space Observatory Aufnahmen des SQ im MIR/FIR Wellenlängenbereich. Die Strahlung in diesen Wellenlängen wird von Staubpartikeln produziert und ist ein Indikator sowohl für Sternentstehung und AGN Aktivitäten, als auch für die Abkühlung von heißem Gas, falls die Strahlung durch Kollisionen der Staubpartikel mit dem Plasma erzeugt wird. Unter Anwendung einer neuen Fit-Technik auf die Spitzer FIR Karten waren wir in der Lage, die verschiedenen Quellen der Staubstrahlung in dieser Gruppe zu isolieren und ihre Photometrie sowohl im FIR als auch im MIR zu erstellen. Diese Untersuchung hat zum ersten Mal das Vorhandensein einer leuchtenden, ausgedehnten Komponente der infraroten Staubemission gezeigt, die nicht direkt mit einer der Galaxien verbunden ist, jedoch grob mit dem Halo der Gruppe im Röntgenlicht zusammenfällt. Wir haben die IR spektrale Energieverteilung (SED) der Staubemission sowohl dieser ausgedehnten Quelle als auch die der anderen Hauptkomponenten des SQ und der intergalaktischen Schockregion gefittet, um dem treibenden Mechanismus hinter der Staub- und PAH-Emission zu ergründen. Dabei wurden Staubaufheizung durch Stöße und durch UV und optische Photonen berücksichtigt.

Unter Verwendung der direkt gemessenen UV-Leuchtkraft aus den GALEX FUV Karten des SQ und dem Bruchteil der Staubemission verursacht durch UV Photons, abgeleitet aus dem SED Fit, konnten wir die Sternentstehungsrate (SFR) der Quellen der Staubemission abschätzen und somit ein vollständiges Bild der Sternentstehung im SQ mithilfe der verdeckten und direkt sichtbaren Komponenten erstellen. Die gesamte SFR des SQ ist $7.5 M_{\odot}/\text{yr}$, vergleichbar mit dem zu erwartenden Wert für nicht wechselwirkende Galaxien von vergleichbarer Masse. Jedoch findet die Sternbildung vor allem in der Peripherie der Galaxien oder im IGM statt, im Gegensatz zu den für Feldgalaxien üblichen inneren Bereichen oder der Kernregion. Trotz dieses ungewöhnlichen Ortes für die Sternbildung stellen wir für die hellsten Quellen im SQ fest, dass die SFR pro physikalischer Fläche vergle-

ichbar ist mit dem entsprechenden Wert einer Scheibengalaxie mit entsprechender Gas-Säulendichte in einem Kennicutt-Schmidt Diagramm. Wir zeigen auch, dass obwohl die detektierte ausgedehnte Komponente der Staubemission der Sternentstehung in der Gruppe folgt, vorhandene Staubquellen im Halo der Gruppe genug Staub zur Verfügung stellen können um eine Leuchtkraft von bis zu $L_{IR} \approx 10^{42}$ erg/s durch Stoß-Aufheizen zu erzeugen. Dieser Betrag, ein Vielfaches der Haloleuchtkraft im Röntgenbereich, könnte einen Kühlmechanismus für das heiße Gas im IGM darstellen.

Am Schluss dieser Arbeit präsentieren wir ein theoretisches Modell eines Hochgeschwindigkeitsschocks, vergleichbar mit dem im IGM des SQ, unter Berücksichtigung der Kühlung durch Staub und der Staubzerstörung. Obwohl die Effizienz der Kühlung durch Staub aufgrund der Verdampfung der Staubkörner schnell sinkt, zeigt dieses Modell dass die benötigte Zeit für die Abkühlung des Gases um einen Faktor 2-3 reduziert wird im Vergleich zu einer Abkühlung ausschließlich durch thermische Strahlung des Gases.

Contents

Foreword	I
1 Introduction	1
1.1 Groups and cluster of galaxies: formation and evolution	1
1.2 The Stephan's Quintet compact group of galaxies	7
1.3 What can we learn from studying the dust emission from SQ?	22
2 SQ Dust Emission: Morphology and Source Photometry	27
2.1 Morphology of dust emission in SQ	27
2.1.1 The FIR map fitting technique and the FIR residual maps . .	30
2.2 SQ Spitzer map photometry	32
2.2.1 Star formation regions and galaxies	36
2.2.2 Shock region	38
2.2.3 Extended FIR emission	42
2.3 Multisource fit of SQ FIR maps	43
2.A Observations and Data Reduction	50
3 Modelling the dust emission SEDs of SQ sources	55
3.1 Modelling the Infrared SEDs	55
3.1.1 Star formation regions	57
3.1.2 AGN galaxy NGC7319	58
3.1.3 Shock region emission	60
3.1.4 Extended emission	65
3.1.5 Foreground galaxy NGC7320	65

3.1.6	Infrared source north of NGC7319 (HII-N)	67
3.2	Dust SED templates and models	67
3.2.1	Dust in PDR/HII regions	70
3.2.2	Dust heated by diffuse radiation fields	70
3.2.3	Dust emission from AGN torus	72
3.2.4	Dust heated by collisions in X-ray plasmas	73
4	Star formation and AGN dust emission in SQ	77
4.1	Introduction	77
4.2	Quantifying star formation rates and gas masses in SQ	78
4.2.1	Star formation rates	78
4.2.2	Gas Masses	83
4.3	Star formation in SQ	84
4.3.1	Discrete Star Formation Regions	86
4.3.2	Star formation associated with the Shock	88
4.3.3	Star Formation associated with the Extended Emission	90
4.4	The AGN galaxy NGC7319 dust emission	93
5	Dust emission from SQ X-ray emitting regions	97
5.1	Introduction	97
5.2	The shock region	98
5.3	The extended emission	101
5.A	Estimate of an upper limit to the dust injection rate from halo stars in SQ	104
5.B	SQ dark matter halo mass	105
6	A shock model with dust cooling	107
6.1	Introduction	107
6.2	The model	108
6.3	Results	111
	Summary and conclusions	119

Future outlook	124
Bibliography	127
Table of abbreviations	135
Future outlook	137

Foreword

The Stephan's Quintet compact group of galaxies was observed for the first time by Edouard Stephan, director of the Marseille Observatory, in the year 1877. In the report of his observations, published in Monthly Notices of the Royal Astronomical Society (MNRAS), one can read the following notes about the set of observed “nebulae”:

“Les quatre nébuleuses 19, 20, 21 et 22 sont excessivement excessivement faibles, excessivement petit, très-difficilement observables. La plus belle est 19, puis viennent 20, 21, 22. Cependant 22, quoique la plus petite des quatre, est plus brillante.”

[Translation: The four nebulae 19, 20, 21 and 22 are extremely faint, extremely small, very difficult to observe. The nicest one is 19, then come 20, 21, 22. Although 22 is the smallest of the four, it is also the brightest.]

What is impressive, reading these notes, is the amount of *unknowns* that resided inside those spots on the sky discovered by Stephan, as often happened in the history of science. One should remember that, at that time, even the bare existence of external galaxies was just a conjecture. In fact, although Immanuel Kant already proposed in the 18th century that nebulae were *Island Universes*, it was only in 1923 that Hubble proved the extragalactic nature of the “nebulae” by measuring the distance to the Andromeda galaxy from the period of the Cepheid stars in that galaxy. Furthermore Stephan probably couldn't even imagine the spectacular phenomena happening in the system named after him: extreme interactions between galaxies, morphological changes, stripping of gas outside galaxies, energetic phenomena such as the Active Galactic Nuclei (AGN) present in one of the group galaxies and an intergalactic collision producing a large scale shock front extending for several tens

of kiloparsec.

Because of the multiple interaction phenomena occurring in this group, Stephan's Quintet (SQ) has been observed in almost all accessible wavelength bands and it shows peculiar emission features in all of them.

A new part of the electromagnetic spectrum recently accessible with sufficiently high resolution to distinguish discrete sources in SQ is the mid-/far-infrared wavelength regime in the range $3 - 160\mu\text{m}$, dominated by emission from dust/PAH particles. This thesis will focus on the emission in that spectral regime and presents an analysis of MIR and FIR maps of SQ taken with the Spitzer Space Telescope. Although Spitzer has provided FIR maps of SQ with resolutions far better than those previously obtained with the Infrared Space Observatory, presented by Xu et al. (1999) and Xu et al. (2003), FIR photometry of sources in SQ is still very challenging because of the confusion produced by the vicinity of sources in such a crowded field. The work presented in this thesis represents a first attempt to separate the different components of dust emission in SQ in order to quantify the fluxes associated with each source and investigate the related scientific implications. Understanding the nature of this emission is important because it is directly linked to the star formation events occurring in this group and, at the same time, it can be partially powered by collisions between dust and hot plasma particles, thus providing an additional cooling mechanism to the hot gas.

SQ has always been a prototype object for forerunner observations in new parts of the electromagnetic spectrum or with improved instrumentation. As well as many other previous observations in different wavelength bands, the Spitzer FIR maps show new surprising features, which can be partially explained in terms of scenarios previously proposed for this system, but also provide evidences for new phenomena, still to be fully investigated.

Chapter 1

Introduction

1.1 Groups and cluster of galaxies: formation and evolution

– Structure growth in Λ -CDM

During the last two decades the cosmological framework of the Λ -CDM¹ model, in which the energy content of the Universe is divided between baryonic matter (4%), cold dark matter (23%) and dark energy (73%), became the standard theoretical foundation for models of galaxy formation. In Λ CDM structures grew from weak density fluctuations present in the otherwise homogenous and rapidly expanding early Universe. These fluctuations, amplified by gravity, eventually turned into the rich variety of structures we observe today. The detailed evolution of these initial fluctuations, a highly non linear process, can be predicted only using huge numerical simulations as the Millenium Simulation (Springel et al. 2005,S05). These simulations show how the process of structure formation involves a hierarchical build up of bigger and bigger structures.

Modern cosmological simulations have reached impressively high resolutions. Fig. 1.1, taken from S05, shows the present day mass distribution in a Λ -CDM Universe on various scales, from 4Mpc to 1Gpc. The zoomed out panel at the

¹ Λ -CDM is the abbreviation for Λ -Cold Dark Matter where Λ stands for the cosmological constant which is associated with dark energy.

bottom reveals a tight network of cold dark matter clusters and filaments of characteristic size $\sim 100h^{-1}\text{Mpc}$. At these large scales the mass distribution can be considered with good approximation to be homogeneous and isotropic. The subsequent images zoom in by factor of four onto the region surrounding one of the many rich clusters. The final image on the top reveals several hundred dark matter substructures, resolved as independent, gravitationally bound objects orbiting within the cluster halo. Therefore mutual gravitational attraction between dark matter particles has brought to the spontaneous formation of groups/clusters of dark matter halos (DMH) embedded in bigger dark matter structures.

– Gas accretion within dark matter halos

The distribution of matter in the Universe determines the gravity field that regulates the motion of baryons and, as most matter is dark in Λ -CDM, DMHs become the centres of attraction where baryonic matter tends to accumulate. The gas accretion on DMHs can occur in two different modalities, a hot and a cold mode. In the hot mode, during its falling into the potential well of a DMH, gas is shocked–heated to temperatures $\approx 10^6\text{K}$ (Dolag et al. 2006). This mode occurs when gas is accreted on DMH with mass $\gtrsim 10^{12}M_{\odot}$ (Dekel et al. 2006). For DMHs of lower mass, the accreting gas doesn't get shocked and it can fall into the dark matter potential being relatively cold. Since the process of star formation requires cold gas to occur, it follows that cold mode accretion is much more suitable to the purpose of feeding star formation in DMHs than hot mode accretion, where gas can take a very long time to cool. The accretion of cold gas in low mass DMHs led to the formation of the first stars and galaxies. According to recent works on gas accretion, filaments of cold gas, penetrating low mass DMHs, have been indeed the main way to induce star formation in the early Universe and also to maintain it afterwards, providing additional material to be converted into stars (Dekel et al. 2006, Kereš et al. 2009). Hot mode accretion has produced the formation of halos of hot gas filling the space between galaxies in groups and cluster of galaxies (the so-called intragroup/intracluster medium). The presence of these hot gas halos should inhibit cold accretion within group/clusters at redshifts $z < 2$, and this is one of the poten-

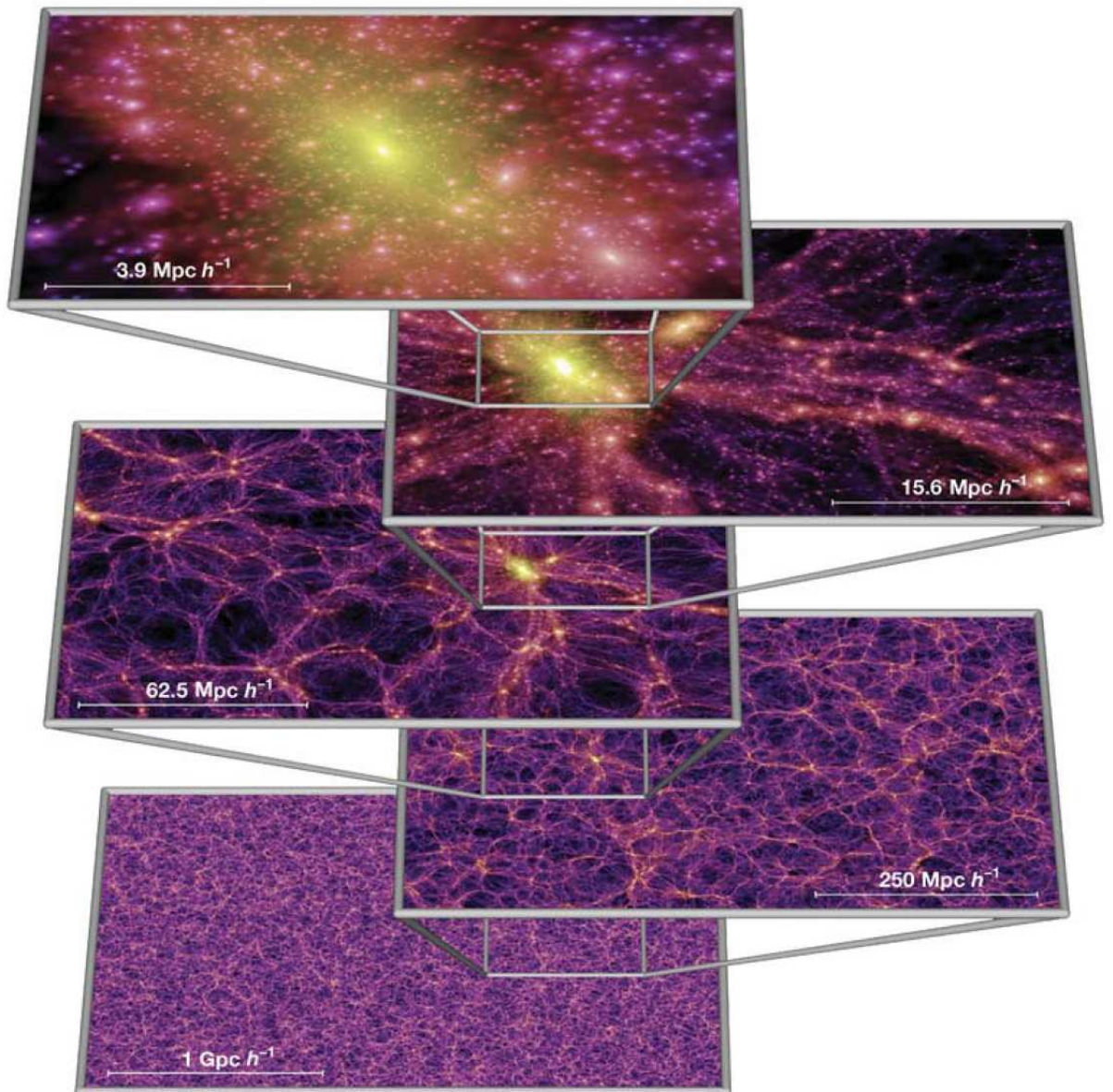


Figure 1.1: The dark matter density field on various scales presented by Springel et al. (2005). Each individual image shows the projected dark matter density field in a slab of thickness $15h^{-1}\text{Mpc}$ (sliced from the periodic simulation volume at an angle chosen to avoid replicating structures in the lower two images), colour-coded by density and local dark matter velocity dispersion. The zoom sequence displays consecutive enlargements by factors of four, centred on one of the many galaxy cluster halos present in the simulation.

tial reasons why the intensity of star formation events is observed to be reduced in these environments in the local Universe.

– **Galaxy interactions**

After the first episodes of galaxy formation in low mass DMHs, the subsequent clustering and merging of DMHs have had consequences also for the embedded galaxies that began interacting with each other and with the intergalactic medium (IGM) pervading clusters/groups. In fact galaxy–galaxy interactions and galaxy–IGM interaction/interplay are thought to play a key role in determining the evolution of galaxy properties in groups and clusters along cosmic time (see e.g. review by Van Gorkom et al. 2004).

Galaxy–galaxy interactions (see Struck 2006 for a recent review) can be of a different kind but they can be classified in two broad categories: low velocity ($\sim 10^2$ km/s) and high velocity ($\sim 10^3$ km/s) encounters. Low velocity galaxy–galaxy encounters can result in a merger, an interaction that leads to the formation of a single galaxy out of the stars and the interstellar medium of the colliding galaxies. When this kind of collision happens between galaxies of similar size (major mergers), star orbits become randomized and the final object assumes the shape of an elliptical galaxy. These events are believed to transform galaxies from spiral disk type into spheroidal type. Mergers between galaxies of significantly different size (minor mergers) result in an increase of the total mass associated with the bigger galaxy without modifying its basic disk large scale morphology. High velocity galaxy–galaxy collisions are instead more effective in displacing interstellar gas and producing tidal distortions. Both these kinds of encounters can induce either gas inflows towards the galaxy centers, triggering central starburst and/or AGN activity, or removal of gas outside the galaxies. In the latter case, the chemically enriched gas extracted from the galaxies can disperse into the intergalactic medium, fall back into the galaxy mainbodies or simply collapse and give rise to intergalactic star formation regions. In this context of particular interest are the so-called Tidal Dwarf Galaxies, found on tidal tails or debris, which are the only galaxies forming in the present Universe (Braine et al. 2001). Tidal interactions can also induce the

formation of a bar component in perturbed galaxy disks. Bars favour gas motion towards galaxy central regions, since they transfer angular momentum outward in the disk, and drive spiral density waves. Therefore the presence of this feature can trigger central star formation/AGN activity in disk galaxies.

As we described before, galaxies and IGM are deeply interconnected since galaxies acquire from the surrounding IGM the fuel for on-going star formation. However galaxies are not just passive objects but they can also inject energy and chemically enriched material into the IGM through feedback processes due to massive supernovae explosions and AGN jets. The actual effect of galaxy feedback on the IGM is not clear. In fact the chemical enrichment of IGM due to feedback processes favour the cooling of the intergalactic gas, because of the higher metal content but, on the other hand, the large amounts of energy transferred to the IGM can prevent its further cooling on the galaxies themselves. Galaxy–IGM collisions are also important in modifying the internal gas distribution in galaxies, affecting the location and the efficiency of star formation within galaxy mainbodies. Galaxies falling into clusters experience ram pressure stripping due to the presence of the intracluster medium. This phenomena gradually removes the gas from the infalling galaxy disk or from the surrounding galactic halo (in the last case it is usually referred to as “galaxy strangulation”). In both cases star formation in the galaxy results inhibited because of the direct removal of the gas already forming stars in the galaxy disk or of the gas reservoir around the galaxy itself.

To summarize one might say that the growth and evolution of galaxies (i.e. large kpc scale agglomerates of stars and gas) is affected by four external factors: 1) the evolution of the pervading dark matter structure; 2) the gas cooling processes occurring in the intergalactic medium (where most of the baryons still reside at the present day); 3) galaxy–galaxy interactions; 4) the complex interplay between galaxies and intergalactic medium. All the processes we discussed before can have diverse consequences on the evolution of galaxies: they can enhance star formation, shut it down or simply displace star formation sites; at the same time galaxy morphologies can be dramatically modified.

– Galaxy bimodality

Although galaxy formation and evolution is evidently an extremely complex process, involving a large number of phenomena whose underlying physics is still not fully understood, what seems to be relatively simple it is the final result of 15 Billion years of galaxy evolution, evident from observations: galaxies can be roughly distinguished in two categories, “blue” and “red”, an empirical distinction termed as “galaxy bimodality” (see e.g. Kauffmann et al. 2003). Red galaxies are more massive (with stellar masses typically higher than $3 \times 10^{10} M_{\odot}$), they show low amounts of on-going star formation, they are red because they are dominated by old stellar populations and they present spheroidal morphologies. Blue galaxies dominate the low mass galaxy population in the present Universe, they host substantial on-going star formation, young star population giving them the blue color, and they are predominantly spirals or gas-rich dwarfs. In a sense, the famous Hubble classification of galaxies, separating spiral and elliptical galaxies, has been found much more informative than previously thought.

The basic goal of galaxy formation and evolution studies is reproducing the huge number of observations that are being available through extended deep galaxy surveys (e.g. COSMOS, Ilbert et al. 2010; COMBO-17, Bell et al. 2004). As we saw, this requires a detailed knowledge of an incredible amount of barionic physics related phenomena: gas accretion, star formation, galaxy interactions, star formation/AGN feedback, etc. To this purpose it is important to study in detail nearby objects where these phenomena, some of them happening much more frequently in the early Universe, can be better analyzed and understood in their consequences. In this regard the Stephan’s Quintet compact group of galaxies (SQ) present an exceptionally large set of physical processes whose understanding is fundamental to correctly model galaxy evolution. The observational evidences of the diverse episodes of galaxy interactions happened in the past or on-going in Stephan’s Quintet are summarized in the next section.

1.2 The Stephan’s Quintet compact group of galaxies

– Compact groups of galaxies

Compact groups of galaxies are aggregates of four or more galaxies showing projected separations on the order of $\sim 30 - 40$ kpc (Sulentic et al. 2001). Such a small separation between the group galaxies implies densities similar to the cores of rich clusters. However to be classified as “compact”, a galaxy group has also to be fairly distant from the galaxies belonging to the large scale structure around it and, therefore, these objects are typically located in not particularly dense environments (see the review by Hickson et al. 1997 for a description of the observational selection criteria.). The importance of compact groups is twofold: 1) they are ideal laboratories for studying the effects of extreme galaxy interactions, and 2) they are low-redshift analogous of those interaction processes that, as we summarized in the previous section, are believed to determine the evolution of galaxies during cosmic time.

– The galaxies in Stephan’s Quintet

The Stephan’s Quintet (SQ) compact group was originally defined as the group formed by the five galaxies in Fig. 1.2, showing a recently released high resolution color map of SQ taken by the Hubble Space Telescope (HST): the spiral galaxy NGC7320 (Sd), the irregular spirals NGC7319 (Sbc pec), classified as Seyfert 2 AGN galaxy, and NGC7318b (Sbc pec), the two ellipticals NGC7317 (E4) and NGC7318a (E2 pec). When precise redshifts measurements became available, it was found that NGC7320 has a recession velocity of ~ 800 km/s, much smaller than the recession velocities associated with the remaining four galaxies, which are in the range $5700 - 6700$ km/s as shown in Table 1.1. Converting redshifts into distances using the Hubble law $v_r = Hd$ (where v_r is the recession velocity, d the distance and H the Hubble constant), these measurements revealed that NGC7320 is a foreground galaxy, located at ≈ 10 Mpc, while the remaining galaxies are at ≈ 94 Mpc

(assuming a Hubble constant equal to 70km/s/Mpc)². It has also been found that NGC7320c (SAB), a spiral galaxy at about 2 arcmin west of NGC7319, presents a recession velocity equal to 6600km/s (Sulentic et al. 2001), consistent with those of the four more closely physically associated galaxies. The relative positions of all these galaxies can be seen in Fig. 1.3, showing an R-band map of SQ. Since, including NGC7320c, there are exactly five galaxies at the same distance, the group is still a “quintet” even if the original membership definition has changed. From Table 1.1 one can also notice that the recession velocity of NGC7318b, 5774km/s , differs by about 1000km/s from the velocities of the other four galaxies of the group. Since the velocity dispersion among the other four galaxies of the group is an order of magnitude smaller ($\sigma \sim 100\text{km/s}$), this suggests that NGC7318b is not in virial equilibrium with the rest of the group but is entering it at high velocity. As we will see later, the signature of the intrusion of NGC7318b into the group of the bounded galaxies is well in evidence in the observational data.

– Stellar and gas distribution in SQ

Looking at the optical SQ maps in Figs.1.2 and 1.3, one can immediately notice several signs of galaxy interactions: a tidal tail extending from NGC7319; a second tidal tail, fainter than the first one and just visible on the R-band map, apparently originating from NGC7320 but in reality passing behind it; the particularly distorted morphology of NGC7318b, presenting two tidal features that extend towards the north and apparently intersect each other in one point; a diffuse optical emission produced by a stellar halo. The galaxy optical morphologies appear indeed very peculiar but, to fully appreciate how fundamentally different SQ galaxies are,

²The presence of an HII region belonging to the high redshift group and seen towards the disk of the low redshift galaxy, together with an interaction feature apparently associated with NGC7320 (the old tail, see Fig. 1.3), led some authors to believe that all the five galaxies are physically at the same distance (e.g. Arp 1973). As it will be seen later, the detection of two distinct HI gas components associated respectively with the optical tail and NGC7320 disprove this hypothesis. Discordant redshift galaxies are found rather frequently in compact groups and their nature has been for many years a matter of debate (see review by Hickson et al. 1997). Nowadays it is generally accepted that their presence doesn't require a change in our interpretation of galaxy redshift.

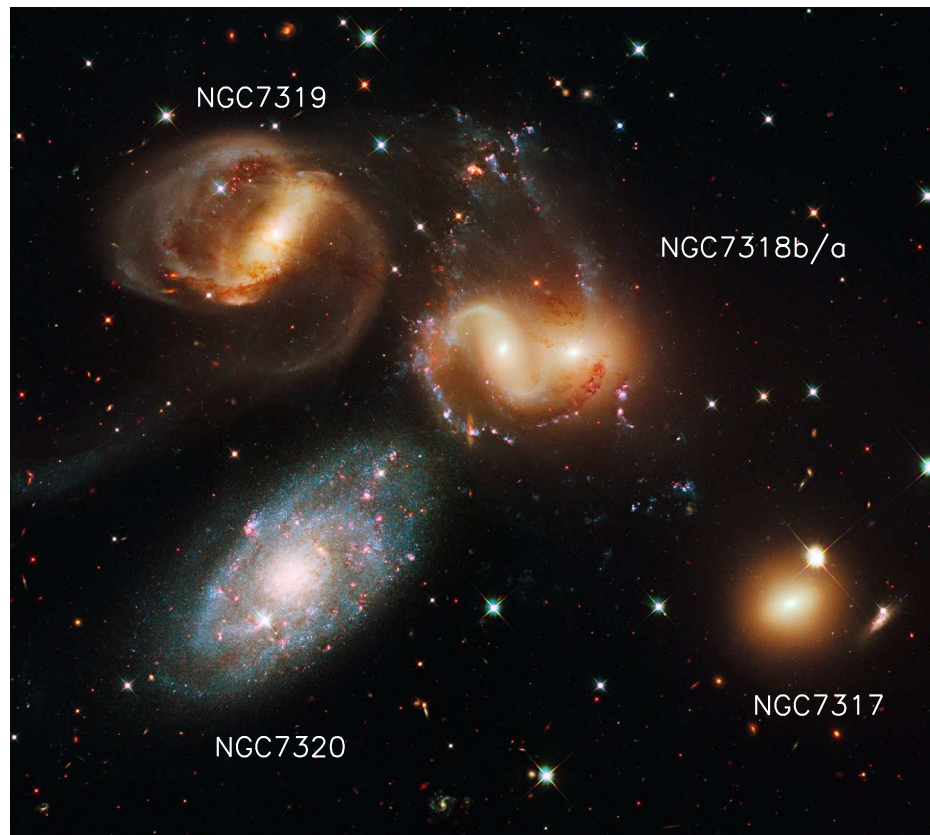


Figure 1.2: High resolution HST color image of Stephan's Quintet (Credit: NASA, ESA, and the Hubble SM4 ERO Team)

Galaxy	v_r (km/s)	z
NGC7317	6599 ± 26	0.022012 ± 0.000087
NGC7318a	6630 ± 23	0.022115 ± 0.000077
NGC7318b	5774 ± 24	0.019260 ± 0.000080
NGC7319	6747 ± 4	0.022507 ± 0.000012
NGC7320	786 ± 20	0.002622 ± 0.000067
NGC7320c	6583 ± 20	0.021958 ± 0.000067

Table 1.1: Recession velocities (v_r) and redshifts (z) of the main galaxies seen in the Stephan’s Quintet field of view. The values are taken by the Nasa Extragalactic Database with the exception of NGC7320c where we used the value quoted by Sulentic et al. (2001).

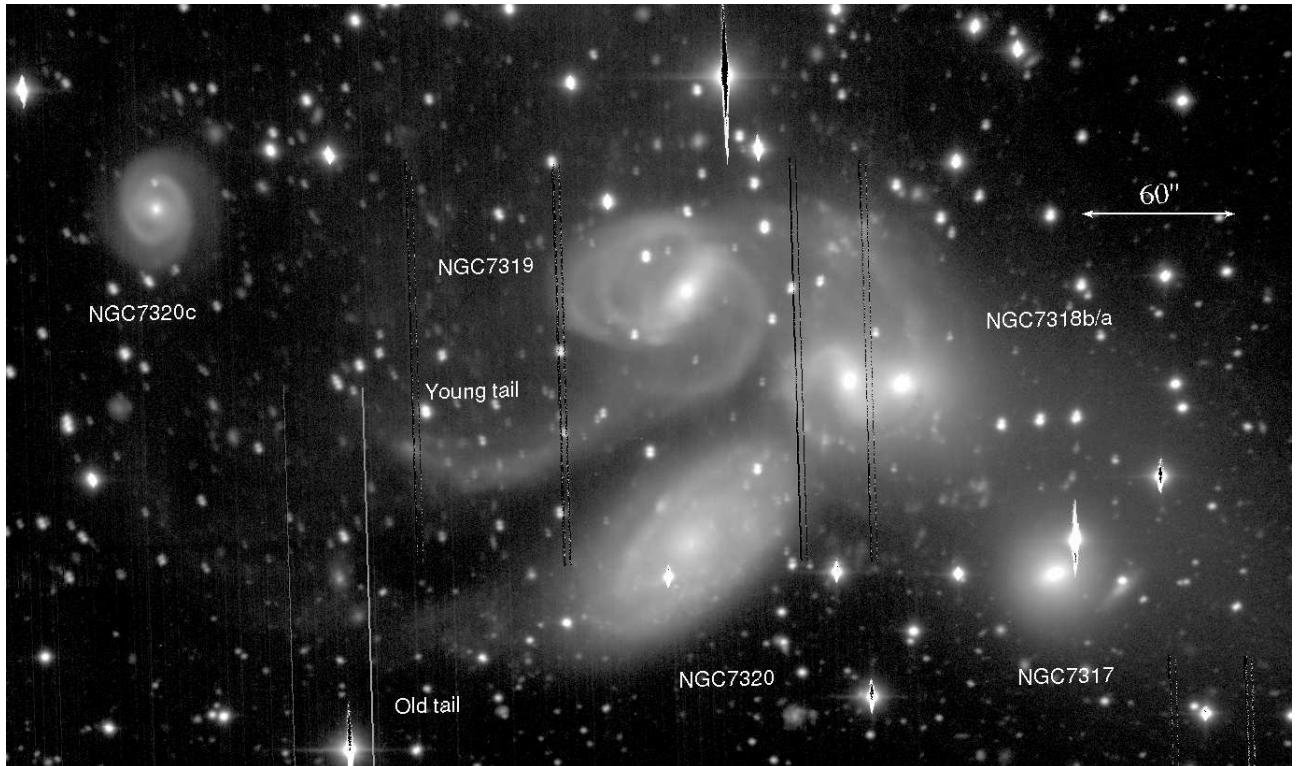


Figure 1.3: Large R-band map of Stephan’s Quintet taken by the Palomar 200-inch telescope.

compared to normal field galaxies, one needs to look at the gas distribution throughout the group in relation to the stellar distribution. Fig. 1.4 shows the contours of the neutral atomic hydrogen (HI) distribution overlaid on a R-band map of SQ. The image is taken by Williams et al. (2002) and the contours corresponds to the integrated emission in the entire SQ recession velocity range $5700 - 6700\text{km/s}$ (the data cube can be found in that paper). Several HI structures are visible and none of them follows the galaxy optical morphologies, in contrast with normal field galaxies that present regular HI distributions. Furthermore most of the HI in SQ is actually intergalactic. NGC7319 is basically devoid of neutral atomic gas while some HI is detected at the radial velocities corresponding to NGC7318b (see also HI contours in Fig. 1.8) but the gas is either found towards the north or towards the south of this galaxy, without any significant HI mass towards the central regions of the galaxy. A large intergalactic gas arc structure is observed extending from the south to the north-east of the group. The southern part of it follows the stellar old tidal tail³.

An even more surprising morphology is shown by hot gas emission as seen at X-ray wavelengths. In Fig. 1.6 we show the maps at three X-ray energy ranges taken by the XMM-Newton observatory and published by Trinchieri et al. (2005). The soft X-ray regime $0.3 - 1.5\text{keV}$ shows a north-south feature that is largely overlapping with the western of the two tidal features associated with NGC7318b. The center of NGC7319 is a particularly bright X-ray source at all energies. An extended diffuse emission is also detected at soft-middle X-ray wavelengths. Trinchieri et al. (2005) identified two components contributing to diffuse X-ray (see Fig. 1.7): the halo, covering the central parts of the group, and the tail, roughly coincident with the old optical tail. The north-south feature has a radio-continuum counterpart as shown in Fig. 1.5 taken by Williams et al. (2002). Notably the central regions of NGC7319 and NGC7318a are also particularly bright at radio wavelengths.

³As one can see from Fig. 1.4, the HI arc is a continuous structure extending from the area of the sky covered by the foreground galaxy NGC7320 towards the north-east of SQ. In the direction of NGC7320 a regular HI disk distribution has been detected by Williams et al. (2002) (see Fig. 2 of that paper) at recession velocities corresponding to that galaxy. This conclusively demonstrates that the tidal stellar/gaseous feature is not connected with NGC7320 but passes behind it.

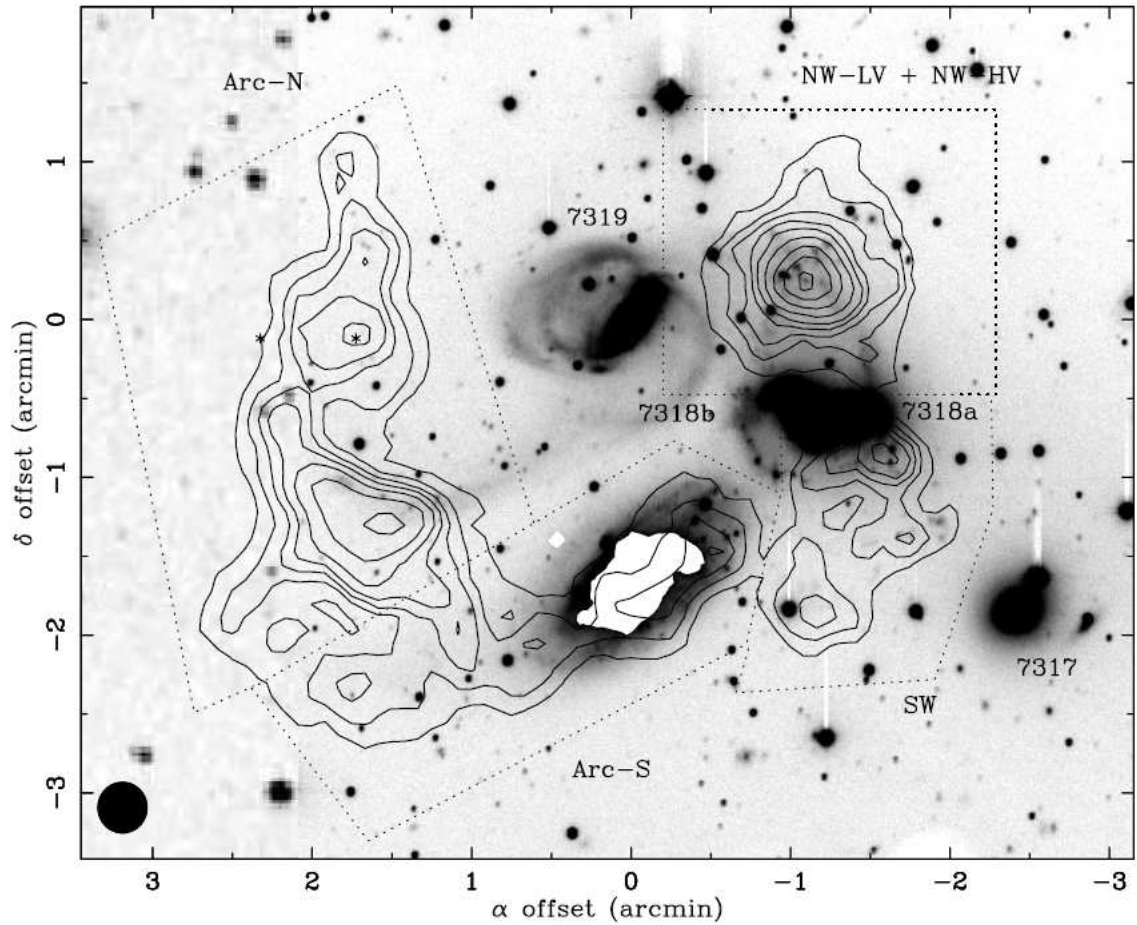


Figure 1.4: Contours of the HI gas distribution in SQ overlaid on an R-band image (from Williams et al. 2002). The integration velocity range is $5597 - 6918 \text{ km/s}$ and the contours are $5.8, 15, 23, 32, 44, 61, 87, 120, 180 \times 10^{19} \text{ cm}^{-2}$. The synthesized beam is $19''.4 \times 18''.6$.

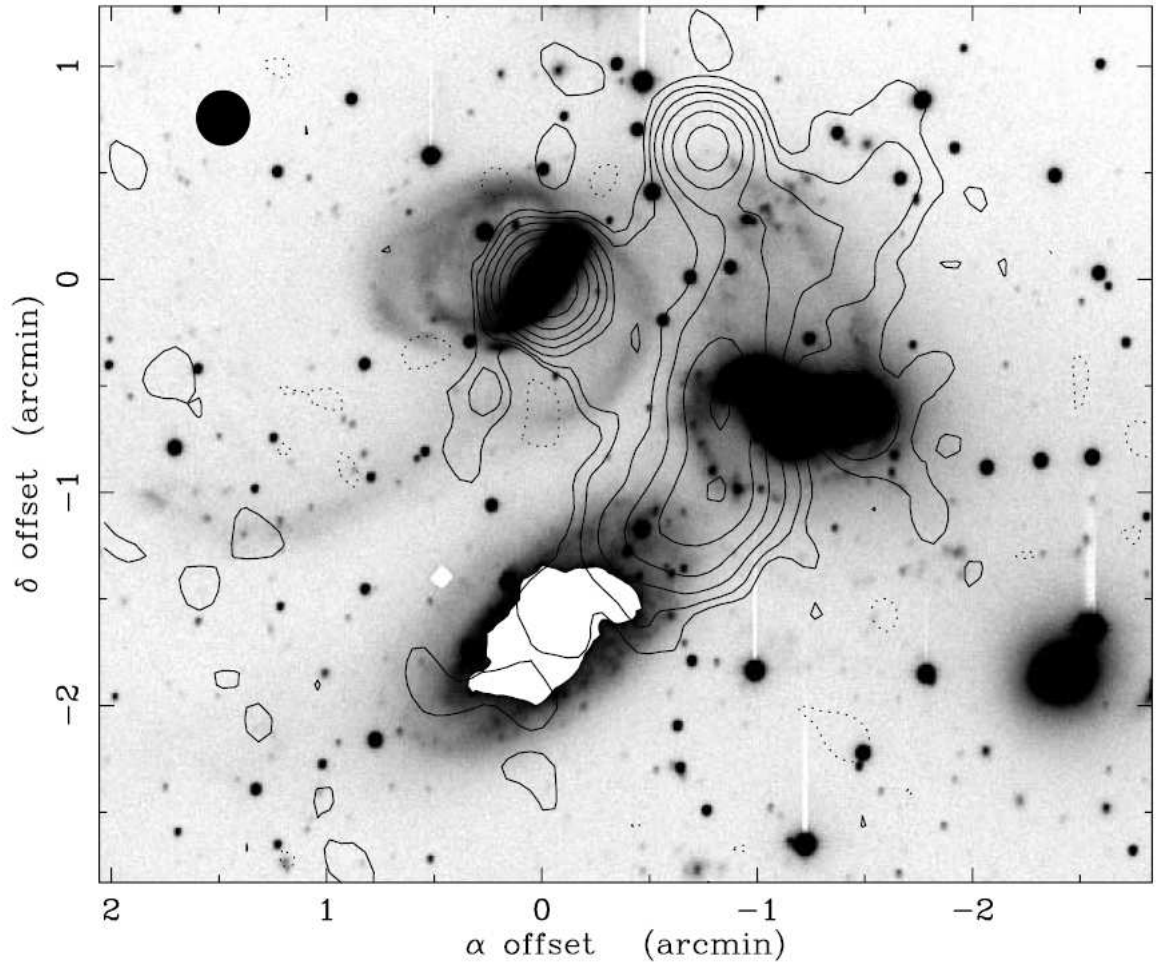


Figure 1.5: Contours of the 21cm continuum emission in SQ overlaid on an R-band image (from Williams et al. 2002). The contours are $-0.2, 0.2, 0.4, 0.8, 1.6, 3.2, 6.4, 13, 26 \text{ mJy beam}^{-1}$. The synthesized beam, $15''.4 \times 14''.8$, is shown on the upper left corner.

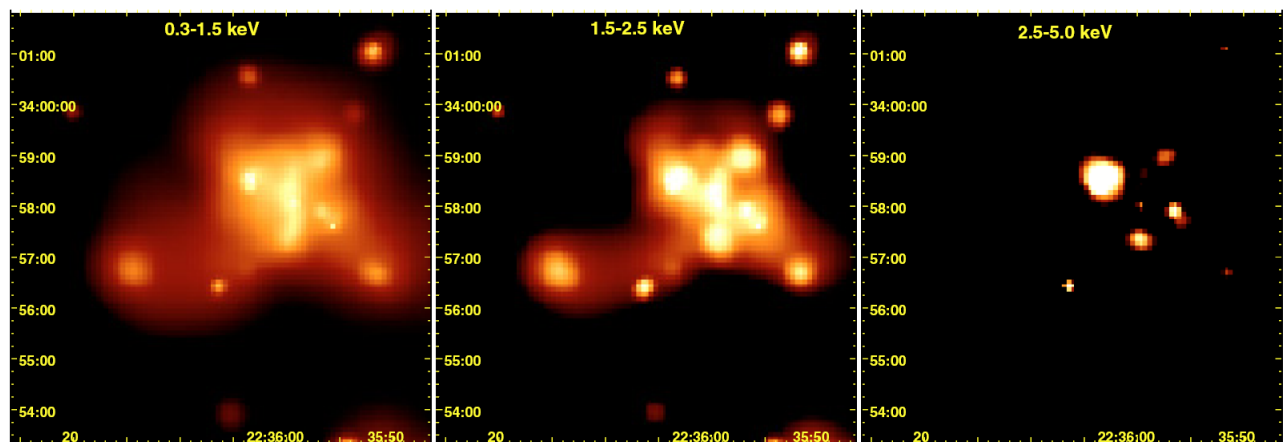


Figure 1.6: X-ray maps of SQ at several energy ranges obtained with the XMM-NEWTON observatory (from Trinchieri et al. 2005).

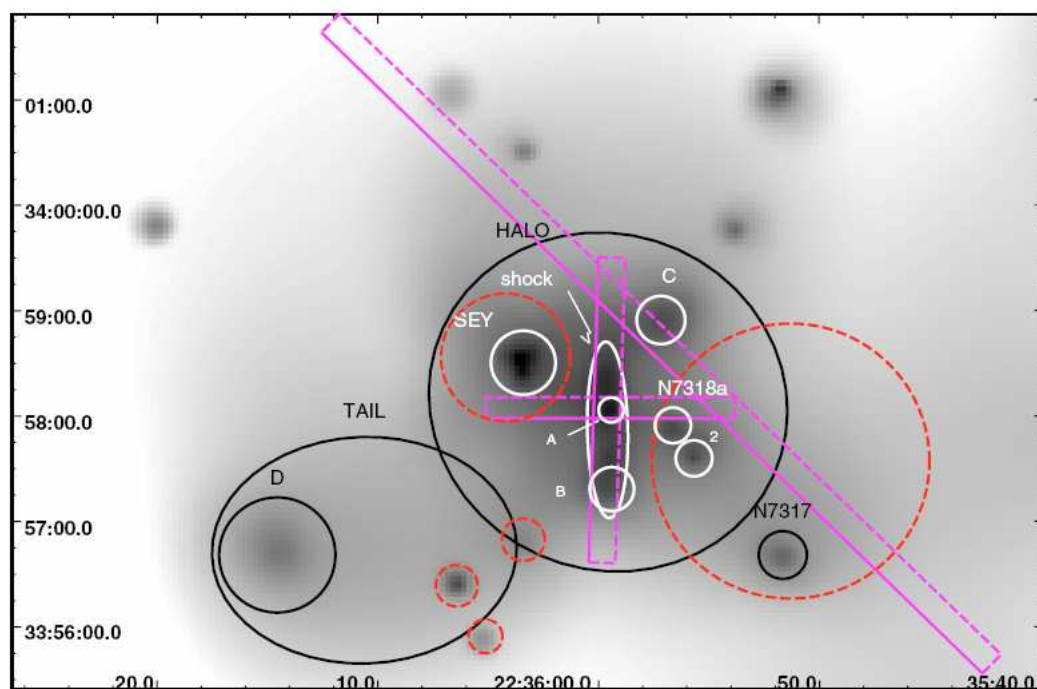


Figure 1.7: SQ X-ray emission regions identified by Trinchieri et al. (2005)

The north–south feature seen at X-ray and radio continuum appears also as H_α and warm molecular hydrogen line emission. Fig. 1.8 shows H_α interference filter maps of the group in two panels: the upper panel shows the emission in the velocity range 6300 – 7000km/s, associated with the bounded part of the group; the lower one shows the emission in the velocity range 5600 – 6000km/s, associated with the intruder galaxy NGC7318b. On the same panels the HI contours, corresponding to similar ranges of radial velocities, are overlaid. From the H_α maps we realize that: 1) the north–south feature is from gas associated with the bounded group; 2) the central regions of NGC7319 are particularly bright; 3) there are numerous clumps of emission, most probably produced by HII regions, associated with both the bounded group and NGC7318b. The most luminous of these sources is at the northern tip of the ridge feature, a source named SQ A by Xu et al. (1999). A second source particularly distant from galaxy centers, SQ B, is located towards the east of the group, precisely on the tidal tail originating from NGC7319; 4) there is a bridge of emission connecting the north–south feature with NGC7319.

Fig. 1.9 is taken by Cluver et al. (2010) and shows the contours of molecular hydrogen infrared rotational line emission overlaid on a R-band image of SQ. The lower molecular transitions (upper panels) show, apart from emission coincident with the central regions of NGC7319 and the HI blob located towards the north of NGC7318b, the same north–south linear feature seen already at other wavelengths. In the same region of this feature, the morphology of the higher transitions (lower panels) is more clumpy but still resembles a linear vertical structure.

– Interpretation of SQ multiwavelength observations

We have seen that SQ presents a complex emission morphology showing diverse features when observed at different wavelengths. However the multiwavelength observations can be interpreted in terms of a past series of interactions between the galaxies of the group, which happened in the last Gyr, plus an on-going collision with a characteristic time scale of 10^7 yr (Moles et al. 1998, Sulentic et al. 2001). The tidal tails observed on the optical maps were most probably produced by two successive passages of NGC7320c. The evidence for this interpretation is that the

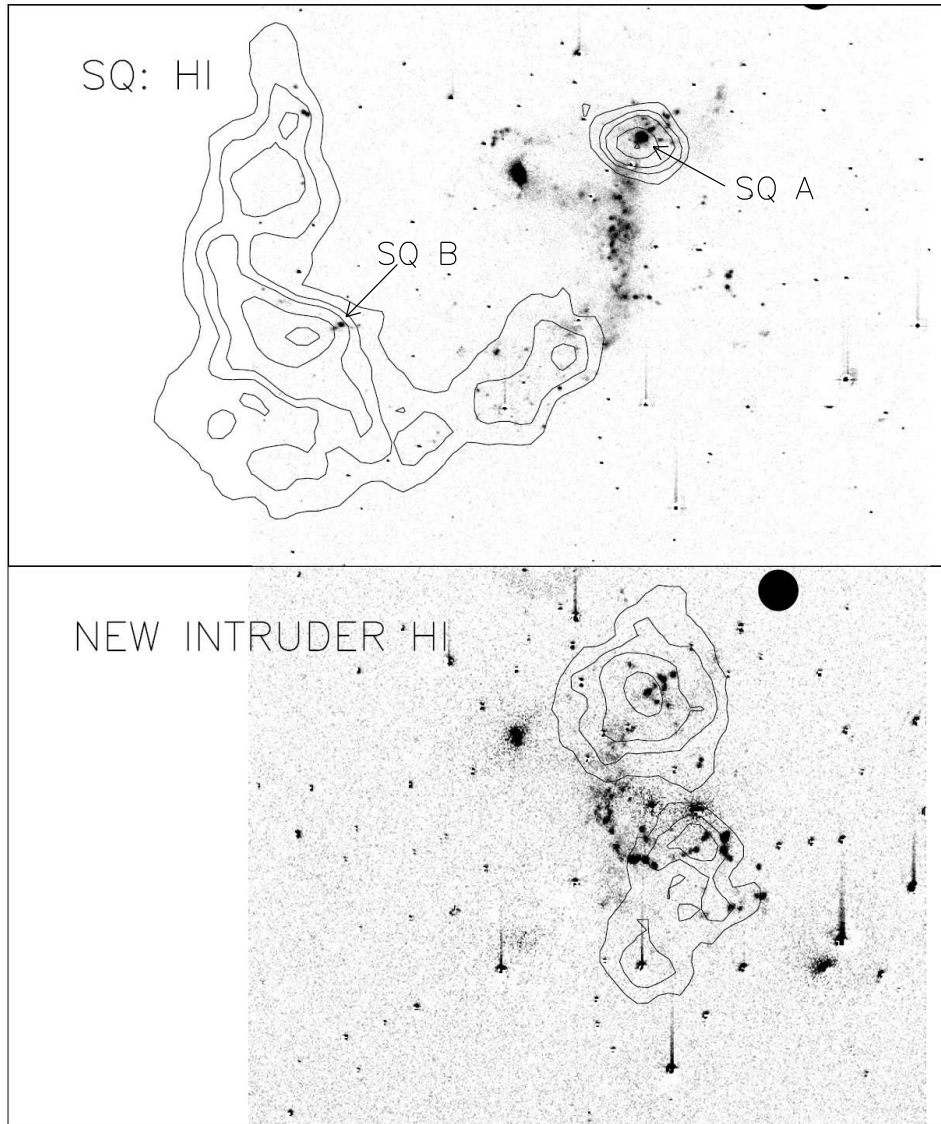


Figure 1.8: H_α interference filter maps presented by Sulentic et al. (2001). In the upper panel the H_α emission in the velocity range 6300 – 7000km/s, corresponding to the SQ group, is shown. In the lower panel the velocity range is 5600 – 6000km/s, corresponding to the intruder galaxy NGC7318b. HI contours for velocities in the SQ range (6475 – 6755km/s) and in the NGC7318b range (5597 – 6068km/s) are overlaid on the two images.

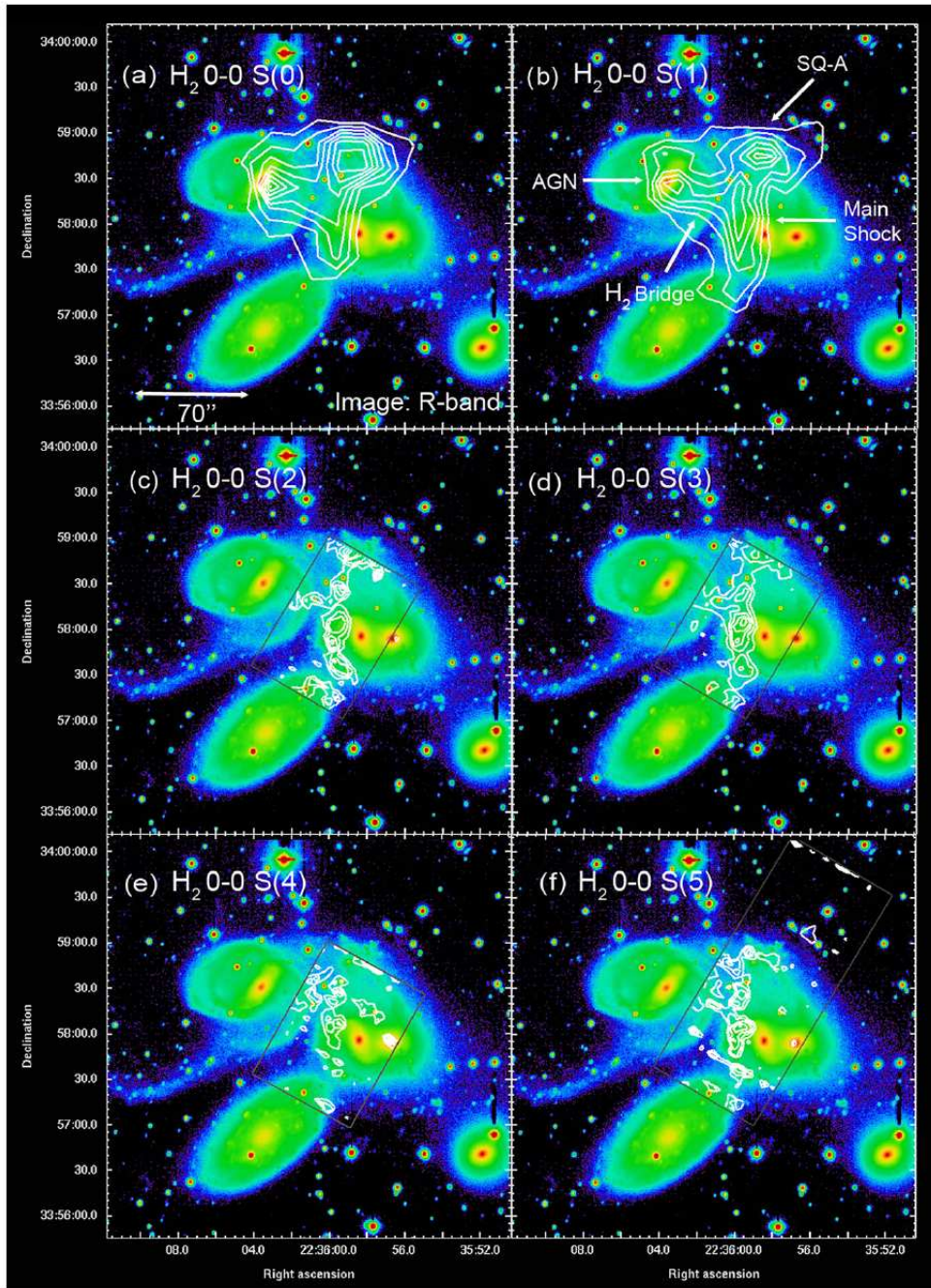


Figure 1.9: SQ warm H_2 line emission contours overlaid on an R-band image (from Cluver et al. 2010). Contour levels are as follows (all in units of MJy/sr): (a) 0.1, 0.14, 0.19, 0.28, 0.32, 0.37, 0.41, 0.46, 0.5, (b) 0.3, 0.53, 0.75, 0.98, 1.2, 1.43, 1.65, 1.88, 2.1, (c) 0.3, 0.4, 0.5, 0.6, 0.7, (d) 0.25, 0.42, 0.58, 0.75, 0.92, 1.08, 1.25, (e) 0.11, 0.19, 0.27, 0.36, 0.44, 0.52, 0.6, and (f) 0.3, 0.46, 0.61, 0.77, 0.93, 1.09, 1.24, 1.4..

tidal tails point roughly towards NGC7320c. The tail originating from NGC7319 is considered the youngest one since its bluer color and narrower width suggest that it has been produced more recently than the redder and broader tail seen to the south. From kinematic arguments and from considerations on the colors of the stellar populations forming the tails, Sulentic et al. (2001) estimated an age of $2 - 4 \times 10^8$ yr for the young tail and $6 - 12 \times 10^8$ yr for the old one. Similarly the large decoupling between HI gas and galaxies in SQ can also be explained in terms of tidal removal of gas during galaxy close passages. The southern part of the arc HI feature is overlapping with the old tail, strongly suggesting that the formation of the stellar and the gaseous features arose from the same tidal interaction. We have seen that there is no HI in the NGC7319 galaxy disk. However at the same time this galaxy hosts an AGN, whose emission is visible at all the wavelengths from radio to X-ray. The triggering of the AGN activity has also been plausibly induced by tidal interactions, perhaps through the formation of the bar observed in that galaxy. In fact, as we mentioned in Sect. 1.1, this feature can be created by tidal forces and it favours inflows of gas towards galaxy centers. Therefore it might be that the bar has been formed during the interaction with NGC7320c and the successive inflowing of gas has triggered the AGN we observe in that galaxy.

– The shock region

Perhaps the most intriguing characteristic of SQ is the linear north–south feature observed at X-ray and Radio wavelengths as well as in H_α and infrared warm H_2 line emission. The emission in that region is the signature of a large scale shock produced by a high velocity collision between the intruder galaxy NGC7318b and the intergalactic medium of SQ. In fact, as we mentioned before, NGC7318b is entering the group at velocity ~ 1000 km/s relative to the average velocities of the bounded galaxies. Therefore, the emission seen in X-rays is consistent with this scenario because the post–shock gas temperature, in such a high velocity collision, is predicted to be of the order of millions of degrees, a temperature regime where the gas emits mainly at X-ray wavelengths. The corresponding radio continuum ridge can be explained in terms of synchrotron emission from relativistic particles accelerated at

the shock front. Finally optical spectral analysis by Xu et al. (2003) showed that the optical line emission in the shock region is dominated by shock excitation rather than by photons from star formation regions, providing a strong constraint on this interpretation. However, given the high velocity of the collision, an aspect that has been a matter of debate in the last years has been the presence of cold gas phases in this region as revealed by the H_α line, tracing ionized gas at temperatures $T \sim 10^4\text{K}$, and the warm H_2 line emission, tracing molecular gas at temperatures $T \sim 10^2\text{K}$. In fact, from the luminosity of the X-ray gas (see Sect.3.2.4) one can show that the hot gas cooling time scale is about 10^8yr , that is, rather longer than the dynamical time scale of the collision ($\sim 10^7\text{yr}$). Therefore, unless additional mechanisms are available for the cooling of the hot gas, the cold gas observed in the shock region cannot be explained in terms of cooled hot gas downstream of the large scale shock front. Furthermore the high velocity dispersion associated with both ionized gas and molecular gas, $\sigma \sim 10^3\text{km/s}$ (see respectively Xu et al. 2003 and Appleton et al. 2006), suggests that the medium is highly turbulent and the hot and cold gas phases are mixed together. The fact that the shock ridge connects two HI clouds that are kinematically connected (see Fig. 1.8), presenting similar radial velocities, provides a key hint into the nature of the pre-shock gas and the formation of the observed multiphase medium. As described by Sulentic et al. (2001), if the north-south ridge is replaced with a strip of cold HI gas, one gets a plausible idea for the distribution of the cold gas before the collision. Since at the present time there is a gap between the north and the south HI clouds, coincident with the region covered by the shock ridge, it has been suggested that the collision happened between the interstellar medium of NGC7318b and a part of the intergalactic HI gas, stripped out from the galaxies in previous interaction events (Sulentic et al. 2001). Both the intruder ISM and the IGM HI were therefore cold and possibly clumpy before the collision, presenting a large range of gas densities. On the basis of these arguments, Guillard et al. (2009) proposed a scenario in which the observed molecular gas, detected from the infrared lines, is formed downstream of the shock front from pre-existing HI clouds. In their model they considered a large scale shock front propagating through the tenuous intercloud component of the gas, with densities $\lesssim 0.1\text{cm}^{-3}$. When the shock front

hits a denser HI cloud, a lower velocity shock propagates into it. Then, the evolution of the shocked cloud depends on several factors: the possible triggering of hydrodynamical instabilities, the cooling of the gas layers after being shocked, the dust destruction and the formation of molecular hydrogen. These authors argued that the cooling of denser clouds is sufficiently fast to inhibit the growth of hydrodynamical instabilities, thus preventing the dispersion of the cloud into the hot medium, and that molecular hydrogen is formed out of the shocked HI clouds at the end of their cooling path. In this context, the powerful warm molecular line emission radiated by gas clouds in the shock region, not associated with star formation, is of particular interest because it might be an additional channel to radiate energy from the system as argued in a recent series of papers by Appleton and collaborators (Appleton et al. 2006, Guillard et al. 2009, Cluver et al. 2010). Previously, Xu et al. (2003) proposed that dust emission, powered by collisions between dust and plasma particles, is the main coolant of the hot gas in the shock region, although these authors only considered an homogeneous medium. The possible role of dust in the gas cooling process is one of the main points addressed in this thesis (see Chap..5.1).

– Star formation in SQ

Given the unusual gas distribution in the group, it is expected that the location of star formation sites is different from that seen in normal field galaxies. In fact from H_α (Fig. 1.8), UV and MIR observations (see Fig. 2.1 in the next chapter), one can see that star formation is not enhanced towards galaxy centers but is happening either in peripheral regions of the galaxies or into the intergalactic medium. Of particular interest are the star formation regions SQ A and SQ B. The SQ A starburst is originating from intergalactic gas as demonstrated by the velocity measurements from ionized gas spectral line emission (Xu et al. 1999) and CO detections (Gao et al. 2000, Lisenfeld et al. 2002). However, in the same area, localized star formation activity is also happening in the intruder galaxy elongated disk. These observational results, together with the simultaneous presence of the shock linear structure to the south of SQ A, suggest that the starburst has also been induced by the collision between NGC7318b and SQ IGM. Xu et al. (2003) argued

that the starburst has been triggered by shock compression of pre-existing molecular clouds entering an overpressurized region filled with hot gas produced, as in the case of the Guillard model, by a shock over-running a more tenuous gas component. This triggering mechanism is based on a theoretical work by Jog et al. (1992) and it is consistent with the fact that no starburst is detected at intermediate velocities between SQ and the intruder galaxy. In fact, in this model, star formation happens in the pre-existing molecular clouds that do not collide because of the small cross section and approximately conserve their momentum while entering the overpressurized region. However X-ray gas emission, expected from the tenuous component of gas heated by a high-velocity shock, is not particularly enhanced close to SQ A where most of the gas seems to be pretty cold. Also it has not been clarified yet why the HI distribution around SQ A has a round shape, suggesting the onset of a global collapse, while the shock region below is much hotter and turbulent. The other bright intergalactic star formation region, SQ B, is located on a tidal tail and, therefore, this source has been considered as a candidate site for the formation of tidal dwarf galaxies (Lisenfeld et al. 2002). This source is just to the west of an HI enhancement on the intergalactic HI arc structure (see Fig. 1.8) that does not show any particular star formation activity, even though it contains huge amount of cold atomic gas.

To conclude, a standard picture for the interaction history and the current interaction phenomena in SQ is now well established. However there are several processes that still have to be clarified, such as the cooling of the gas in the shock ridge and the modalities under which star formation is proceeding throughout the group. In this thesis we will make use of data in a range of wavelengths that has not been discussed yet, the mid- and far-infrared regime dominated by dust emission, to obtain some additional insights into the phenomena occurring in SQ and their implications for the evolution of galaxy groups and clusters.

1.3 What can we learn from studying the dust emission from SQ?

– Dust particles

In astrophysics the term “dust” is used to identify essentially two components of the interstellar medium: 1) solid particles with sizes of fractions of microns thought to be composed mainly of graphite, silicates and iron (even though different composition mix are consistent with observational constraints, see Zubko et al. 2004); 2) Polycyclic aromatic hydrocarbon molecules (PAH), that can be thought of as flat molecules of interconnected molecular units corresponding to the benzene molecule C_6H_6 . Dust particles emit radiation in the MIR–FIR and sub-mm ranges. This happens because the temperatures of dust particles, heated by radiation sources, are of order of $10 - 10^2$ K. Higher temperatures than $\sim 10^3$ K are not reachable because any form of dust is destroyed when heated to these levels. In the case of PAHs, radiative excitation induces fluorescent line emission visible in the MIR regime (see e.g. Leger & Puget (1984)).

Dust has been detected in very different environments: molecular clouds, diffuse interstellar medium, galaxy cirrus structures, AGN torus, circumstellar disks, planetary nebula, etc. Its importance is twofold: 1) dust plays an active role in determining the thermodynamical and chemical processes of the gas in which it is embedded, as for example injecting energetic photoelectrons into the ISM or catalyzing the formation of molecular hydrogen; 2) dust absorbs radiation in the optical/UV and it re-emits it in the infrared. Therefore, from studying the emission from dust grains one can infer the properties of the sources that power the emission itself. A typical example is the use of dust emission as a star formation rate indicator, since dust in the parent molecular clouds of newly formed stars absorbs a large fraction of the UV radiation from young stars and the luminosity of the dust infrared emission is then proportional to the rate at which stars are being formed.

An alternative way to heat dust, typically not considered in studies of dust emission on galactic scales, occurs when dust is embedded in hot plasma at temperatures $\sim 10^6$ K. In this hot environment dust grains are continuously hit by energetic par-

ticles that, in the process of penetrating the grain, release a fraction of their kinetic energy. This continuous transfer of energy from the plasma to the grains can be comparable to the transfer of energy from photons of the interstellar radiation field. Therefore, even though the heating mechanism is different, collisional heated dust emission appears at infrared wavelengths as well. Apart from heating dust, this process acts as a very efficient way to cool the hot gas in a temperature regime where gas radiative process are rather inefficient. However one should also notice that dust in hot plasma is quickly destroyed because of dust sputtering, the gradual removal of atoms from grains due to the collisions between grains and energetic ions. Therefore the efficiency of dust as coolant of the hot gas depends strictly on the dust abundance which is expected to be very low. Collisional heating of dust has been used to model dust emission from supernovae remnants by Dwek et al. (1981), among others. Details about the dust collisional heating process can be found in that paper.

– Dust emission in SQ

Previous studies of the dust emission in SQ were presented by Xu et al. (1999) and Xu et al. (2003), using data from the Infrared Space Observatory in the $6 - 100\mu\text{m}$ range. These data led to the discovery of the source SQ A as the first example of an intergalactic starburst triggered by a direct galaxy-IGM high-velocity collision. At the same time, dust emission from the shock region was detected. This opened the possibility that the emission in this region is indeed produced by dust collisional heating. Unfortunately the low resolution of the ISO data didn't allow a precise photometry of the emission and an accurate morphological comparison with multiwavelength data. In this thesis we will make use of deep imaging of the FIR emission from SQ taken with the Spitzer Space Telescope. These data have superior angular resolution and sensitivity compared to the previous ISO data and extend the wavelength coverage to longer wavelengths (to $160\mu\text{m}$). Combining the FIR data with Spitzer MIR maps and multiwavelength observations, we will investigate several issues that can be summarized in four main categories:

1) Star formation: We will use dust emission to identify the location of the

obscured part of star formation in the SQ group and to quantify the overall intensity of the star formation events. SQ presents a large decoupling of gas and galaxies and, as we saw before, this implied a displacement of the star formation regions compared to the case of normal field galaxies, at least in terms of the unobscured star formation tracers. Interesting points that will be stressed are the total star formation rate in this group compared to the case of isolated galaxies and the star formation efficiency in extragalactic star formation regions.

2) Gas cooling in the shock region: If a sufficiently high quantity of dust is present in the hot plasma in the shock region of SQ, dust–plasma particles collisions may provide the dominant cooling mechanism for the hot gas and, therefore, determine the thermodynamical evolution of the gas in this region. In particular the cooling time may be significantly reduced with important consequences for future star formation episodes out of the shocked gas.

3) Hot group halo gas cooling: In the context of IGM gas fueling of star formation in galaxies and galaxy groups, it is very important to determine all the possible ways group halo gas can cool. A new mechanism recently under investigation (see Montier et al. 2004, Popescu et al. 2000) is, as in the case of the shock region, the cooling through dust–plasma particle collisions. In fact through several processes, such as the mixing of galaxian material within the X-ray halo or the injection of grains into the IGM from halo stars, it is possible to pollute the hot IGM with dust and enhance its cooling. In this work we will use observational and theoretical constraints to quantify the amount of dust emission from the halo which can be due to this mechanism.

4) Nature of dust emission in the Seyfert 2 galaxy NGC7319: NGC7319 is a very bright MIR and FIR source. Since this galaxy is classified as Seyfert 2 (i.e. it hosts an obscured AGN) the bright MIR emission might potentially be explained in terms of AGN torus warm dust emission. However, as it will be seen later in Chaps. 2 and 3, this galaxy shows also a FIR emission of similar intensity compared

to the MIR flux and the peak of the FIR emission is located at the center of this galaxy. An obvious question we will address in this thesis is therefore whether the FIR emission we observe from this galaxy is powered by a central starburst or it is somehow powered by the central AGN.

– **Thesis outline**

The thesis outline is the following. In the second chapter we present the Spitzer data, we compare the dust emission with multiwavelength observations and we perform the photometry of all the detected sources. In chapter three we show the infrared spectral energy distributions (SED) for each source in SQ and we model them with template SEDs in order to infer useful physical parameters. In chapter four we derive star formation rates and we discuss the results we have obtained from source photometry and SED fitting and their consequences for star formation and AGN dust emission. In chapter five we discuss to which extent dust can contribute to the cooling of hot X-ray emitting gas. In chapter six we present a theoretical model of a steady-state shock, including dust collisional heating and dust destruction. A summary and conclusions close the thesis.

Chapter 2

SQ Dust Emission: Morphology and Source Photometry

2.1 Morphology of dust emission in SQ

In this section we describe the morphology of the dust emission in SQ, as seen on the Spitzer maps, in relation to the star and gas distribution in the group. In Fig. 2.1 (lower panel) we show all the Spitzer broad band maps (from IRAC and MIPS) where the signal is dominated by dust emission¹: $8\mu\text{m}$, $24\mu\text{m}$, $70\mu\text{m}$ and $160\mu\text{m}$ (details about Spitzer data reduction can be found in Appendix 2.A at the end of this chapter). These can be compared with the upper panel showing the SDSS r-band map, the GALEX FUV map, the VLA radio 21 cm line map and the XMM NEWTON soft X-ray map. On each map, crosses identify the galaxy centres.

The IR morphology of the galaxies seen in the IR maps is markedly different from the optical morphology. This is true not only for the early type galaxies but also for the late type galaxies which exhibit remarkable little infrared emission from the main bodies of the galaxies. The only exception is the emission from the foreground

¹Throughout this thesis all the $8\mu\text{m}$ images presented have had the stellar component of the emission subtracted using the relation $F_\nu(8\mu\text{m}, \text{dust}) = F_\nu(8\mu\text{m}) - 0.232F_\nu(3.6\mu\text{m})$ (Helou et al. 2004). The $8\mu\text{m}$ Spitzer band also contains emission from rotational hydrogen lines which however we estimate in Sect. 3.1.3 to be unimportant in relation to the PAH and dust continuum emission

galaxy NGC 7320 which is quite symmetrical in all the Spitzer bands, having a filled disk of emission commonly seen in local universe field galaxies, compatible with the optical/UV appearance not showing any sign of interactions (consistent with its not being a member of SQ).

The infrared emission from NGC7319 is dominated by an unresolved nuclear source, presumably from the Seyfert 2 AGN, that is particularly prominent at 24 and $70\mu\text{m}$. At $8\mu\text{m}$ one can also clearly see emission from the disk of the AGN host galaxy. As it can be seen from the MIR maps, dust emission from compact star formation regions are detected all over the group and especially on the elongated features of the intruder galaxy NGC 7318b which are most prominently delineated in the UV. Here the similarity is strongest between the UV and the $8\mu\text{m}$ band though the most prominent discrete sources are also clearly seen at 24 and $70\mu\text{m}$. The most prominent such MIR/FIR source is SQ A, the star formation region located to the north of NGC 7318b, already detected by ISO, which can also be seen at $160\mu\text{m}$. From optical spectra (Xu et al. 2003) and radio observations (Lisenfeld et al. 2002, Williams et al. 2002) it is known that star formation in this region is associated with gas at radial velocities corresponding to both the intruder galaxy and the IGM of the group. Several further compact star formation regions are located on the southern arms of NGC 7318b. The brighter sources, HII SE and HII SW, are also detected on the $70\mu\text{m}$ map but not clearly seen on the lower resolution $160\mu\text{m}$ map. Two other bright MIR/FIR emitting regions detected on the Spitzer maps are SQ B, a star formation region located on the optical “young ” tidal tail (see Sulentic et al. 2001), and a source, HII N, located about $40''$ towards the north of the AGN galaxy.

There is no clear morphological counterpart in the infrared to the shock region, defined here by the ridge of emission that can be seen on the X-ray map. Nevertheless the $70\mu\text{m}$ map and more particularly the $160\mu\text{m}$ map show enhanced emission towards the peak of the X-ray emission. The ratio of the MIR 8 and $24\mu\text{m}$ emission to the $160\mu\text{m}$ emission at the same position appears rather low compared to the discrete sources associated with star formation such as SQ A.

A previously undetected feature is an extended component of FIR emission, that

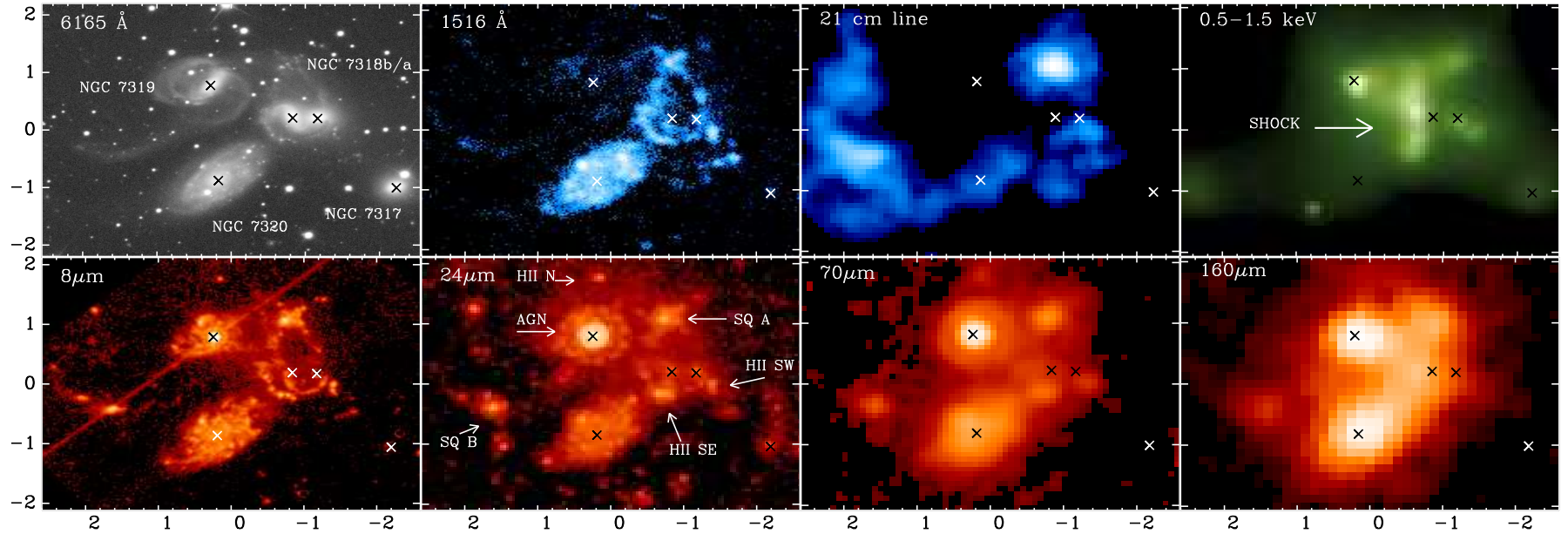


Figure 2.1: Stephan’s Quintet Multiwavelength Data. Upper row from left to right: SDDS r-band, GALEX FUV, VLA radio , XMM NEWTON soft X-ray. Lower row: SPITZER IRAC $8\mu\text{m}$ and MIPS 24, 70, $160\mu\text{m}$. Crosses on the maps identify the galaxy centers. The position (0,0) coincides with $RA = 22^h36'02.4'', Dec = +33^\circ57'46.0''$. The units on the axis are arcmin. At the distance of SQ (94 Mpc) every arcmin corresponds to 24kpc. Note that NGC 7320 is a foreground galaxy at the distance of 10 Mpc and its HI distribution, not shown in this figure, can be found in Williams et al. (2002).

we will refer to as “extended emission” in this thesis, spatially coincident with the main part of the group X-ray halo (as defined in Trinchieri et al. 2005, see Fig. 1.7). The appearance of the corresponding MIR emission on the higher resolution 8 and $24\mu\text{m}$ images suggests that the extended FIR emission may at least in part be clumpy rather than uniform, possibly indicating the presence of faint star formation regions far away from the centers of the galaxies.

In order to quantify the morphology and brightness of the FIR emission seen towards the X-ray emitting halo and shock regions, it is necessary to subtract from the FIR maps the most prominent discrete sources associated with star formation regions and galaxies. To do this we devised a FIR source fitting technique which we describe in subsection 2.1.1. This source fitting technique also serves to fix the photometry and the extent of discrete sources, information that cannot be directly extracted from the maps due to the unknown level of mutual confusion.

2.1.1 The FIR map fitting technique and the FIR residual maps

The fitting technique models a preselected set of the most prominent discrete sources as a sum of elliptical gaussian convolved with the instrument PSF. Seven parameters are calculated for each source: amplitude, the peak coordinates, the two gaussian widths, the axis rotation angle and the local background (included to avoid removal of any diffuse emission components). The fit is performed simultaneously for the 10 brightest sources seen on the $70\mu\text{m}$ maps, (see Fig. 2.2): five compact sources (SQ A, HII SE, HII SW, SQ B, HII N), two sources to fit the emission from the AGN galaxy NGC 7319 (one for the central emission and one for a peripheral star formation region visible after the removal of the first component), two for the fit of the foreground galaxy NGC 7320 (one for the fit of the diffuse emission and one for a compact source) and one to fit the emission peaked in the middle of the shock region. The fit to the $70\mu\text{m}$ map is performed first, keeping all the fitting parameters as free variables. This is followed by a constrained fit to the $160\mu\text{m}$ map in which the relative position of the sources are fixed to the values obtained at

$70\mu\text{m}$. In addition, a further constraint was that we kept the same shape and axis orientation for the five compact sources, as inferred by the $70\mu\text{m}$ fit, allowing only a size change (to take into account the potentially more extended distribution of cold dust emission). This strategy was adopted because the higher resolution $70\mu\text{m}$ map places the strongest constraints to the position and morphology of sources in the FIR. Model images from the fitting technique are shown in Figs. 2.2 and 2.3. The best fit parameters and the inferred total flux densities are shown in Table 2.1. At both $70\mu\text{m}$ and $160\mu\text{m}$ the best fit model images are remarkably similar to the original maps. On the “deconvolved“ maps in each figure, it is possible to see the contribution from each gaussian to the final map. Interestingly enough, the source at the position of the shock is much more predominant at $160\mu\text{m}$ than at $70\mu\text{m}$, confirming the original impression that the emission in the shock region is brighter at $160\mu\text{m}$. It is also noteworthy that the position angle of the model source at $160\mu\text{m}$ is aligned with the north–south orientation of the X-ray emitting ridge whereas at $70\mu\text{m}$ no such alignment is apparent. At both 70 and $160\mu\text{m}$ the east–west width of the fitted elliptical gaussians at the shock position ($FWHM \approx 60''$) is larger than that of the X-ray shock ridge ($FWHM \approx 20''$). This indicates that the integrated emission is not necessarily entirely composed of emission from the shock ridge. A full description of the source fitting technique is given in Sect. 2.3.

To understand how the emission peaked in the shock region and the extended emission are distributed on the maps, we created FIR residual maps where the emission from all the sources fitted by the FIR map fitting technique, with the exception of the source associated with the shock, have been subtracted. The contours of these FIR residual maps are shown in Fig. 2.4 overlaid on HI, X-ray and FUV maps. As one can see, the emission on the FIR residual maps is uncorrelated with the HI distribution but well correlated with the soft X-ray flux. The FIR emission, as already seen on the original maps, peaks in the middle of the shock region and its overall extent is similar to the X-ray halo emission. At first sight this finding supports the idea that collisional heating is producing the observed FIR emission. However a large part of the residual FIR emission covers areas emitting significant luminosity at UV wavelengths. The presence of these radiation sources complicates

Source	RA	DEC	$\Delta_{70\mu\text{m}}$ (arcs)	$\Delta_{160\mu\text{m}}$ (arcs)	$F_{70\mu\text{m}}$ (mJy)	$F_{160\mu\text{m}}$ (mJy)
SQ A	22 35 58.81	33 58 51.08	16	15	134 ± 15	265 ± 86
HII SE	22 35 59.08	33 57 33.97	14	40	61 ± 9	186 ± 140
HII SW	22 35 56.10	33 57 43.10	11	ND	31 ± 5	ND
SQ B	22 36 10.54	33 57 20.52	14	36	63 ± 8	302 ± 34
N7319	22 36 3.760	33 58 33.03	12	30	616 ± 62	1192 ± 130
N7319 (HII)	22 36 3.01	33 59 00.0	24	ND	50 ± 8	ND
N7320	22 36 3.380	33 56 52.69	44	48	716 ± 73	1899 ± 196
N7320 (HII)	22 36 4.540	33 57 4.480	16	ND	111 ± 13	ND
HII N	22 36 03.132	33 59 34.6	23	42	52 ± 6	98 ± 41
SHOCK ¹	22 36 0.1	33 58 0.28	61	58	258 ± 30	1218 ± 230

Table 2.1: Fitted FIR source parameters: col1: FIR source; col2-3: Source center RA and DEC coordinates; col4-5: Averaged FWHMs of the sources; col6-7: Total flux densities at $70\mu\text{m}$ and $160\mu\text{m}$. Some of the sources are not detected at $160\mu\text{m}$ (ND = “non detected”)

¹ The SHOCK source on this table refers only to the gaussian used to fit the emission centered in the middle of the shock region. Therefore the quoted fluxes don’t represent the actual fluxes coming from that area. The emission from the shock region is given in the Table 2.

the interpretation of the dust emission in the shock region as well as for the extended emission (see Chaps. 4 and 5.1).

2.2 SQ Spitzer map photometry

Precise photometry of all these different emitting regions in SQ is required in order to elucidate the physical mechanisms that power dust emission and the related scientific implications. In the FIR the photometry is derived from the source fitting procedure (for the discrete sources) and from the FIR residual maps (for the shock

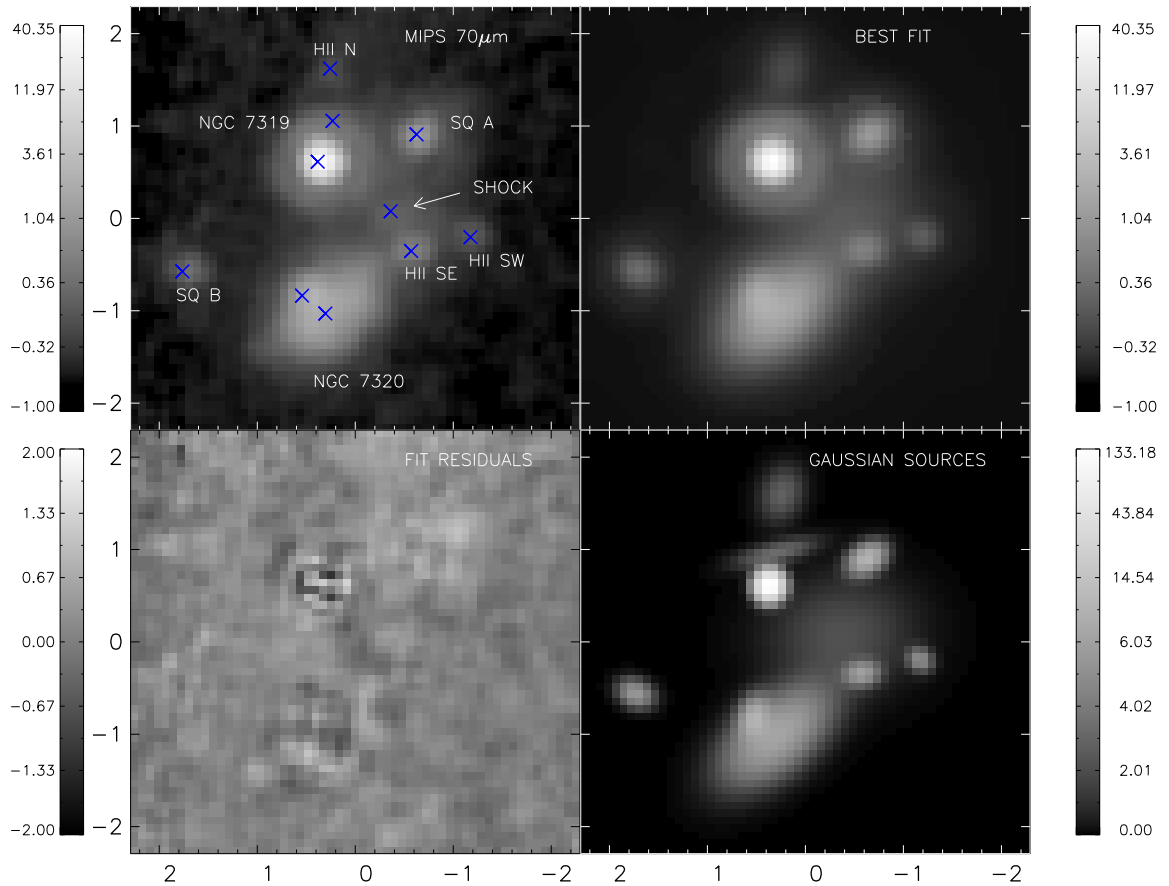


Figure 2.2: Fit results for the $70\mu\text{m}$ map. Top-left: original $70\mu\text{m}$ map; Top-right: best fit map; Bottom-left: fit residuals; Bottom-right: “deconvolved” map. The crosses on the original map identify the centers of the fitted sources. The units aside the color bars are MJy/sr. Note: The fit residual map, shown on the bottom-left panel, has all the fitted sources subtracted. It differs from the $70\mu\text{m}$ “FIR residual map”, whose contours are shown in the upper panels of Fig. 2.4, where the SHOCK source has not been subtracted.

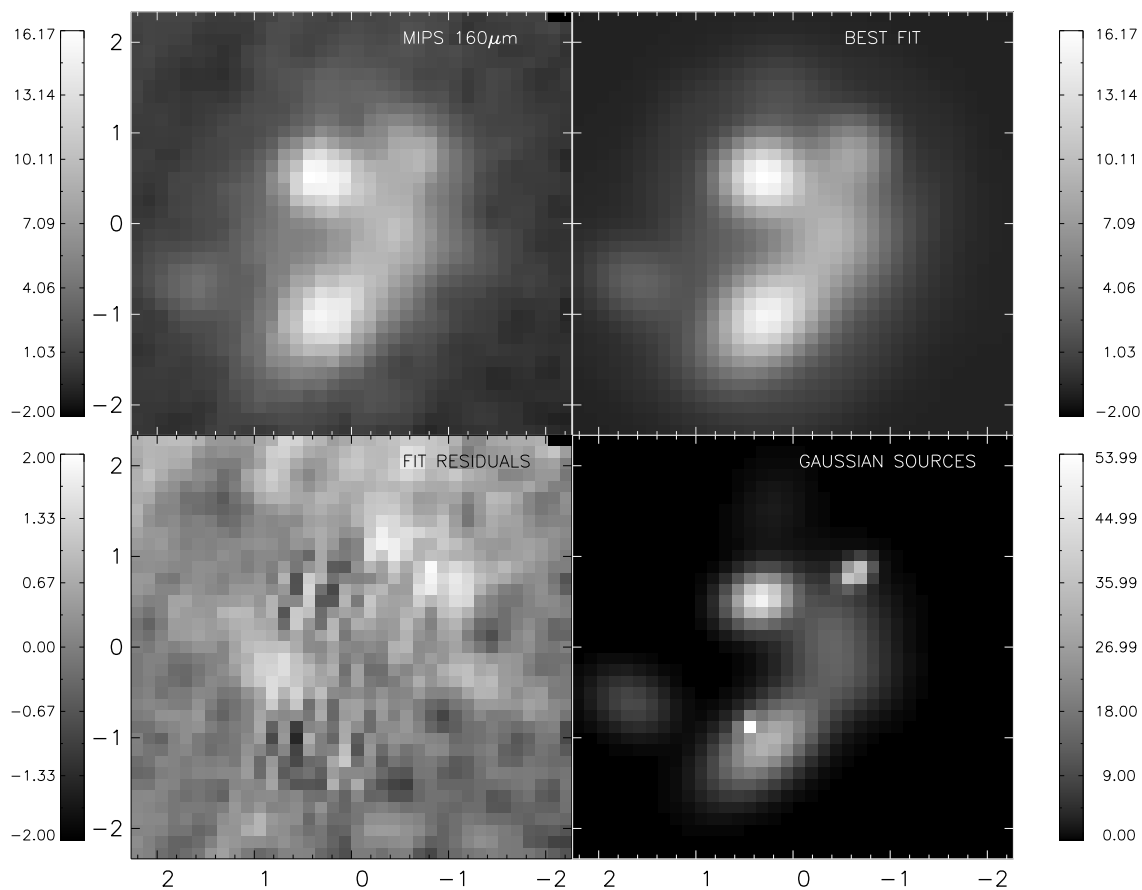


Figure 2.3: Fit results for the $160\mu\text{m}$ map. Top-left: original $160\mu\text{m}$ map; Top-right: best fit map; Bottom-left: fit residuals; Bottom-right: “deconvolved” map. The units aside the color bars are MJy/sr . Note: The fit residual map, shown on the bottom-left panel, has all the fitted sources subtracted. It differs from the $160\mu\text{m}$ “FIR residual map”, whose contours are shown in the lower panels of Fig. 2.4, where the SHOCK source has not been subtracted.

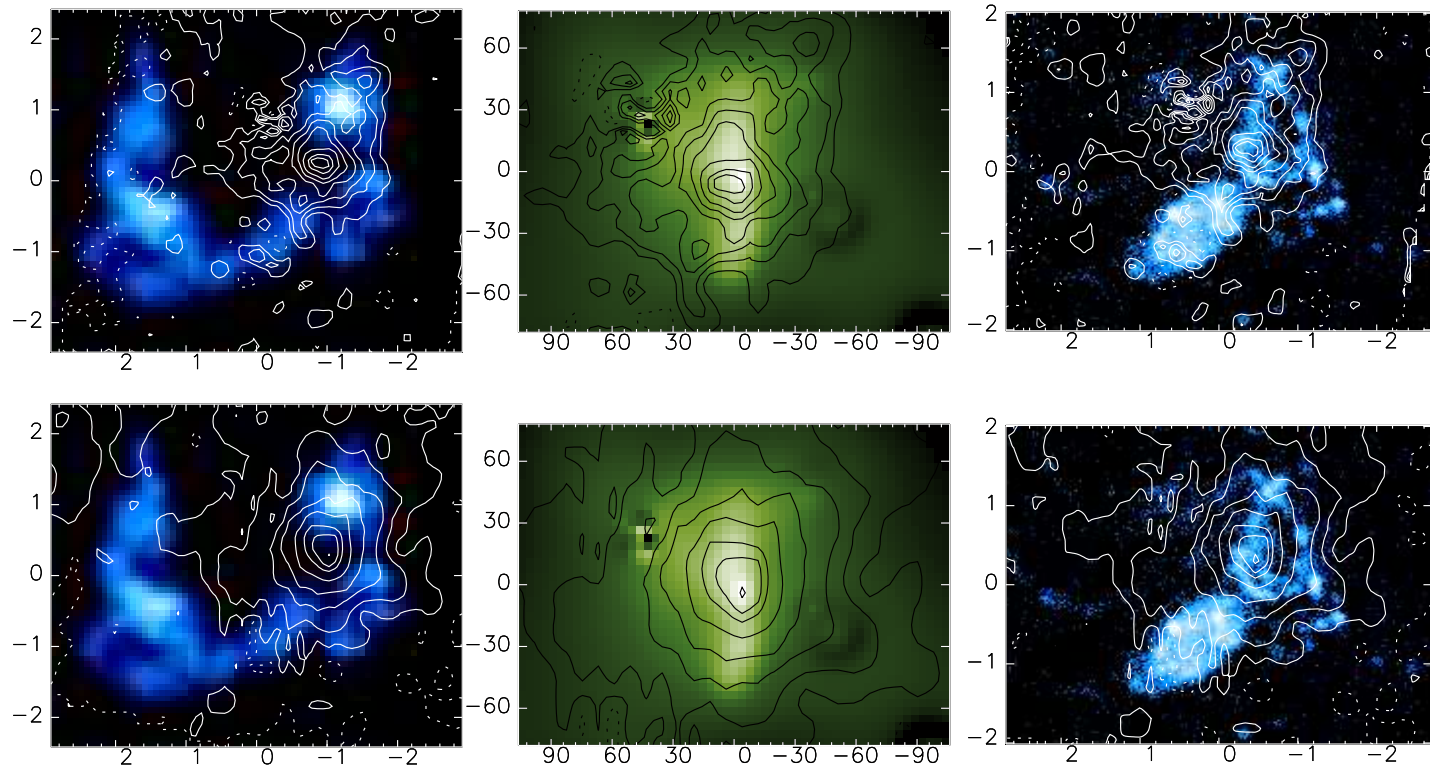


Figure 2.4: FIR residual maps (see Sect. 3.2) contours overlaid on HI (left panels), X-ray (middle panels) and FUV maps (right panels). The contours in the upper row are from the $70\mu\text{m}$ residual map while those in the lower row are from the $160\mu\text{m}$ residual map. The $70\mu\text{m}$ residual map contour levels are $-0.3, 0.3, 0.6, 0.9, 1.2, 1.5, 1.8, 2.1, 2.25$ MJy/sr and those for the $160\mu\text{m}$ residual map are $-0.4, 0.4, 1.2, 2.4, 3.6, 4.8, 6.0, 6.6, 7.2$ MJy/sr (the dashed lines are the negative contours, corresponding to -1σ level). The field of view is different in the three maps. The coordinates corresponding to $(0,0)$ are for the HI map $RA = 22^h36^m04.1''$ and $Dec = +33^\circ57'47.2''$, for the X-ray map $RA = 22^h35^m59.7''$ and $Dec = +33^\circ58'05.9''$, for the FUV map $RA = 22^h36^m01.6''$ and $Dec = +33^\circ57'42.1''$. The axis units are arcminutes for the HI and FUV maps and arcseconds for the X-ray map. Note that point sources have been removed from the X-ray map (see Fig. 1).

and the extended emission components). In the MIR the high resolution of the MIR 8 and $24\mu\text{m}$ maps allows a straightforward extraction of fluxes of the corresponding regions in SQ using aperture photometry. All results are summarized in Table 2.2.

2.2.1 Star formation regions and galaxies

The FIR map fitting technique, described previously, allows a precise measure of the flux coming from the compact star formation regions, the AGN galaxy NGC 7319 and the foreground galaxy NGC 7320, all well modelled by convolved elliptical gaussians (although some sources are not detected at $160\mu\text{m}$). This technique allowed us not only to obtain the total source fluxes but also to derive accurately the source extent. In Fig. 2.5, as an example, we show the contours of the “deconvolved” $70\mu\text{m}$ and $160\mu\text{m}$ emission at the position of SQ A overlaid on the $8\mu\text{m}$ and $24\mu\text{m}$ maps. The FIR emission has a MIR counterpart that peaks in the areas where FIR is higher. This is generally true for all the fitted FIR sources and it validates the use of apertures for the photometry of the compact sources at MIR 8 and $24\mu\text{m}$ whose sizes are derived by the FIR fitting technique. Specifically, at 8 and $24\mu\text{m}$ we used elliptical apertures having the same axial ratio and orientation as the $70\mu\text{m}$ best fit elliptical gaussian axis and semi-axis lengths equal to $2.17\sigma_{70\mu\text{m}}$ (this area includes 90% of an elliptical gaussian total flux). We took sizes based on the $70\mu\text{m}$ map fit because all the compact sources are clearly seen on that map. These apertures are depicted in red in Figs. 2.6 and 2.7.

The local background for the aperture photometry has been estimated on regions located nearby the central source, where other peaks of emission are not clearly seen (see green circles on Figs. 2.6 and 2.7). In this way we are confident that the background level has not been overestimated due to contamination by surrounding sources. We didn’t apply aperture correction for the photometry at $8\mu\text{m}$ because this is close to unity for the chosen apertures (typical aperture size about 10 pixels), as reported by the IRAC data Handbook. At $24\mu\text{m}$ the chosen apertures typically delimit the first outer ring of the PSF. In this case we applied an aperture correction equal to 1.16 (MIPS data Handbook). For the MIR photometry of the galaxies

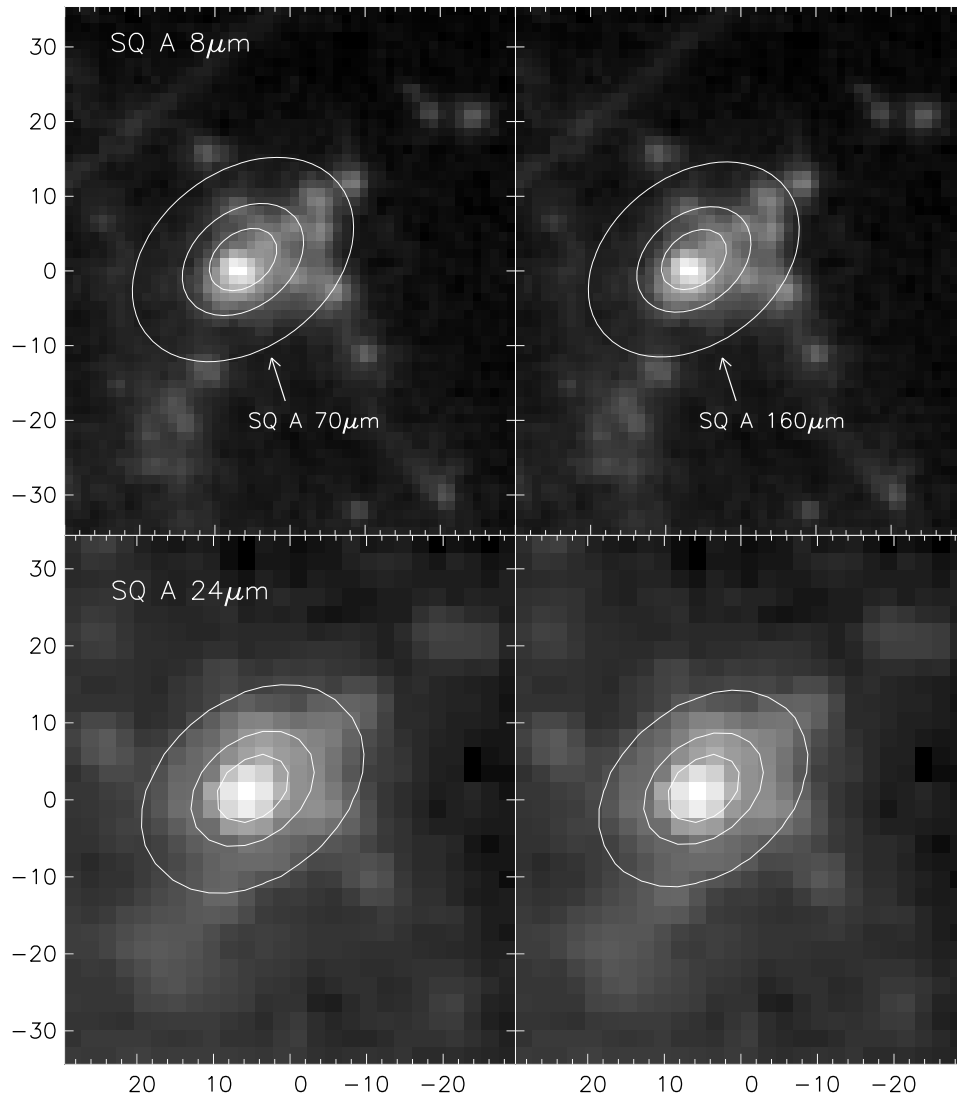


Figure 2.5: “Deconvolved” 70 μ m and 160 μ m SQ A emission contours overlaid on 8 μ m (upper row) and 24 μ m (lower row) maps. Units on the axis are arcseconds.

NGC 7319 and NGC 7320 we used large apertures covering most of the emission from these objects and we didn't apply aperture corrections because of the large integration area.

The uncertainties on the MIR photometry are given by the quadratic sum of the following contributions: 1) error on the aperture correction; 2) flux calibration uncertainty; 3) background fluctuations. Since we used elliptical apertures, instead of typical circular apertures, we rather conservatively assumed that the relative error on the aperture correction is 10% (note that this error is applied only to aperture photometry at $24\mu\text{m}$). The flux calibration relative uncertainty is equal to 4% (IRAC and MIPS Handbook) while the error introduced by background fluctuations is derived from the variance of the background mean values in the several areas we selected nearby the sources. The measured fluxes and uncertainties for both MIR and FIR wavelengths are given in Table 2.2.

Since we are using different methods to derive the source fluxes on the MIR maps and the FIR maps, it is important to check that these two photometric techniques give consistent results. To verify this, we performed the source fitting technique on convolved MIR maps and derived the source fluxes exactly as we did for the FIR maps. Details and results of this test are shown in Sect. 2.3.

2.2.2 Shock region

Fig. 2.8 show the east-west profiles, along a line passing through the center of the shock ridge, extracted from the FIR residual maps, the X-ray and the VLA 21 cm radio continuum maps convolved to the resolution of the $160\mu\text{m}$ map ($FWHM \approx 40''$). From these profiles, one can see that the FIR width is significantly larger than the shock ridge width as seen both in the X-ray and Radio. Using the current data it is impossible to say if this discrepancy is due to confusion with fainter unrelated infrared sources or to a systematic change in the width of the emitting region of the shock between the X-ray and the FIR. Nevertheless we estimated the flux coming from the shock ridge by fitting the FIR residual maps with a simple two component model: a PSF convolved uniform ridge, used to fit the dust emission in

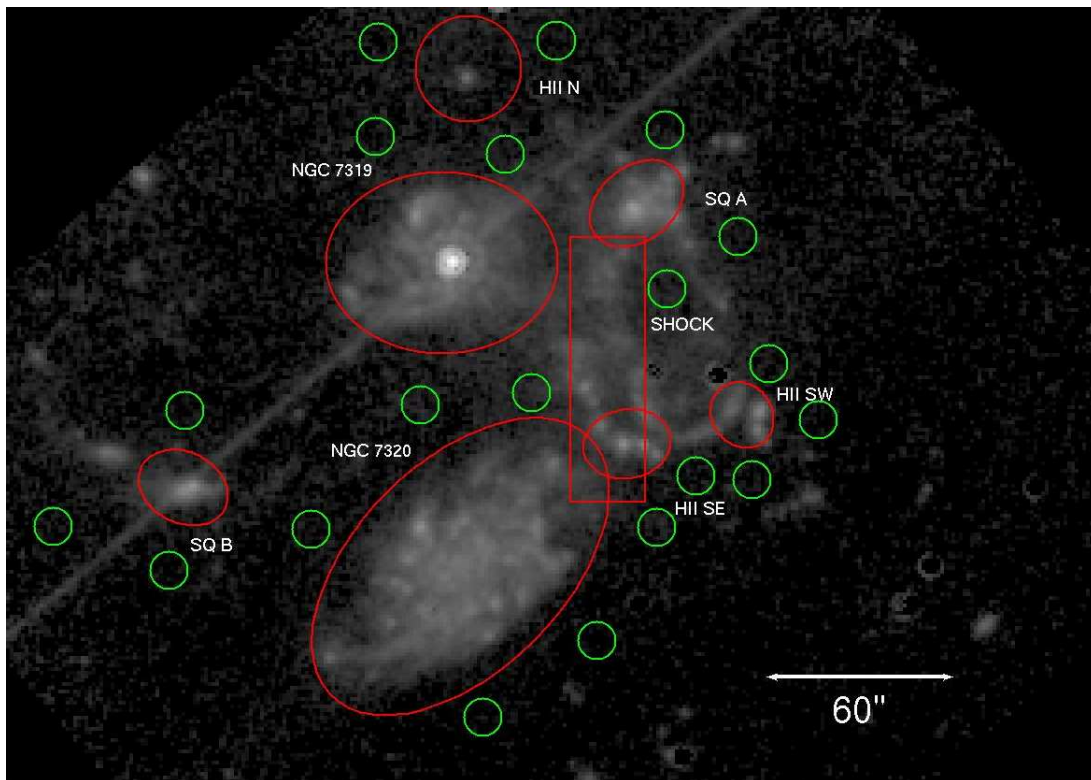


Figure 2.6: Apertures for source photometry on the Spitzer IRAC $8\mu\text{m}$ map. Integration areas are delimited in red while background areas in green. The straight line passing through the AGN galaxy and SQB is a map artifact.

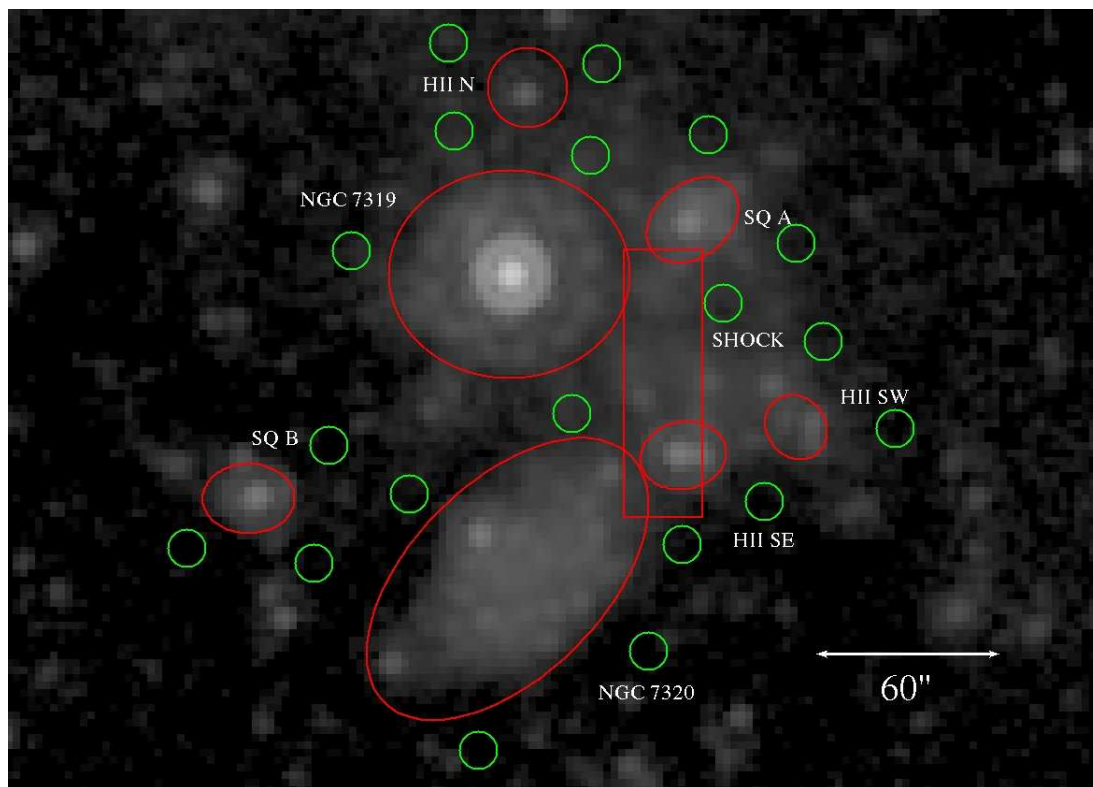


Figure 2.7: Apertures source photometry on the Spitzer MIPS 24 μ m map. Integration areas are delimited in red while background areas in green.

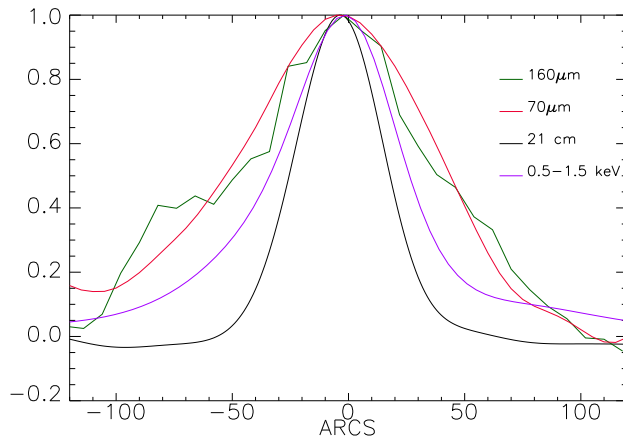


Figure 2.8: East–West profile of the shock region at several wavelengths. The profiles for the $70\mu\text{m}$, X-ray and Radio maps are derived after convolution to the resolution of the $160\mu\text{m}$ map ($FWHM = 40''$). The profiles are derived from an horizontal strip passing through the center of the shock region ($RA = 22^h35'59.7, Dec = +33^\circ58'14.2''$) and of vertical width equal to $10''$.

the shock region and whose size ($20'' \times 80''$) were derived from X-ray data, plus a uniform component. In this procedure the level of the fitted uniform component is influenced by the fact that the actual FIR source is more extended than the X-ray source. Taking into account the ambiguity in identifying all the flux from the more extended FIR emission with the shock, we have assigned extremely conservative flux uncertainties. Specifically, the upper and lower limits defined by the quoted error bars in Table 2.2 are the fluxes contributed by the uniform emission component underlying the solid angle of the shock ridge (convolved with the PSF) in the cases the uniform emission component has a brightness equal to twice or zero times the value given by the fit. To measure the MIR 8 and $24\mu\text{m}$ emission from the shock region, we simply integrated the emission in the same rectangular area used before to define the shock ridge component in the fit of the FIR residual maps. The adopted apertures are shown in Figs. 2.6 and 2.7. Before the integration we masked all the areas inside the apertures we used for the photometry of other sources, because the MIR emission in that areas is mainly connected with the corresponding sources that we fitted and subtracted from the FIR maps before the measure of the shock

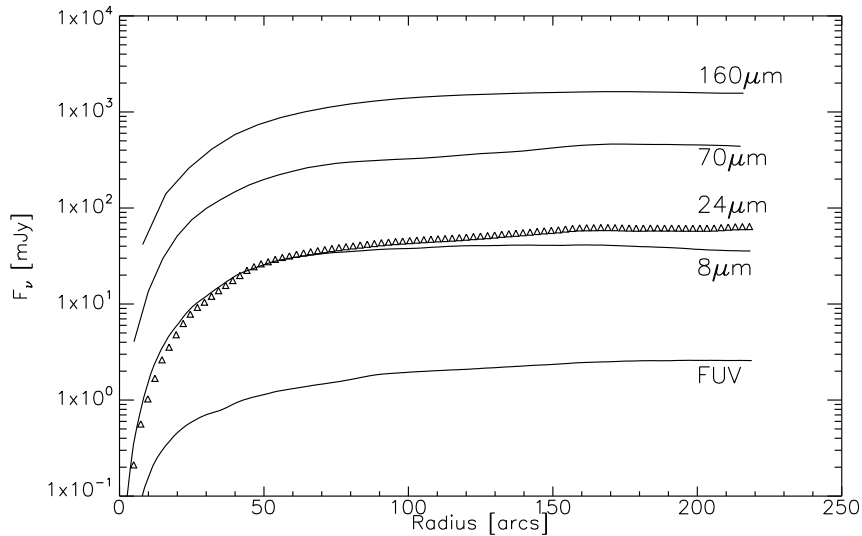


Figure 2.9: Radial curves of growth of the FUV, MIR and FIR emission after masking or subtraction of star formation regions and the two galaxies NGC 7320 and NGC 7319 (see text). The zero on the X-axis corresponds to the center of the shock region: $RA = 22^h 35^m 59.7, Dec = +33^\circ 58' 14.2''$

region flux. For the fraction of the masked regions that falls inside the shock region integration area we assumed that the surface brightness is equal to the average brightness on the other regions inside the aperture. The background level has been measured on areas around the rectangular aperture where no peaks of emission are clearly seen. The quoted error on the integrated fluxes is the sum of the contributions due to background fluctuation and flux calibration error.

2.2.3 Extended FIR emission

We have measured the amount of extended flux on the FIR residual maps within a radius of $90''$ from the shock center, an area approximately equal to that covered by the X-ray HALO region as defined in Trinchieri et al. (2005) (see Fig. 1.7). We performed this flux measurement in the following way. First we constructed radial curves of growth of the integrated emission on the FIR residual maps starting from the shock center. These curves of growth are shown in Fig. 2.9. As one can see, the integrated emission continues to grow somewhat beyond the $90''$ radius. However we

considered only the flux within this limit because it can be directly related to the X-ray Halo extent. We took the curve of growth values for the integrated fluxes at $90''$ and we subtracted the contribution from the shock region, estimated in Sect. 2.2.2. The uncertainties on the fluxes are mainly due to the mutual contamination between shock ridge and extended emission. Therefore we assumed the same conservative errors that we assigned to the shock region FIR fluxes. For the estimate of the extended MIR emission we have used an analogous method. We constructed radial curves of growth, starting from the shock region center, after having masked all the compact sources and galaxies whose photometry has been described in Sect. 2.2.1 (note that the shock region is not masked). For the calculation of the MIR curves of growth we took into account the missing areas, those that we masked, assuming that their brightness is equal to the average brightness inside the circular annuli passing through them. The derived curves are shown in Fig. 2.9. Exactly as for the FIR measurements, we took the value of the curve of growth at $90''$ and subtracted the emission from the shock region in order to obtain the integrated emission from the extended area corresponding to the X-ray halo. The flux uncertainties, in this case, are derived summing quadratically background fluctuation, calibration errors and the error on the shock ridge flux.

2.3 Multisource fit of SQ FIR maps

In this section we explain in more detail the FIR map fitting technique that we devised to model the sources on the FIR maps. As seen in Sect. 2.1.1 and 2.2.1, we applied this technique to extract these sources from the FIR maps but also to perform their photometry. The fitting technique we developed is similar to the CLEAN algorithms used in radio astronomy but with some additional characteristics: 1) all the sources are fitted at the same time; 2) an intrinsic finite source width is allowed. Our basic assumption is that all the sources we model are sufficiently well described by elliptical gaussians or a combination of them. This is not necessarily true because some sources can, in principle, differ significantly from this simple shape. However this simple approach has been sufficient for a good fitting of the FIR

Source	$F_{8\mu\text{m}}$ (mJy)	$F_{24\mu\text{m}}$ (mJy)	$F_{70\mu\text{m}}$ (mJy)	$F_{160\mu\text{m}}$ (mJy)
SQ A	7.9 ± 0.5	11 ± 2	134 ± 15	265 ± 86
HII SE 7318b	3.4 ± 0.4	7.5 ± 1	61 ± 9	$186(51) \pm 142(40)$
HII SW 7318b	2.5 ± 0.1	2.4 ± 0.35	31 ± 5	ND
SQ B	3.1 ± 0.15	5.6 ± 0.8	63 ± 8	$302(120) \pm 34(13)$
NGC 7319	68 ± 3	185 ± 8	666 ± 67	1192 ± 130
NGC 7320	45 ± 3	38 ± 2	827 ± 85	1899 ± 196
HII N 7319	0.69 ± 0.07	1.1 ± 0.2	52 ± 6	$98(78) \pm 41(33)$
Shock region	8.1 ± 0.8	6 ± 1.5	80 ± 30	506 ± 200
Extended emission	29 ± 2	40.6 ± 5	233 ± 30	805 ± 200

Table 2.2: IR fluxes of the set of discrete sources detected on the Spitzer $70\mu\text{m}$ map. The $8\mu\text{m}$ and $24\mu\text{m}$ fluxes are obtained from aperture photometry while the $70\mu\text{m}$ and $160\mu\text{m}$ fluxes for the galaxies and compact star formation regions are the results of the FIR map fitting technique. The FIR fluxes from the shock region are obtained by the fitting of the FIR residual maps. The MIR and FIR values for the extended emission are derived from the curves of growth of the MIR and FIR maps (see Sect. 2.2.3). The values in brackets are the $160\mu\text{m}$ fluxes within the size of the $70\mu\text{m}$ emission.

maps. The function $F(x, y)$, describing an elliptical gaussian on a map, is defined by the following formulas:

$$F(x, y) = B_{loc} + A \times e^{-U/2} \quad (2.1)$$

$$U = (x'/\sigma_x)^2 + (y'/\sigma_y)^2 \quad (2.2)$$

$$x' = (x - x_s) \cos \theta - (y - y_s) \sin \theta \quad (2.3)$$

$$y' = (x - x_s) \sin \theta + (y - y_s) \cos \theta \quad (2.4)$$

The first two equations define the shape of the elliptical gaussian while the last two are the coordinate transformations between the map and the frame defined by the elliptical gaussian axis. For each source the fitting procedure has to provide 7 parameters: A (the gaussian amplitude), (x_s, y_s) (the position of the source center), (σ_x, σ_y) (the gaussian widths in two orthogonal directions), Θ (the rotation angle of the gaussian axis from the array axis) and an offset value B_{loc} (the local background for each source).

A real image is not just the sampling of the original signal, of course, but it's the sampling of the convolution of the signal with the point spread function (PSF) of the telescope optics–detector instrument. Using the program STINYTIM², we obtained theoretical PSFs of the MIPS instrument for both 70 and 160 μm bands. Fig. 2.10 and 2.11 show the theoretical PSFs for the 70 μm and 160 μm bands and their profiles. In panel (b) of these figures, it is shown also the radial profile of an empirical PSFs (kindly provided by G. Bendo). Although there are some intrinsic differences between empirical and theoretical profiles, we decided to use theoretical PSFs because they can be sampled at any desired rate and don't contain noise that would be added to the fit (however we made some tests to determine the level of uncertainty introduced by using theoretical PSFs instead of real ones in our fitting procedure. We have found that the difference on the final results is negligible compared to other sources of error, e.g. only $\approx 5\%$ on the inferred source fluxes). The first step of our fitting procedure is to assume a distribution of elliptical gaussian sources, with initial trial values of the parameters, in an array of the same size of the

²by John Krist for the Spitzer Science Center:

<http://ssc.spitzer.caltech.edu/dataanalysis/tools/contributed/general/stinytim/>

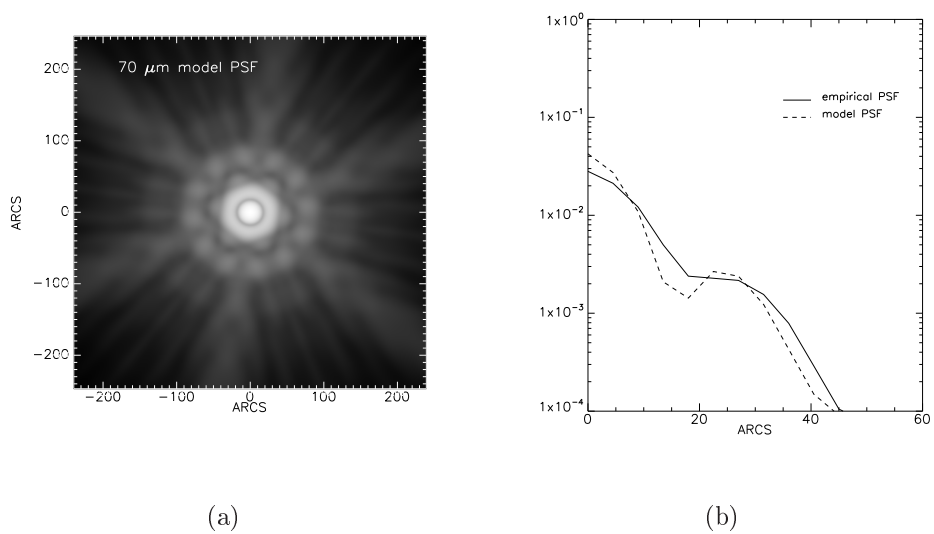


Figure 2.10: a) Theoretical $70\ \mu\text{m}$ PSF; b) Average radial profiles of empirical and theoretical $70\ \mu\text{m}$ PSFs.

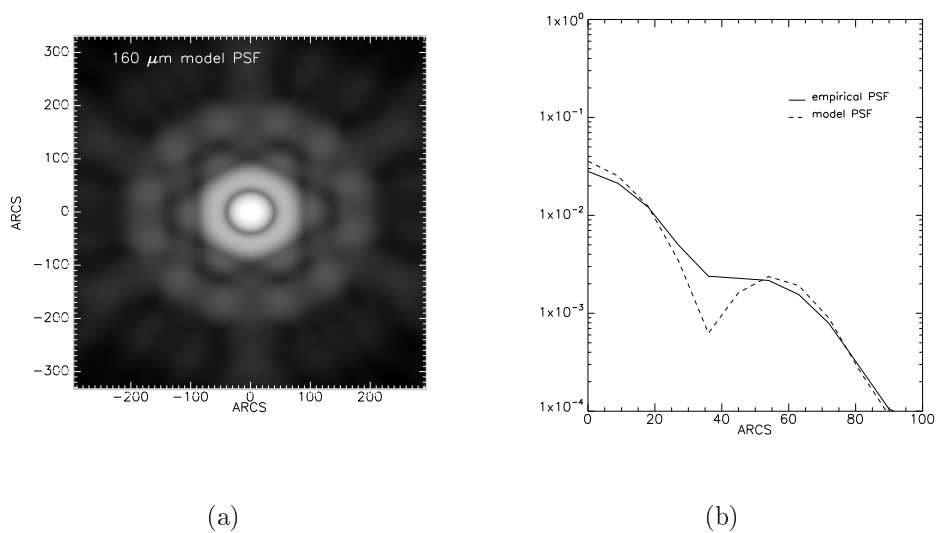


Figure 2.11: a) Theoretical $160\ \mu\text{m}$ PSF; b) Average radial profiles of empirical and theoretical $160\ \mu\text{m}$ PSFs.

data. First from a direct inspection of the FIR maps and then after some iterations, we identified 10 main sources to be fitted using elliptical gaussians (see Fig. 2.2): two for NGC 7320 (one for the disk emission plus one for a compact star formation region), one each for SQ A and SQ B, two for NGC 7319 (one for the circumnuclear emission plus one for a star formation region), one for a source located north of NGC 7319 (HII N), two for NGC 7318b (the two compact star formation regions located on the southern spiral arms), one for a source peaked in the middle of the shock region. Convoluting this array with a theoretical PSF, an artificial image is obtained that can be compared with the real data. Varying the parameters of the elliptical gaussians, it is possible to improve the agreement between artificial and real images until a certain degree of accuracy is reached. To minimize χ^2 and find the best fit model parameters, we used the Levenberg–Marquardt (LM) algorithm (see Bevington 1992), implemented by the IDL routine MPFIT2DFUN³. Although this algorithm is less dependent on the initial trial values of the parameters, compared with other χ^2 minimization methods, the results are inevitably dependent on these. Therefore it is a good rule to assign the initial values as close as possible to the real ones (or better to which we believe are the real ones). The criteria we used to choose the initial values for the free parameters are the following:

- 1) Amplitude: any number of the order of the peak amplitude of the source (this fitted parameter has been found almost independent from the initial value);
- 2) Position: initial positions near the peaks of the sources;
- 3) Gaussian Widths: derived approximately from the apparent width of the source;
- 4) Rotation angle: any number.
- 5) Local Background: initial value equal to zero.

As one can notice, the choice of the initial values doesn't require to know in advance any parameter but the approximate positions of the source centers and roughly the sizes of the gaussians. All this information can be easily derived from the data. The fitting procedure improves the quality of the results (in the sense that we obtain a smoother residual map and a lower reduced χ^2) if we consider only the regions close

³written by Craig Markwardt: <http://cow.physics.wisc.edu/~craigm/idl/fitting.html> for details on the χ^2 minimization routine

to the sources for the fit. Therefore, we created a mask to exclude all the pixels that are too distant from the calculation, that is more than 2-3 times the apparent sizes from the source centers.

The fitting technique as described until now has been applied successfully to the $70\mu\text{m}$ FIR map. The fitting of the $160\mu\text{m}$ map has been performed in a slightly different way because one cannot clearly see on this map all the compact sources that are detected on the $70\mu\text{m}$. This effect is most probably due to both lower resolution and intrinsic color differences. Since our goal was to produce consistent SEDs of the main sources in SQ, we introduced new constraints for the fit of the $160\mu\text{m}$ map. We assumed that the centre position of each source on the $160\mu\text{m}$ map is the same as derived from the $70\mu\text{m}$ map fitting. We only allowed a common shift of all the source positions in order to correct possible small differences in the astrometry of the two maps. Then we assumed that the orientation angles and the ratio of the elliptical gaussian axial widths (σ_x, σ_y) for the compact sources (SQ A, HII SE, HII SW, SQ B, HII N and the compact star formation regions in NGC 7319 and NGC 7320) are the same as those inferred from the $70\mu\text{m}$ map fit. Therefore we assumed that the shape of the emitting compact sources is similar at 70 and $160\mu\text{m}$ even if the size can be different. This is actually expected because colder emission can come from regions that are simply farther away from the central heating source in case of star formation regions.

Figs. 2.2 and 2.3 show the results of our fitting technique for the $70\mu\text{m}$ and $160\mu\text{m}$ maps in four panels: a) the background subtracted Spitzer FIR map of SQ, b) the best fit image obtained with our method, c) the fit residuals and d) the "deconvolved" map (that is actually the map showing the elliptical gaussians whose PSF convolution gives the best fit map). As one can see, this method produces best fit maps with remarkable similarity to the original maps ($\chi^2_{70\mu\text{m}}/N_{\text{free}} = 0.8$, $\chi^2_{160\mu\text{m}}/N_{\text{free}} = 0.7$). The "deconvolved" map at $70\mu\text{m}$ shows, apart from the emission of the foreground galaxy NGC 7320 and AGN galaxy NGC 7319, the several discrete compact sources that are responsible for the several peaks seen on the real map. There is a rather extended source that peaks in the middle of the shock region, even though some excess of emission is still seen on the fit residual map at

this position suggesting that the accuracy of the fit is not very good for this faint source. At $160\mu\text{m}$ the emission is dominated by the AGN galaxy, the foreground galaxy and the source peaked on the shock region. It is quite interesting that the gaussian used to fit the emission at the position of the shock is very well aligned along the main axis of the shock ridge. However the east–west width of this gaussian is too large to be related only to the X-ray ridge (see Sect. 2.2.2)). Some compact star formation regions are undetected (or only marginally detected) at $160\mu\text{m}$, as we somehow expected, as no peaks are clearly seen at their position.

The main fitted parameters and the derived flux densities for each of the fitted sources can be found in Table 2.1. The uncertainties on the integrated fluxes are derived from the covariance matrix provided by the LM χ^2 minimization algorithm. For the estimate of the error on each point of the map, necessary to evaluate χ^2 we considered the variance of background fluctuations on each map. On the final integrated fluxes for each source a 10% error is added due to flux calibration uncertainties (MIPS data handbook). As one can notice from tab.2.1, the inferred $160\mu\text{m}$ sizes for the AGN galaxy NGC 7319 and the compact sources HII SE, SQ B and HII N are much larger than the $70\mu\text{m}$ size. In case of the AGN galaxy the size difference can be physically understood if one thinks that additional warm emission come from the central part of the galaxy and, therefore, the $70\mu\text{m}$ flux is more peaked towards the center (see also discussion in Sect. 4.4). The larger $160\mu\text{m}$ size for the compact sources arises because the fit procedure tends to fit also extended diffuse emission around the main central source, most probably produced by unresolved nearby sources. For these last sources we calculated from the deconvolved $160\mu\text{m}$ gaussians the amount of flux within one $70\mu\text{m}$ *FWHM* from the peak. These reduced $160\mu\text{m}$ fluxes are quoted within brackets in Table 2.2.

Comparison between results obtained by the fitting technique and aperture photometry

As it will be seen in Sect. 3.1, we performed source SED fitting including MIR and FIR measurements, performed respectively using aperture photometry and the map fitting technique. Therefore, it is important to understand how different the fluxes

obtained by the fitting procedure are compared to those we would have obtained by aperture photometry on a high resolution map. To quantify this difference, we made a test using the higher resolution $24\mu\text{m}$ map where dust emission morphology looks remarkably similar to the $70\mu\text{m}$ emission (at least if one considers the main sources of emission). We convolved the $24\mu\text{m}$ MIR map to match the resolution of the $70\mu\text{m}$ map, resampled the map to match the pixel size of the $70\mu\text{m}$ map and then performed the gaussian fitting technique on the convolved map. The convolution has been done using the kernel function created by Carl Gordon (Gordon et al. 2008). For the fit we assumed the same distribution of gaussians as in the fit of the FIR maps, but leaving all the parameters free. The convolved map and the fit results are shown in Fig. 2.12. In Table 2.3 and in Fig. 2.13 we compared the results from aperture photometry (described in Sect. 2.2.1) and gaussian fitting. For all but one source (HII SW) the fluxes derived using the two different methods are consistent within the uncertainties and also the inferred source sizes are close to those found at $70\mu\text{m}$ (the problem with HII SW arises because of the vicinity of the nucleus of NGC 7318a that is much brighter in the MIR than in the FIR). Based on the results of this test, we are confident that the two photometric techniques give consistent results.

2.A Observations and Data Reduction

In this thesis we have used Spitzer maps from two Guest Observer (GO) programs making use of continuum data at $24, 70$ and $160\mu\text{m}$ from the MIPS instrument (Rieke et al., 2004). From the GO #40142 (PI: Appleton, P.) we took the $24\mu\text{m}$ map and from the GO #3440 (PI: Xu, K.) the 70 and $160\mu\text{m}$ maps. In addition, an image of SQ at $8\mu\text{m}$, taken with the IRAC instrument (Fazio et al., 2004) and downloaded from the Spitzer Science Center (SSC) archive, was also used. In the following we provide details of the data reduction for the Spitzer FIR maps, performed by Nanyao Lu at the SSC. The $24\mu\text{m}$ map has been already presented by Cluver et al. (2010) and we refer to that paper for technical details about the data preparation.

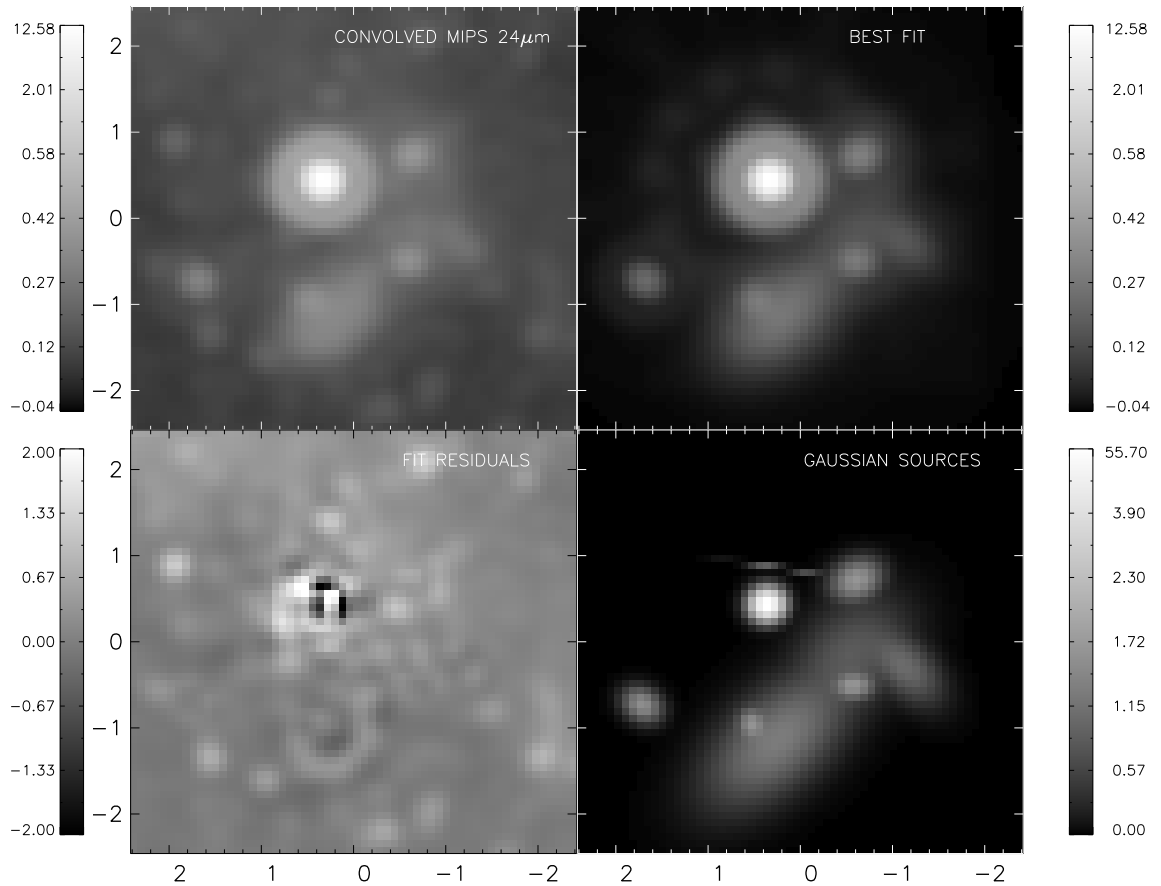


Figure 2.12: Convolved $24\mu\text{m}$ map fit. Top-left: Convolved $24\mu\text{m}$ map; Top-right: Best fit map; Bottom-left: Fit residuals; Bottom-right: deconvolved gaussian map

Source	$F_{24\mu\text{m}}^{\text{ap}}$ (mJy)	$F_{24\mu\text{m}}^{\text{fit}}$ (mJy)	$\Delta_{70\mu\text{m}}^{\text{fit}}$ (arcs)	$\Delta_{24\mu\text{m}}^{\text{fit}}$ (arcs)
SQ A	11 ± 2	12 ± 0.5	16	15
HII SE 7318b	7.5 ± 1	6.7 ± 0.4	14	12
HII SW 7318b ¹	2.4 ± 0.35	6 ± 0.6	11	24
SQ B	5.9 ± 0.8	5.6 ± 0.8	15	12
NGC 7319 ²	185 ± 8	195 ± 8	12	12
NGC 7320 ²	38 ± 2	40 ± 2	44	43
HII N 7319	1.1 ± 0.2	ND ³	22	ND ³

Table 2.3: Comparison of photometry results at $24\mu\text{m}$ obtained with aperture photometry and the gaussian fitting technique. Col. 1: Source name; col. 2: aperture photometry fluxes; col. 3: fluxes from the gaussian fitting technique ; col. 4: average source FWHMs as derived from the $70\mu\text{m}$ map fitting ; col. 5: average source FWHMs as derived from the $24\mu\text{m}$ convolved map fit.

¹This source is the only source, detected by the fitting technique, whose inferred fluxes are considerably different. The size of the gaussian that fit the emission on the $24\mu\text{m}$ convolved map is much larger than that found at $70\mu\text{m}$. The reason for this is the contamination from the nearby nucleus of NGC 7318a that emits strongly in the MIR but not in the FIR.

²For NGC 7319 (the AGN galaxy) and NGC 7320 (the foreground galaxy) the apertures are chosen such to cover the entire emission of the galaxies. In the fitting procedure these sources are modeled with two gaussians, one for the centrally peaked emission and one for a peripheral HII region. The sizes shown in column 4 and 5 refer to the central source that contribute most of the flux.

³ND: non detected.

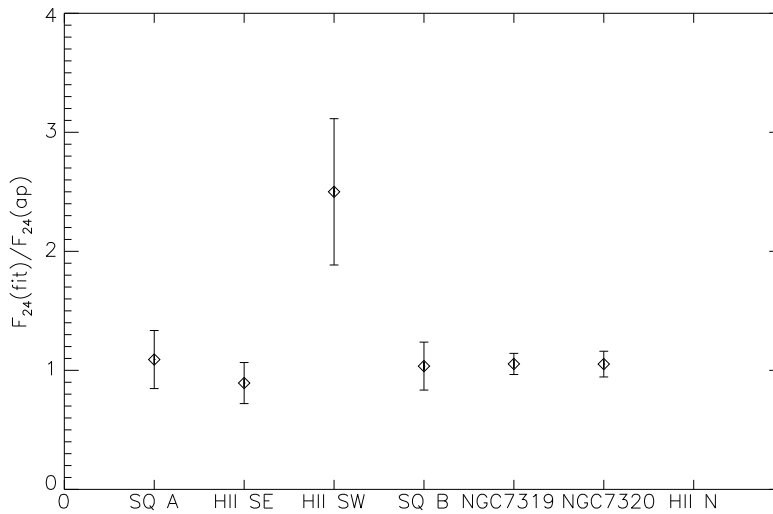


Figure 2.13: Ratio between fluxes inferred from the fitting technique and from aperture photometry for the sources on the $24\mu\text{m}$ map.

– MIPS $70\mu\text{m}$ and $160\mu\text{m}$ data reduction

The MIPS $70\mu\text{m}$ and $160\mu\text{m}$ data are from Spitzer pipeline version S11.0.2. In the pipeline default mosaic images, there are a few residual instrumental artifacts that are particularly noticeable at $70\mu\text{m}$. Because of this, these pipeline images were not used in this thesis. In their place, new images were used in which the instrumental artifacts were reduced by performing additional data reduction steps on the “basic calibrated data” (BCD) frames.

Specifically, for the $70\mu\text{m}$ data, we observed an overall signal drift in time. To remove this, we masked out those pixels of each of the 468 non–stim BCD frames that are within a radius of $125''$ of the SQ center (RA=339.0181d, DEC=33.969183d; J2000). For each BCD frame, a median was calculated from all unmasked pixels. These medians were plotted as a function of the BCD frame index (1 to 468). The resulting plot shows a clear discontinuity at frame index 313. We fit the sections prior to and post this discontinuity separately with a cubic spline function of order 1 or 2. The two fitted curves were connected to form one curve covering all the BCD frames. After being normalized by its mean, this curve was divided into the index–ordered BCD frames to remove the signal drift in time. The next step was to

create a sky flat image by median filtering only unmasked data for a given detector pixel. The resulting sky flat image was normalized by its mean, and subsequently divided into each unmasked BCD frames. Finally, we used Spitzer MOPEX tool to mosaic these improved BCD frames into our final image used in this paper. With a much flatter sky background, our own mosaic image is significantly better than the pipeline counterpart.

For the MIPS $160\mu\text{m}$ data, a similar procedure was used with all 522 non-stim BCD frames. In this case, the detector signal drifts in time differ significantly among individual readout modules. As a result, our signal drift removal was attempted on per readout module basis.

Background subtraction was performed by fitting a tilted plane to the maps, after masking a large area covering the main group and, in the case of the $160\mu\text{m}$ map, the galaxy NGC7320c (that lies outside the field of view shown in Fig. 2.1).

Chapter 3

Modelling the dust emission SEDs of SQ sources

3.1 Modelling the Infrared SEDs

The spectral energy distribution (SED) of dust emission is determined by the heating mechanism, the intensity and color of the radiation fields (for the case of photon heating), the temperature and density of the hot plasma (for the case of collisional heating) and by the amount, size distribution and chemical composition of the emitting grains. Ideally one would solve for the distribution of photon sources, hot plasma and grains using a self consistent radiation transfer analysis to fit the entire X-ray/UV/Optical-MIR/FIR SED for each source, analogous to the treatment of photon heated dust in disk galaxies and starburst galaxies (see Popescu & Tuffs (2010) for a recent review). However, due to the extra dimension of collisional heating and the unusual geometry of the optical/UV and infrared emission from SQ, this approach would require a very individualized treatment which is well beyond the scope of this work. We therefore adopt here a hybrid approach fitting just the MIR/FIR SED with superpositions of dust emission templates where each template is appropriate for specific dust emission regions: HII/photodissociation regions (PDR), diffuse photon-powered dust emission, AGN torus emission and collisionally heated dust embedded in hot X-ray plasma. Each of these templates is calculated

self consistently in terms of physical input parameters as described in detail in Sect. 3.2. In this approach the amplitude of the HII/PDR template, derived from the model of Dopita et al. (2005) and Groves et al. (2008) and shown in Fig. 3.7 (left panel), quantifies the obscured component of on-going star formation, whereas the amplitude of the diffuse dust emission template (shown in Fig. 3.8) quantifies dust emission powered by longer range photons, to which older stellar populations can also contribute. In the latter case a family of SEDs is calculated according to the strength and color of the radiation field, which are both expected to vary according to radiation transfer effects, and the relative contribution of young and old stellar populations. A family of SEDs are also calculated for the collisionally–heated dust emission template (Fig. 3.10), corresponding to a range of plasma parameters and to different grain size distributions, thus accounting for the expected effect of the plasma on the grain size distribution. For both the photon heated and collisionally heated dust emission templates, the stochastic emission from impulsively heated grains, which is important to determine the MIR emission, is calculated. In the case of the AGN template SED, we have used the existing self-consistent model of Fritz et al. (2006) (right panel of Fig. 3.7).

The fits were done by minimizing χ^2 for each source, defined as:

$$\chi^2 = \sum \left(\frac{F_{\nu i}^{\text{model}} - F_i^{\text{obs}}}{\sigma_i} \right)^2 \quad (3.1)$$

where F_i^{obs} and σ_i are the observed flux densities and their associated uncertainties respectively, and F_{ν}^{model} is the corresponding model prediction which is related to a given theoretical spectra F_{ν} through $F_{\nu}^{\text{model}} = K F_{\nu}$. The color correction, K , for each Spitzer band is calculated according to the formulas provided by the IRAC and MIPS data handbooks:

$$K = \frac{\int (F_{\nu}/F_{\nu_o}) (\nu/\nu_o)^{-1} R d\nu}{\int (\nu/\nu_o)^{-2} R d\nu} \quad (\text{IRAC}) \quad (3.2)$$

$$K = \frac{\int \frac{F_{\lambda}}{F_{\lambda_o}} R_{\lambda} d\lambda}{\int \left(\frac{\lambda_o}{\lambda}\right)^5 \frac{e^{\frac{hc}{\lambda_o k T_o}} - 1}{e^{\frac{hc}{\lambda k T_o}} - 1} \lambda R_{\lambda}} \quad (\text{MIPS}), \quad (3.3)$$

where the subscripts ν_o and λ_o refer to the band reference frequency or wavelength, R is the instrument spectral response and $T_o = 10,000$ K (these formulas derive

from the conventions used to calculate the quoted fluxes on the Spitzer maps). It is particularly important for the $8\mu\text{m}$ band where the emission spectra varies quickly along the bandwidth because of PAH line emission. The color correction can be up to 80% at $8\mu\text{m}$, while it is generally less than 10% for the other bands.

3.1.1 Star formation regions

In this section, we describe the SED fits for the star formation regions SQ A, HII SE, HII SW and SQ B. We fitted all the observed SEDs as the superposition of two components. The first component is the PDR/HII region dust emission template, that helps to fit the emission from warm dust located very close to young stars. The second component is the diffuse photon heated dust emission template that fits the emission from diffuse dust near star formation regions. This diffuse dust is heated by a combination of UV photons escaping from the PDR/HII region and any ambient large scale UV/optical radiation field pervading the region. We performed the fit varying four free parameters: the amplitude of the HII region/PDR SED template (determined by the parameter F_{24}^{HII} , the fraction of $24\mu\text{m}$ flux contributed by this component); the diffuse dust mass M_{dust} ; the strength and the color of the diffuse radiation field, determined by two parameters, χ_{isrf} and χ_{color} (see Sect. 3.2 for details). As one can notice, there are no degrees of freedom in these fits. Therefore it is not possible to estimate the goodness of the fit (in the sense of the fidelity of the model) from a chi-square test. Nonetheless we estimated the error on the best-fit dust masses and total dust luminosities from a multidimensional analysis of χ^2 near to its minimum χ_{min}^2 . The uncertainty on the dust mass is the minimum dust mass variation that gives $\Delta\chi^2 = \chi^2 - \chi_{\text{min}}^2$ values always greater than one, independently from the values of all the other parameters. The total luminosity error bar is determined by the lowest and highest values of the total luminosity in the subspace of fitting parameters determined by $\Delta\chi^2 \leq 1$.

The SED fits are shown in Fig. 3.1 (note that for HII SE and SQ B we used the $160\mu\text{m}$ fluxes within the $70\mu\text{m}$ source size to limit contamination from neighbours). Table 3.1 shows the best fit parameters, together with the estimate of the uncertainty

on the dust mass, the total infrared dust luminosity and the contribution to this total infrared luminosity from optical heating of diffuse dust by the diffuse radiation field, UV heating of diffuse dust by the diffuse radiation field and localized UV heating of dust in PDR/HII regions. The predicted radiation fields needed to account for the diffuse emission component are at least as strong as the local ISRF in the Milky Way with a strong variation in color. From the plots one can see that the $24\mu\text{m}$ emission is dominated by HII region/PDR emission, as expected, while $8\mu\text{m}$ and FIR points are generally dominated by diffuse emission. This is consistent with a picture where MIR emission is produced by regions very close to young stars whilst FIR emission and PAH emission come from dust illuminated by dilute radiation fields, as observed in galaxy disks (e.g. Bendo et al. 2008)

3.1.2 AGN galaxy NGC7319

The observed SED of the Seyfert 2 galaxy NGC7319 differs markedly from the SEDs we obtained for the other sources in SQ, for which the power emitted at $24\mu\text{m}$ is typically a factor ten or more smaller than that observed at 70 and $160\mu\text{m}$. For NGC7319 the amount of energy emitted at MIR wavelengths is comparable to the FIR luminosity. We first tried to fit the SED of this galaxy using the same HII region/PDR plus diffuse emission components as we have done previously for the star formation regions (we didn't include a component of synchrotron emission, originating from the AGN, because an extrapolation of its infrared luminosity from the radio measurements of Aoki et al. (1999) gives values which are six orders of magnitudes lower than the observed infrared luminosities). The best fit is shown in the left panel of Fig. 3.2. The fit tries to reproduce the high $24\mu\text{m}$ flux with the HII region template but, doing so, completely overestimates the $70\mu\text{m}$ flux. A second attempt has been performed substituting the HII region/PDR template with an AGN torus template (Fritz et al. 2006, see Sect. 3.2). As one can see from the right panel of Fig. 3.2, the observed data is reproduced much better in this case. Of course the limited number of data points doesn't allow any inference of the physical properties of the dusty torus nor provide precise information on the radiation field.

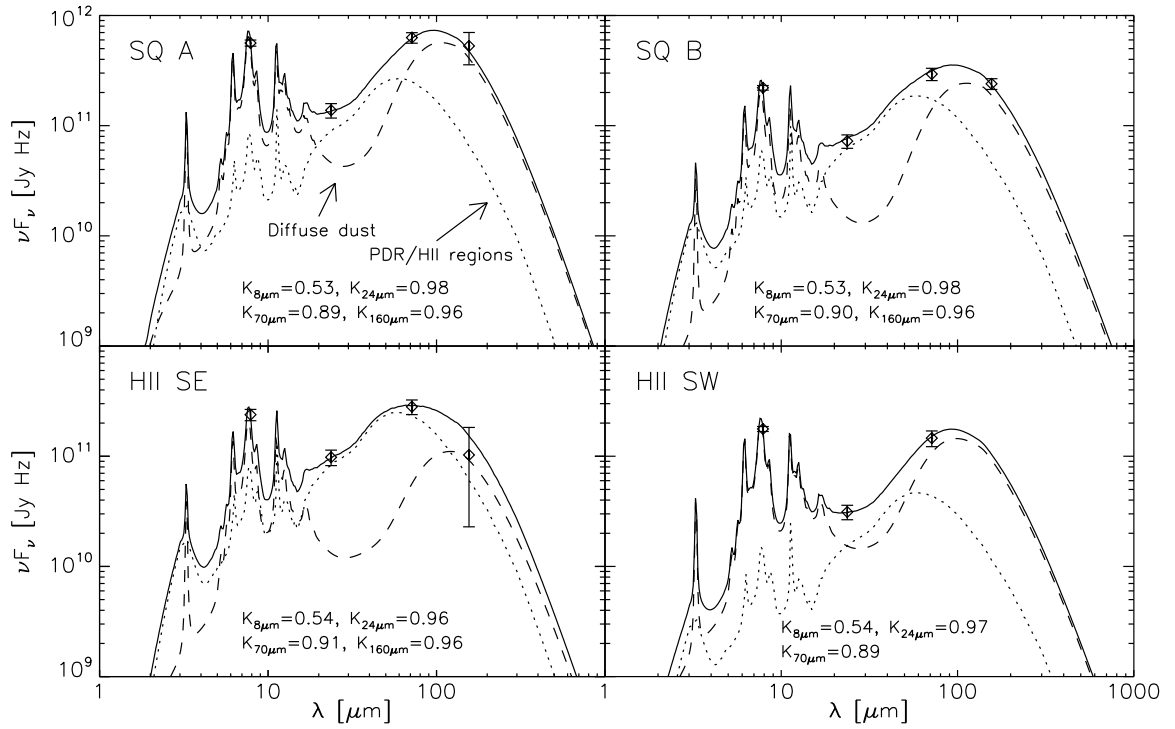


Figure 3.1: SEDs of discrete SQ star formation regions: the plotted curves are the best fit SED (solid line), the contribution from PDR/HII regions (dotted curve) and diffuse dust (dashed line). The values $K_{8\mu\text{m}}$, $K_{24\mu\text{m}}$, $K_{70\mu\text{m}}$, $K_{160\mu\text{m}}$, shown in each plot of this and the following figures, are the color corrections applied to each fitted point.

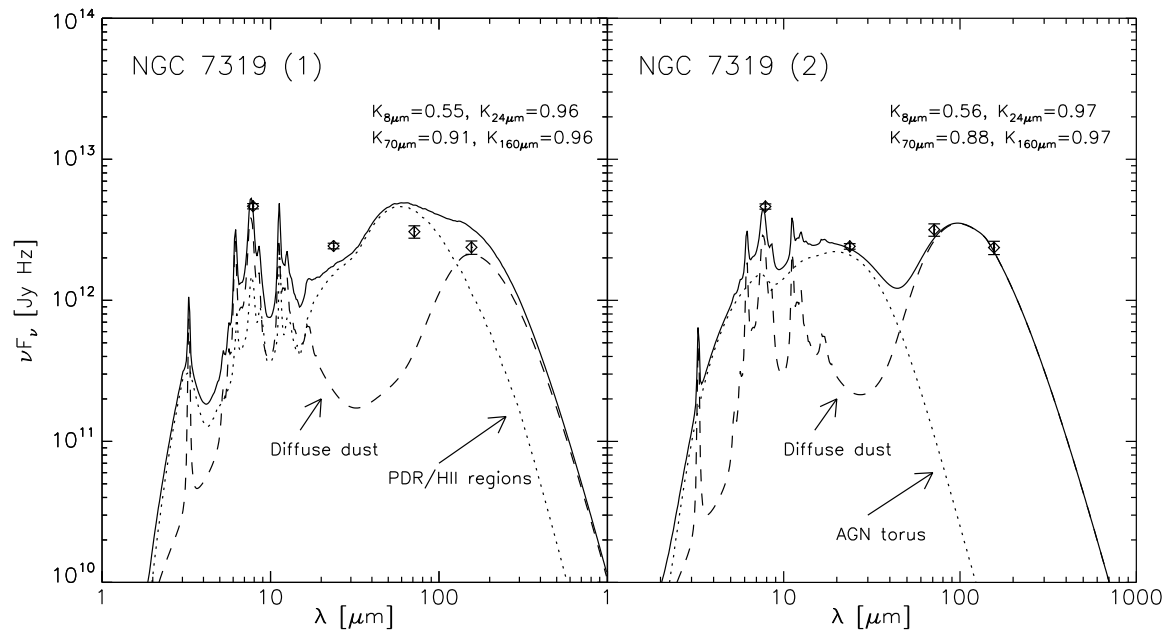


Figure 3.2: SED of NGC 7319 performed using two different combinations of templates. In the left panel, the best fit SED (solid line) is calculated using a PDR/HII region template (dotted line) and a diffuse dust component (dashed line). In the right panel the best fit is calculated using an AGN torus dust emission template (dotted) and a diffuse dust component (dashed).

However the fit does provide an indication that the majority of the $24\mu\text{m}$ emission in this galaxy is powered directly by the AGN power law radiation. The fitted parameters and the total dust luminosity derived from the AGN torus plus diffuse emission fit are shown in Table 3.1.

3.1.3 Shock region emission

The dust emission SED of the shock region contains MIR and FIR emission components which indicate inhomogeneous structure within the emitting region. As one can see from the middle panels of Fig. 2.4, the emission on the FIR residual maps shows a rough correlation with the X-ray emission, especially near the center of the shock ridge, suggesting, as mentioned before in Sect. 2.1.1, that collisional heating

of dust embedded in the hot ($T \approx 3 \times 10^6$ K) shocked plasma powers at least some of the observed emission. However the presence of significant $8\mu\text{m}$ emission rules out the possibility that the observed dust emission is purely collisionally heated because PAH molecules are not expected to survive in a medium shocked by a wave travelling at more than 125 km/s (Micelotta et al., 2010). The PAH emission must therefore either be physically unrelated to the shock, coming from another region on the line of sight, or, if associated with the shock, belong to colder gas phases embedded in the X-ray plasma. The latter scenario would be consistent with the detection of H_2 molecular line (Appleton et al. 2006, Cluver et al. 2010) and $H\alpha$ (Xu et al. 1999) emission from the shock region.

The multiphase nature of the gas in the shock region implies that there are at least four potential sources of dust emission in this region: (1) diffuse dust collisionally heated in hot plasma; (2) dust in a colder medium and heated by a diffuse radiation field; (3) HII/PDR dust emission from optically thick clouds with embedded star formation regions and (4) cold dust emission from optically thick clouds without embedded star formation.

In practice, it is not possible to distinguish model predictions for (2) and (4) over the wavelength range of the currently available data, since the only difference would correspond to a very cold emission component from the interior, self-shielded regions of the optically thick clouds, which will only become apparent at longer submm wavelengths. Therefore, we only consider explicitly here components (1) - (3), ignoring component (4). Furthermore, the four available data points are insufficient to simultaneously fit these three potential sources of dust emission, especially the diffuse photon heated and collisionally heated components which are both predicted to peak at FIR wavelengths. Therefore, we decided to perform the SED fit in two different ways corresponding to the two opposite cases, where collisional heating is either responsible for the entire FIR emission, or is completely negligible. We followed this approach in order to understand which mechanism is predominant in powering the diffuse dust emission. First, we fitted the shock region SED as a superposition of two components: the HII region/PDR template, to fit MIR emission possibly associated with star formation regions, and a collisionally heated dust SED

template (see Sect. 3.2.4). This model is appropriate for the case where photon heated diffuse FIR emission is negligible compared to the collisionally heated dust emission. Given the plasma physical properties (fixed by the X-ray emission, as described in Sect. 3.2.4), the free parameters in this fit are: the amplitude of the HII region template and the collisionally heated dust mass. We performed these fits for the highest and the lowest densities admitted by the X-ray data, however, the final results are quite similar. In the upper panels of Fig. 3.3, we show the best fit obtained for the highest considered particle density $n = 0.016 \text{ cm}^{-3}$ and temperature $T = 3 \times 10^6 \text{ K}$. As one can see, the collisionally heated component (dashed curve) is sufficient to reproduce the observed data except the $8\mu\text{m}$ datum which, as already remarked, is too high to be due to PDR/HII regions, requiring a diffuse photon-heated contribution. The model curve shown (fitted, in this case, just to the three longer wavelength data points) was calculated assuming a power law grain size distribution with exponent $k = 2.5$, the expected value in the case of equilibrium between dust injection (with a standard $k = 3.5$ interstellar distribution; Mathis et al. 1977) and sputtering of grains in hot plasmas (Dwek et al. 1990). The dust mass required to produce the observed FIR flux densities, for the case where collisional heating rather than diffuse photon heating is considered, is $2 \times 10^7 M_{\odot}$.

The second fit was performed using the HII region/PDR template and the photon-heated diffuse dust component. This combination of SED templates represents the case where the entire emission is powered by photons and collisional heating is negligible. Using this combination of SEDs, one can fit all the data points, including the $8\mu\text{m}$ flux. The best-fit curve is shown in the lower panels of Fig. 3.3. In this fit, the diffuse dust component dominates the emission in all the Spitzer bands, even at $24\mu\text{m}$, where the contribution of PDR/HII regions is normally predominant. The fitted parameters are given in Table 3.1. We note that the diffuse radiation fields needed for the fit are colder than those needed to fit the star formation regions in Sect. 3.1.1.

In conclusion, the FIR part of the SED from the shock can be fitted by a cold continuum component either from collisional heating, which is cold due to the limited ambient density of plasma particles and the underabundance of small stochastically

heated grains, or from photon heating, which is cold due to the low ambient density of photons coupled with a low UV to optical ratio. The only real discriminant favouring photon heating would be the $8\mu\text{m}$ emission which, as a PAH tracer, cannot be explained by collisional heating.

Contamination of the $8\mu\text{m}$ band flux by H_2 molecular line emission

Appleton et al. (2006) and Cluver et al. (2010) showed that the shock region of SQ emits an unusual flux, given the level of observed star formation, in the form of H_2 infrared rotational line emission. This H_2 line emission could also contribute to the cooling of the gas, but a complete explanation of the way the emission is powered is still proving elusive (see Guillard et al. 2009). From our perspective, the infrared lines can be a potential source of contamination of the observed $8\mu\text{m}$ flux. Since, as we saw above, the $8\mu\text{m}$ flux gives a strong constraint on the dust heating mechanism powering the observed infrared flux, it is important to quantify this contamination. Specifically the H_2 infrared lines falling within the Spitzer $8\mu\text{m}$ band are $H_2 0 - 0S(4)$ and $H_2 0 - 0S(5)$. The total power of these lines in an area of 2307 arcs^2 is $1.66 \times 10^{-16} \text{ W/m}^2$ (Table 2 of Cluver et al. 2010, “Main Shock” region). Scaling this value to our integration area ($1600''$), we obtain a total line emission power, $P_{H_2}^{8\mu\text{m}} = 1.15 \times 10^{-16} \text{ W/m}^2$. The total power (line plus continuum) received within the IRAC $8\mu\text{m}$ band is equal to $P_{\text{tot}}^{8\mu\text{m}} = \int_{\nu_1}^{\nu_2} f_\nu d\nu$, where f_ν is the received signal and $\nu_1 = 3.1 \times 10^{13} \text{ Hz}$ and $\nu_2 = 4.7 \times 10^{13} \text{ Hz}$ are, respectively, the frequencies below and above which the band response efficiency is less than 10% of the maximum. Using the IRAC convention to calculate the quoted fluxes, the received signal can be written as $f_\nu = f_\nu^{8\mu\text{m}} \nu^{8\mu\text{m}} / \nu$ where $f_\nu^{8\mu\text{m}} = 8.1 \text{ mJy}$ is the $8\mu\text{m}$ flux density we measured for the shock region and $\nu^{8\mu\text{m}} = 3.8 \times 10^{13} \text{ Hz}$. The result of the integration gives $P_{\text{tot}}^{8\mu\text{m}} = 1.2 \times 10^{15} \text{ W/m}^2$, which is a factor of ten higher than $P_{H_2}^{8\mu\text{m}}$. Since the contamination is small, we didn’t apply a correction to the measured $8\mu\text{m}$ flux for the shock region.

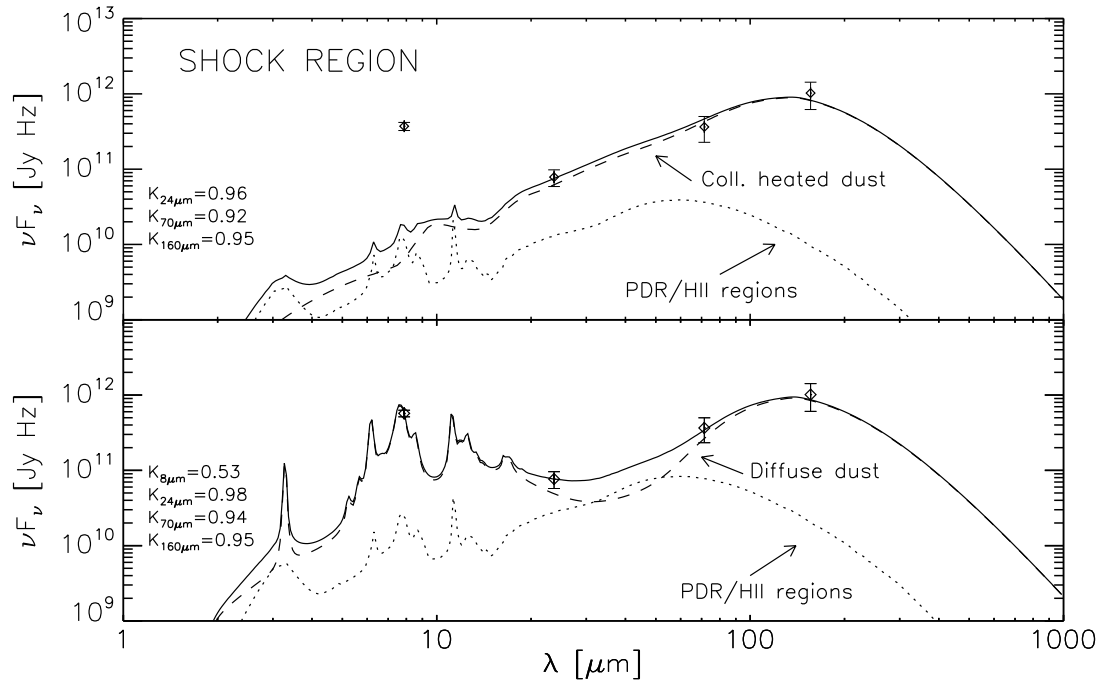


Figure 3.3: SED of the shock region. The upper panel shows the fit performed using an PDR/HII region template plus a collisional heating component. The hot gas parameters adopted to calculate the collisionally heated dust SED are: $n = 0.016 \text{ cm}^{-3}$ and $T = 3 \times 10^6 \text{ K}$. The lower panel shows the fit performed using the PDR/HII region template and a uniformly photon-heated dust model.

3.1.4 Extended emission

In a completely analogous way as for the shock region emission, we tried to model the observed extended emission SED by including a collisionally heated dust emission component. This is motivated by the fact that the FIR residual maps show the presence of extended emission in the area of the main part of the X-ray halo emission (the so called “HALO” in Trinchieri et al. 2005). In the upper panels of Fig. 3.4 we show the SED fit performed adding two components: HII regions plus collisionally heated dust emission. In this fit the adopted plasma physical parameters, derived in Sect. 3.2.4, are $n = 0.001 \text{ cm}^{-3}$ and $T = 6 \times 10^6 \text{ K}$ and we again assumed $k = 2.5$. Using this combination of SEDs, one can roughly reproduce the SED longward of $24\mu\text{m}$, but the collisionally heated component dominates only the $160\mu\text{m}$ flux. The dust mass inferred from this fit (constrained, as in the case for the model fit to the shock SED incorporating collisional heating, only by the three longer wavelength points) is $1.0 \times 10^8 M_{\odot}$.

In the lower panel of Fig. 3.4, we show the fit performed adding HII region and diffuse photon heated emission. As before for the shock region, using these two components one can fit the entire spectra including the $8\mu\text{m}$ point. In this fit HII region emission dominates at 24 and $70\mu\text{m}$ while the diffuse emission is responsible for the 8 and $160\mu\text{m}$ fluxes. The fitted parameters are shown in Table 3.1. As for the shock emission, we note that the extended emission component requires a very cold FIR component from the fit even though, observationally speaking, this is a somewhat less robust conclusion since it really needs to be confirmed with longer wavelength photometry.

3.1.5 Foreground galaxy NGC7320

For the SED fit of the foreground galaxy NGC7320, we used again the usual combination of PDR/HII regions plus diffuse photon heated dust emission components. The best fit is shown in the left panel of Fig. 3.5. The relative contribution of HII regions to the $24\mu\text{m}$ flux is reduced compared to the star formation regions, whose SED fits have been shown before. This might be physically understandable since,

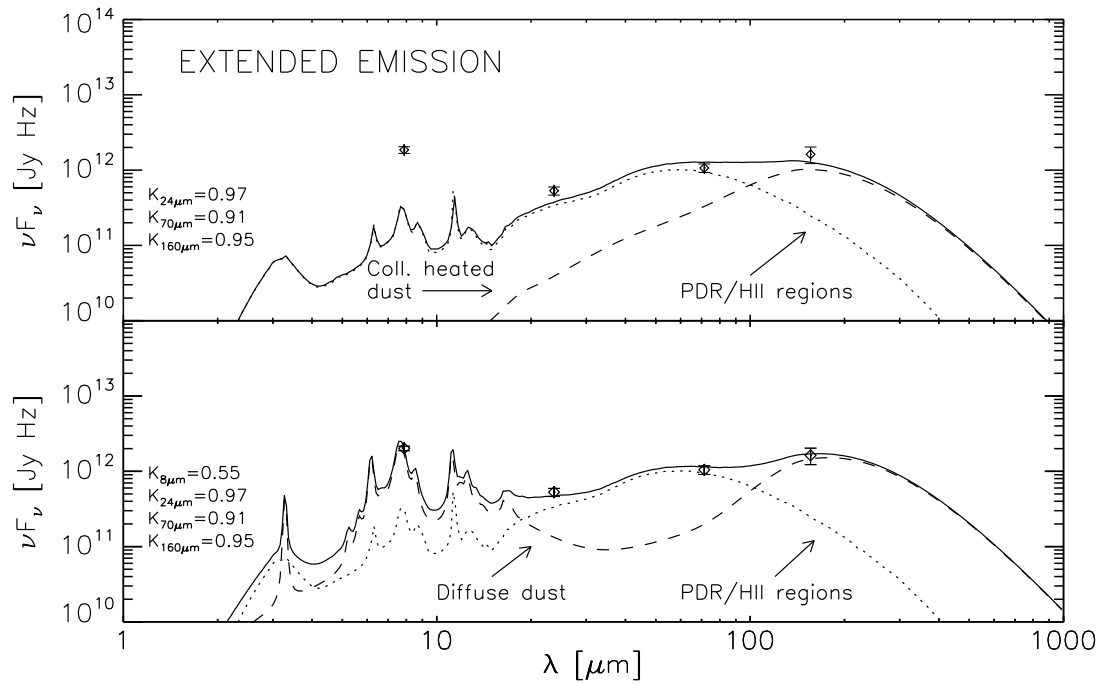


Figure 3.4: SED of the extended emission. The upper panel shows the fit performed using a PDR/HII region template plus a collisional heating component. The hot gas parameters adopted to calculate the collisionally heated dust SED are: $n = 0.001 \text{ cm}^{-3}$ and $T = 6 \times 10^6 \text{ K}$. The lower panel shows the fit performed using the HII region template and a uniformly photon-heated dust model.

in this case, we are fitting the emission of a galaxy as a whole, including all the diffuse interstellar medium containing small dust particles whose stochastically heated emission can account for a major part of the total MIR emission (e.g. Popescu et al. 2000).

3.1.6 Infrared source north of NGC7319 (HII–N)

We attempted to fit the observed emission for this source with a combination of PDR/HII regions plus diffuse photon–heated dust emission. However, this source shows a very peculiar MIR to FIR ratio and, as a consequence, we have not managed to fit the entire spectra. As shown in the right panel of Fig. 3.5, the FIR points are highly underestimated by the best fit curve. If no systematic errors are present in our measurements, it might be that this source is a distant background source and its intrinsic colors are heavily redshifted. The high resolution HST maps of SQ (see Fig. 3.6) show at the position of HII N a rather red galaxy, whose spiral structure is barely visible. The red optical color of this galaxy is consistent with it being a possible background source. The real nature of this source can be determined by measuring the redshift directly from a spectra of this source and/or by searching at longer wavelengths for a counterpart whose dust emission SED peaks deep in the submillimeter regime.

3.2 Dust SED templates and models

As it has been shown in the previous section, in order to fit the observed source SEDs, we needed to model the dust emission from several environments: dust in PDR/HII regions, dust heated by diffuse radiation fields, dust in AGN tori and collisionally heated dust embedded in hot plasmas. In this section, we describe the characteristics of the SEDs we used to model the emission from each of these regions.

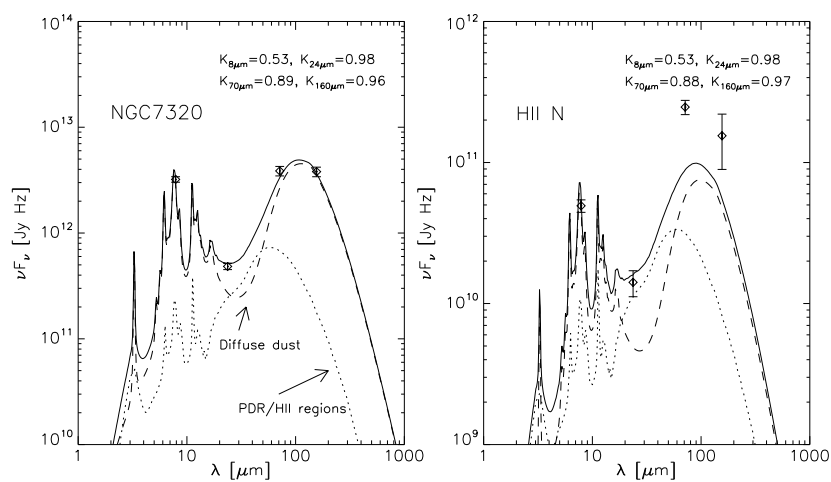


Figure 3.5: SED of NGC7320 and HII N: the plotted curves are the best fit SED (solid line), the contribution from PDR/HII regions (dotted curve) and diffuse dust (dashed line).

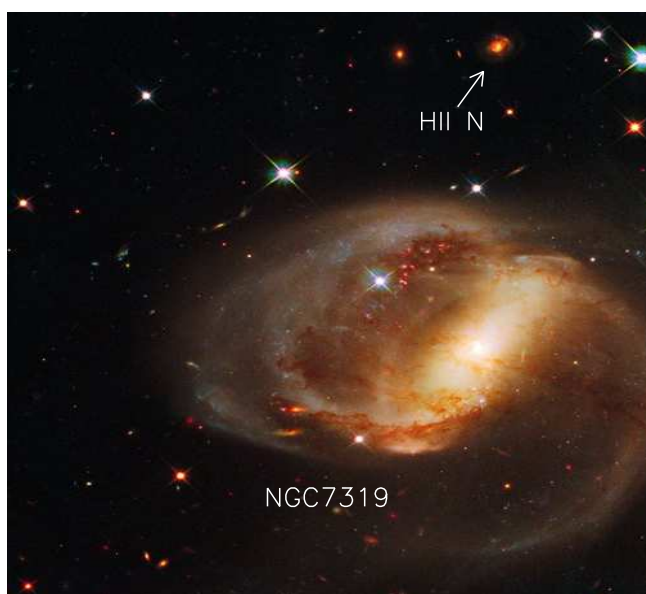


Figure 3.6: Extraction from HST high resolution color map of SQ showing the optical counterpart of the infrared source HII N.

Source	M_{dust} ($10^7 M_{\odot}$)	χ_{isrf}	χ_{color}	F_{24}	$L_{\text{UV}}^{\text{abs,local}}$ ($10^{43} \frac{\text{erg}}{\text{s}}$)	$L_{\text{opt}}^{\text{abs,diffuse}}$ ($10^{43} \frac{\text{erg}}{\text{s}}$)	$L_{\text{UV}}^{\text{abs,diffuse}}$ ($10^{43} \frac{\text{erg}}{\text{s}}$)	L_{tot} ($10^{43} \frac{\text{erg}}{\text{s}}$)
SQ A	$0.6^{+0.1}_{-0.2}$	2	2	0.65 (HII)	0.45	0.61	0.36	$1.4^{+0.2}_{-0.1}$
HII SE 7318b	$0.22^{+0.04}_{-0.05}$	2	0.25	0.86(HII)	0.42	0.10	0.12	$0.64^{+0.06}_{-0.06}$
HII SW 7318b	$0.11^{+0.01}_{-0.01}$	4	1	0.50 (HII)	0.08	0.14	0.12	$0.34^{+0.03}_{-0.01}$
SQ B	$0.37^{+0.09}_{-0.04}$	1	4	0.80 (HII)	0.31	0.28	0.10	$0.70^{+0.02}_{-0.03}$
NGC7319	$2.7^{+0.4}_{-0.4}$	2	4	0.90 (AGN)	4.13	4.01	1.47	$9.6^{+0.3}_{-0.3}$
NGC7320	$0.08^{+0.02}_{-0.01}$	1	4	0.45 (HII)	0.014	0.059	0.021	$0.094^{+0.005}_{-0.002}$
shock region	$4.4^{+0.5}_{-1}$	0.3	4	0.35 (HII)	0.14	1.00	0.37	$1.5^{+0.1}_{-0.3}$
Extended emission	47^{+3}_{-4}	0.1	1	0.71(HII)	1.71	1.56	1.30	$4.6^{+0.2}_{-0.5}$

Table 3.1: Results from the infrared SED fitting. Col1: Fitted source; col2: Cold component dust mass; col3-4: Radiation field χ_{isrf} and χ_{color} parameters (see Sect. 3.2); col5: Fraction of $24\mu\text{m}$ flux contributed by HII regions or AGN torus templates; col6: Luminosity of dust in PDR/HII regions or in AGN torus in the case of NGC7319; col7: Luminosity of diffuse dust powered by the absorption of optical photons of the diffuse radiation field; col8: Luminosity of diffuse dust powered by the absorption of UV photons of the diffuse radiation field; col9: Total dust luminosity.

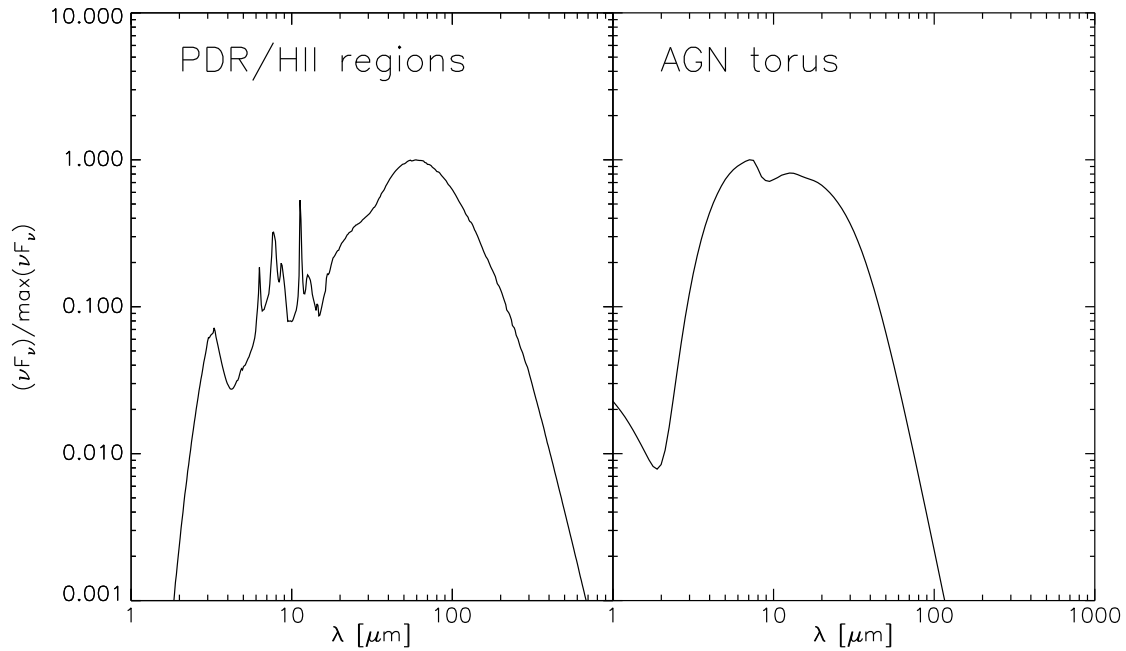


Figure 3.7: PDR/HII region dust emission template (left panel) and AGN torus dust emission template (right panel)

3.2.1 Dust in PDR/HII regions

Dust in HII regions and photodissociation regions (PDR), close to young stars, is warm and emits predominantly in the MIR. To model its emission, we used an SED template derived by the fitting of Milky Way star formation region infrared emission with the theoretical model of Groves et al. (2008). The Galactic star formation regions considered are the radio-selected sample of Conti et al. (2004). The template is the average fitted spectra of the observed emission from these regions and it is shown in the left panel of Fig. 3.7. Further details can be found in Popescu & Tuffs 2010.

3.2.2 Dust heated by diffuse radiation fields

To fit the diffuse dust emission, we created a grid of theoretical SEDs of emission from dust heated by a uniform radiation field. The code we used to calculate dust

emission, developed by Joerg Fischera (details will be given in Fischera et al. (2010), in preparation), assumes a dust composition including graphite, silicates, iron and PAH molecules. The abundances and size distributions are the same as in Table 2 of Fischera et al. (2008). Dust emission is calculated taking into account the stochastic temperature fluctuations of dust grains following the numerical method described by Guhathakurta et al. (1989), combined with the step-wise analytical solution of Voit (2005). We created the set of SEDs by varying the intensity and the color of the radiation field heating the dust and keeping the dust composition fixed. The standard shape of the radiation field spectra, adopted by the dust emission code, is that derived by Mathis et al. (1983) to model the local Galactic ISRF. In this spectrum, the stellar contribution consists of four components: a UV emission from early type stars plus three blackbody curves at temperatures $T_2 = 7500$ K, $T_3 = 4000$ K and $T_4 = 3000$ K used to reproduce, respectively, the emission from young/old disk stars and Red Giants. Each blackbody curve is multiplied by a dilution factor W_i that defines its intensity. The whole spectrum is multiplied by a parameter, χ_{isrf} , whose value is unity when the spectrum intensity is the same as in the local radiation field. In order to consider different colors of the radiation field, we defined a second parameter, χ_{color} , that multiplies only the blackbody curves used to model the old disk population and the Red Giant emission (blackbody temperatures T_3 and T_4). For a range of values of χ_{isrf} (0.1,0.3,0.5,1,2,4) and χ_{color} (0.25,0.5,1,2,4), we calculated the corresponding dust emission and created the set of models for the SED fit. The result of increasing the χ_{isrf} value is that the overall intensity of the radiation field is higher and, therefore, the equilibrium dust temperature is higher, leading to a warmer emission in the FIR (see left panel of Fig. 3.8). A value of χ_{color} higher than unity increases the relative contribution of the cold stellar emission, which peaks in the optical range. These wavelengths are more efficiently absorbed by big grains than by PAH molecules (and small grains). As a consequence, by varying this parameter, one modifies the ratio between the peak intensity in the FIR, produced by big grains and the peak intensity at $8\mu\text{m}$, due to PAH molecules which are mainly heated by UV photons (see right panel of Fig. 3.8). A similar effect would have also been produced by varying the relative abundance of PAH

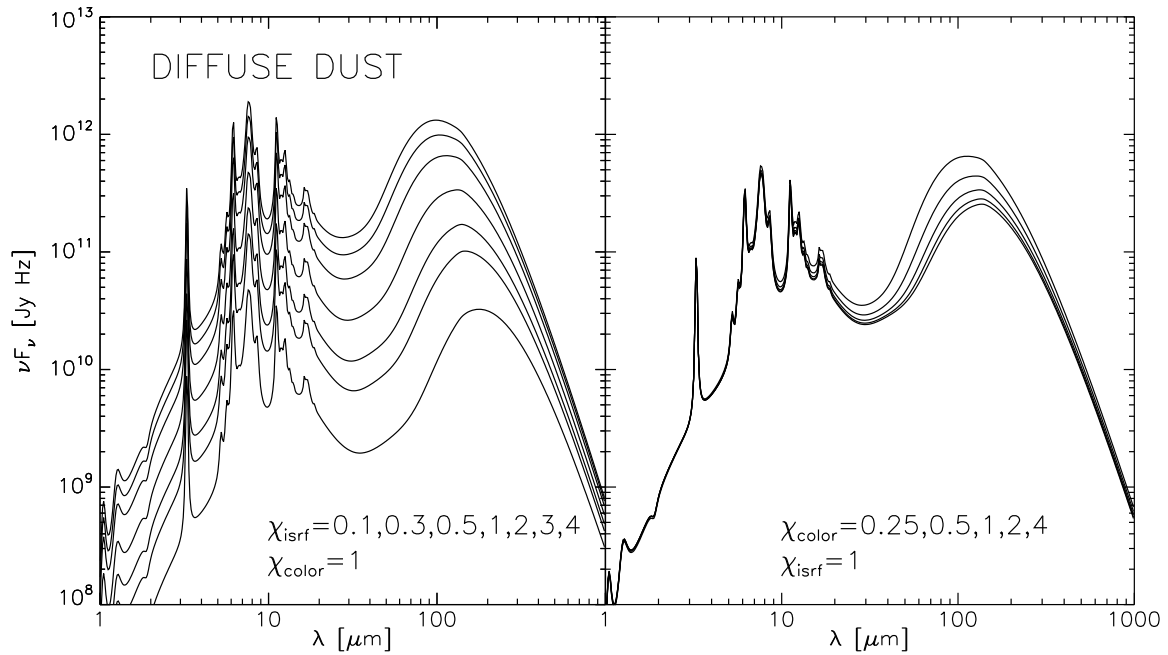


Figure 3.8: Diffuse photon heated dust SEDs for different choices of χ_{isrf} and χ_{color} . In the left panel the SEDs are calculated assuming $\chi_{\text{color}} = 1$ and several values of χ_{isrf} (the higher curves correspond to higher values of χ_{isrf}). In the right panel we assumed $\chi_{\text{isrf}} = 1$ and different values of χ_{color} (similarly, the higher curves correspond to higher values of χ_{color}). The SEDs are calculated assuming a distance equal to 94 Mpc (SQ distance) and a dust mass $M_d = 10^7 M_\odot$.

molecules and solid grains.

3.2.3 Dust emission from AGN torus

We selected a theoretical dusty torus SED between those created by Feltre et al. (2010), in preparation, using the model presented by Fritz et al. (2006). In this model, the characteristic of the torus, supposed to be homogeneous, are defined by several parameters (see Fig. 3.9): opening angle, external to internal radius ratio, the equatorial optical depth at $9.7\mu\text{m}$ ($\tau(9.7\mu\text{m})$) and two parameters, β and γ , which determine the radial and the angular density profile respectively according to the

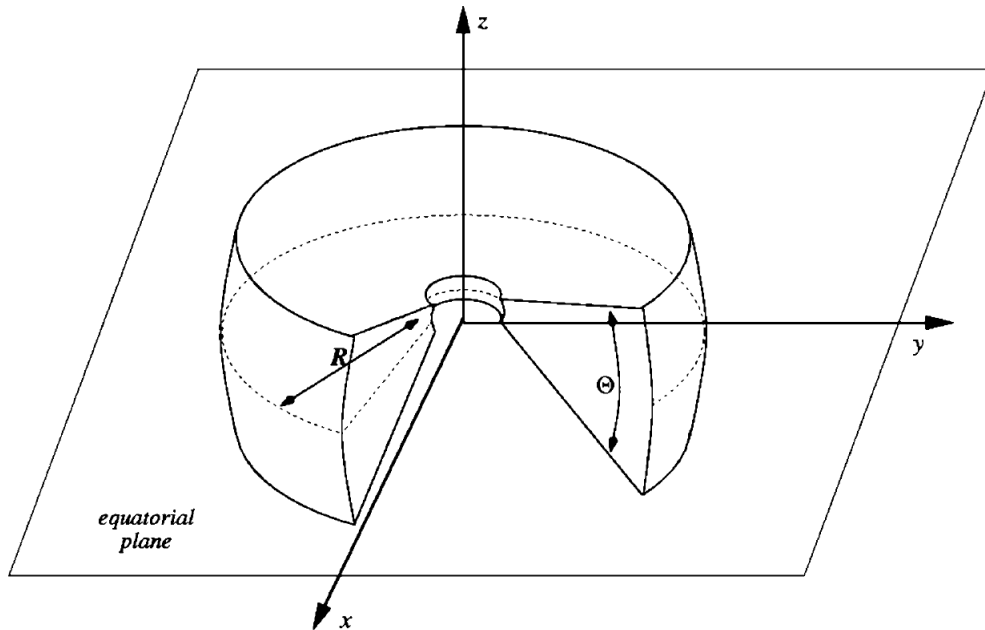


Figure 3.9: AGN torus model from Fritz et al. (2006)

formula $\rho(r, \theta) = \alpha r^{-\beta} e^{-\gamma |\cos(\theta)|}$, where r is the radial coordinate and θ is the angle between a volume element and the equatorial plane (note that α is determined by the torus optical depth). We selected a model with a large opening angle (140°), with an angular gradient in the density profile ($\beta = 0$, $\gamma = 6$), external to internal radius ratio equal to 30 and equatorial optical depth $\tau(9.7\mu\text{m}) = 6$. The chosen parameters are well within the range of values found by Fritz et al. (2006) from the fitting of a sample of Seyfert2 galaxies. We then extracted the output SED in the equatorial view, according to the Seyfert 2 classification of NGC 7319, which is the AGN galaxy in SQ. The extracted SED is the template we used for fitting the AGN torus emission and it is shown in the right panel of Fig. 3.7.

3.2.4 Dust heated by collisions in X-ray plasmas

Finally, we needed to model the emission from collisionally heated dust. For this, we used a code, created by J.Fischera, based on the works by Guhathakurta et al. (1989) and Voit (2005) for calculating the stochastic heating and using the results

of Draine et al. (1979) and Dwek (1987) to determine the heating rates due to collisional heating. Dust composition is assumed to be a mix of graphite (47%) and silicates (53%). PAH molecules are not included but since they have an extremely small destruction time scale when embedded in hot plasmas with $T > 10^6$ K, their abundance is expected to be negligible. In order to perform the calculations, one needs to specify the physical properties of the plasma, i.e. the density, temperature and metallicity. The exact value of metallicity is not important because dust is predominantly heated by collisions with electrons, provided mainly by ionized hydrogen and helium. Plasma temperature and density are derived from the X-ray data (see below). An important phenomena that should be taken into account while preparing the SED models is dust destruction due to sputtering (Draine et al. 1979). Because the efficiency of sputtering depends on the grain size, we expect that the size distribution of grains in hot plasmas is different from that of dust in the cold ISM, typically assumed to be $n(a) \propto a^{-k}$ with $k = 3.5$ (Mathis et al. 1977). Therefore, we created a set of SEDs varying: 1) the plasma's physical parameters (see Table 3.2), and 2) the exponent, k , of the size distribution in the range $[1, 3.5]$. A k value lower than 3.5 implies that the relative number of big grains is higher compared to the standard size distribution. Since the destruction time scale due to dust sputtering is directly proportional to the grain size (Draine et al. 1979), a higher relative abundance of big grains is indeed expected in hot plasmas. Once the heating rates due to collisions are fixed, a change in k modifies the color of the emitted radiation (see Fig. 3.10). This happens because big grains are generally colder than small grains, and do not provide warm dust emission due to stochastic heating. Therefore, changing their relative abundance, one can obtain colder or warmer SEDs.

X-ray plasma temperature and density in SQ Shock and Halo regions

As we mentioned before, the hot plasma physical parameters, needed for the calculation of the emission SED from collisionally heated dust, in both the shock and halo gas, are derived from the X-ray emission. The temperatures characteristic of the plasma have been obtained by Trinchieri et al. (2005) fitting XMM-NETWON X-ray data and quoted in their Table 3. They fitted the source X-ray spectra with

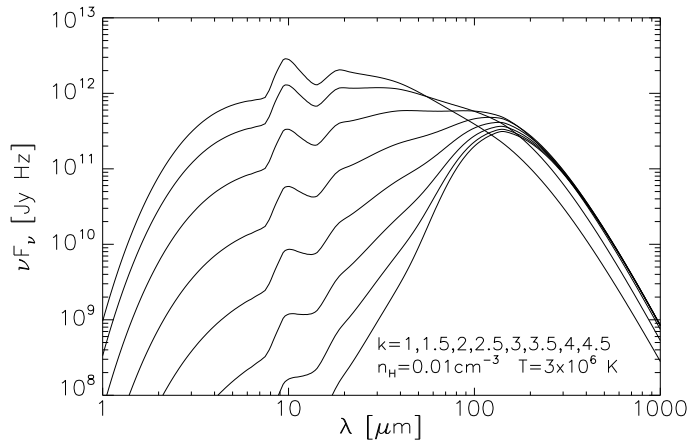


Figure 3.10: Theoretical collisionally heated dust SEDs for several values of the size distribution exponent k . From the lowest to the highest curve the k values are respectively 1, 1.5, 2, 2.5, 3, 3.5, 4, 4.5. The SEDs are calculated assuming for the plasma density and temperature $n_H = 0.01 \text{ cm}^{-3}$ and $T = 3 \times 10^6 \text{ K}$ respectively, a dust mass $M_d = 10^7 M_\odot$ and a distance equal to 94 Mpc.

two temperature plasma models. The fitted colder component is predominant for the shock region and has a temperature $T \approx 3 \times 10^6 \text{ K}$ that we assumed to calculate the dust emission. For the halo region, the two plasma components have similar luminosities. In this case, we assumed the average value $T = 6 \times 10^6 \text{ K}$ for the dust emission calculation (the fitted temperatures are $T_1 = 3.5 \times 10^6 \text{ K}$ and $T_2 = 8.8 \times 10^6 \text{ K}$). The plasma densities have been derived from the X-ray luminosity, which can be expressed as:

$$L = n_t n_e \Lambda(T) V, \quad (3.4)$$

where n_t and n_e are the ion and the electron number densities respectively, $\Lambda(T)$ is the cooling function and V is the volume of the X-ray emitting plasma. From given L , $\Lambda(T)$ and V , one can calculate the gas density $n = (n_t n_e)^{0.5}$ by inverting eq.3.4. Given the plasma temperatures found by Trinchieri et al. (2005), we derived $\Lambda(T)$ by interpolating the CIE curve calculated by Sutherland et al. (1993) at two different metallicities corresponding to 100% and 30% the solar metallicity. Then we assumed for the shock gas an emitting volume equal to the projected shock

Source	Z (Z_{\odot})	Ω ($10^{-23} \frac{\text{erg cm}^3}{\text{s}}$)	los/R (kpc)	n (cm^{-3})	M_{gas} ($10^9 M_{\odot}$)
SHOCK	1	3.82	5	0.012	0.65
SHOCK	1	3.82	10	0.009	0.92
SHOCK	1	3.82	20	0.006	1.30
SHOCK	1	3.82	40	0.004	1.84
SHOCK	0.3	1.92	5	0.018	0.92
SHOCK	0.3	1.92	10	0.012	1.30
SHOCK	0.3	1.92	20	0.009	1.83
SHOCK	0.3	1.92	40	0.006	2.60
HALO	1	2.54	40	0.0011	10.4
HALO	0.3	1.39	40	0.0016	14.4

Table 3.2: X-ray gas parameters for the shock and halo components assuming different gas metallicity or emission volumes. Col1: Source; col2: assumed metallicity; col3: cooling rate; col4: line of sight depth (for the shock), or sphere radius (for the halo); col5: gas number density defined as $n = (n_i n_e)^{1/2}$; col6: gas mass.

ridge area ($A = 330 \text{ kpc}^2$) multiplied by a parametrized line of sight depth, l , and for the halo, we adopted an emitting sphere of radius 40 kpc corresponding to $90''$ at 94 Mpc distance. The luminosity values we used are those inferred by Trinchieri et al. (2005) ($L_X^{shock} \approx 2.4 \times 10^{41} \text{ erg/s}$ and $L_X^{halo} \approx 2.3 \times 10^{41} \text{ erg/s}$), properly scaled to the different assumed distance (85 Mpc in Trinchieri et al. 2005 vs 94 Mpc here). The results for different choices of emitting volumes and metallicity are shown in Table 3.2. For the shock region plasma we obtained densities in the range $4 - 18 \times 10^{-3} \text{ cm}^{-3}$. As expected, the minimum density is obtained for higher metallicity (that is higher Λ) and largest volume, while the maximum density corresponds to lower metallicity (lower Λ) and smallest volume. For the halo gas, the inferred densities are 1.1×10^{-4} and $1.6 \times 10^{-4} \text{ cm}^{-3}$ for $Z = Z_{\odot}$ and $Z = 0.3 Z_{\odot}$ respectively.

Chapter 4

Star formation and AGN dust emission in SQ

4.1 Introduction

If one were to view SQ at a greater distance such that the group would appear as a point-like source to Spitzer (i.e. at a redshift of $\gtrsim 0.5 - 2$, in the main star-forming epoch of the Universe, and also the epoch when galaxy groups were first forming), one would not regard this as a particularly unusual infrared source. On the basis of the shape of the total dust emission SED, plotted as the black curve in Fig. 4.1, the only noteworthy points would be the quite warm MIR colours and moderately high FIR luminosities which would most likely lead our hypothetical observer to conclude that this source had an AGN, possibly combined with a mild starburst. In this he would be at least in part correct, as illustrated in Fig. 4.1 by the curves representing the constituent emission components from the AGN galaxy (red), from star formation regions (blue) and the emission from X-ray emitting regions (green), where one can immediately see the high relative contributions of the AGN galaxy to the $8\mu\text{m}$ and $24\mu\text{m}$ emission, respectively $\sim 50\%$ and $\sim 70\%$. In the FIR, although the AGN galaxy is still the most luminous individual source, there is emission at a comparable level from the combination of the distributed star-formation regions in SQ and the infrared counterparts of the X-ray emitting shock and halo structures;

the combined FIR/submm SED resembles that of star-forming galaxies, with an amplitude similar to that of the local starburst galaxy M82. However our analysis of the spatially resolved structures has shown that the characteristics of infrared emission in SQ are the very opposite of a nuclear starburst, with the star-formation activity enhanced in regions far away from the main bodies of the galaxies.

In the following Sect.4.2 and 4.3 we quantify the star formation rates in the several regions of SQ, together with the related gas masses, and we discuss to what extent the nature of the distributed star formation in SQ may differ from the star formation in the disks of individual galaxies, in terms of sources of gas and the star formation efficiency for the group as a whole. In Sect.4.4 we discuss the nature of the infrared emission from NGC7319, the only galaxy of the group showing FIR emission enhanced towards the galaxy central regions, and the role of its AGN in powering such emission. In the next chapter we'll discuss to which extent collisional heating of grains in the IGM of SQ may be cooling the IGM and thus contributing to the fuelling of the observed star formation.

4.2 Quantifying star formation rates and gas masses in SQ

4.2.1 Star formation rates

The measurements of UV, recombination line and dust emission from sources in SQ can in principle be used to derive star formation rates (SFR), provided proper account is taken of the absorption of the UV/optical photons by dust and subsequent re-emission in the MIR/FIR spectral regimes. Several authors have provided empirically-based relations achieving this for spiral galaxies on scales of kpc. Calzetti et al. (2007) presented an $H\alpha$ luminosity based star formation rate relation: $SFR(M_{\odot}\text{yr}^{-1}) = 5.3 \times 10^{-42} [L(H\alpha)_{\text{obs}} + (0.031 \pm 0.006)L(24\mu\text{m})]$. In this relation the $24\mu\text{m}$ luminosity is used to estimate the $H\alpha$ luminosity obscured by dust. Bigiel et al. (2008) combined GALEX FUV and Spitzer $24\mu\text{m}$ fluxes to obtain SFR per unit area maps of a sample of spiral galaxies. Similarly to Calzetti et al. (2007), they

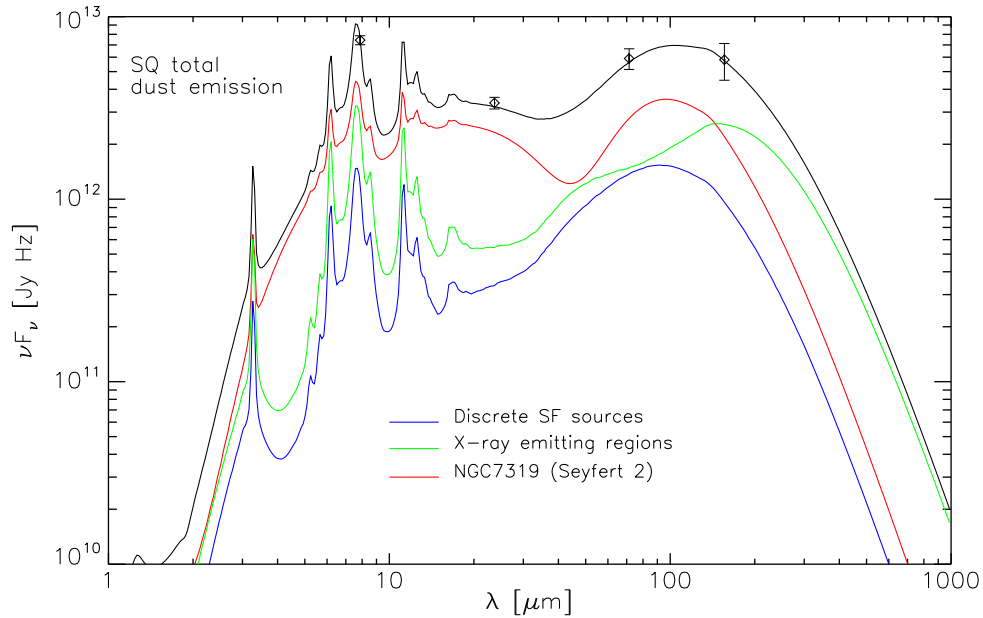


Figure 4.1: SED of the total SQ dust emission. The plotted points are the sum of the fluxes of all the dust emitting sources in SQ: the discrete sources SQ-A, HII-SE, HII-SW, SQ-B, the AGN galaxy NGC7319, the shock region and the extended emission (the applied color corrections are: 0.62 ($8\mu\text{m}$), 0.97 ($24\mu\text{m}$), 0.90 ($70\mu\text{m}$) and 0.97 ($160\mu\text{m}$)). The plotted curves are the total emission SED (black), the discrete star formation region total SED (blue), the AGN galaxy NGC7319 SED (red) and the X-ray emitting region total SED (green). All the SEDs representing the total emission from more sources are derived summing the fitted SEDs as described in Sect.3.1. In the case of the X-ray emitting region SED, we combined the SED fits for the shock region and the extended emission performed using purely photon-heated dust emission components (see Sect.3.1.3 and 3.1.4).

used a UV SFR calibration and they used the $24\mu\text{m}$ flux to measure the obscured UV flux.

Simple application of the Calzetti relation to SQ is hampered by the lack of pure measurement of $H\alpha$ emission driven by star formation. As one can see from Figs. 5 from Sulentic et al. (2001) (reproduced in Fig. 1.8 of this thesis), the shock region $H\alpha$ emission shows a diffuse component that reflects the north–south ridge seen in the soft X-ray regime. This diffuse $H\alpha$ emission cannot be considered for SFR measurements because, as demonstrated by Xu et al. (2003) from spectral line analysis, the $H\alpha$ emission in the shock region is dominated by shock–excitation rather than star formation. In addition, it is not clear that the semi–empirical relations derived for spiral galaxies should apply to the sources in SQ.

Therefore, we adopted a new approach, using only observational indicators of star formation activity available for all sources in SQ, and utilizing the results of the fits to the dust emission SEDs given in Sect. 3.1. Our method to estimate SFRs is based on a UV–SFR calibration. Specifically we adopted the calibration by Salim et al. (2007):

$$SFR_{\text{UV}} = 1.08 \times 10^{-28} F_{\text{UV}} \text{ M}_{\odot}/\text{yr} \quad (4.1)$$

where F_{UV} is the FUV luminosity density in units of erg/s/Hz which would be observed in the GALEX FUV band in the absence of dust. F_{UV} can be written as:

$$F_{\text{UV}} = F_{\text{UV}}^{\text{direct}} + F_{\text{UV}}^{\text{abs,local}} + F_{\text{UV}}^{\text{abs,diffuse}} \quad (4.2)$$

where $F_{\text{UV}}^{\text{direct}}$ is the directly observed unabsorbed component of FUV luminosity density, $F_{\text{UV}}^{\text{abs,local}}$ is the FUV luminosity density locally absorbed by dust in star formation regions and $F_{\text{UV}}^{\text{abs,diffuse}}$ is the FUV luminosity density absorbed by dust in the diffuse medium surrounding the star formation regions.

We measured $F_{\text{UV}}^{\text{direct}}$ for each source by performing aperture photometry on the GALEX FUV map in a completely analogous way to the photometry we performed on the Spitzer MIR maps, including the construction of the curve of growth after masking the galaxies NGC7319 and NGC7320 and the star formation regions (see Fig. 2.9). The final flux densities, shown in col. 4 of Table 4.1, include the correction for Galactic foreground extinction ($E(B - V) = 0.079$, Schlegel et al. 1998;

$A(FUV) = 8.24 * E(B - V)$, Wyder et al. 2007). Values for the obscured emission components $F_{UV}^{\text{abs,local}}$ and $F_{UV}^{\text{abs,diffuse}}$ were extracted from the fits to the dust emission SEDs by noting that the total infrared luminosity emitted by dust and powered by UV photons can be written as:

$$L_{\text{dust,UV}} = L_{UV}^{\text{abs,local}} + L_{UV}^{\text{abs,diffuse}} \quad (4.3)$$

where $L_{UV}^{\text{abs,local}}$ is the luminosity of dust emission in star formation regions, dominated by UV photon heating, and $L_{UV}^{\text{abs,diffuse}}$ is the part of the diffuse dust luminosity powered by UV photons, respectively tabulated in cols. 6 and 8 of Table 3.1. Since the intrinsic SEDs of the young stellar population are rather flat at UV wavelengths (Kennicutt et al. 1998), it then follows that:

$$F_{UV}^{\text{abs,local}} = \frac{L_{UV}^{\text{abs,local}}}{\Delta\nu(UV)} \quad (4.4)$$

and

$$F_{UV}^{\text{abs,diffuse}} = \frac{L_{UV}^{\text{abs,diffuse}}}{\Delta\nu(UV)} \quad (4.5)$$

where $\Delta\nu \approx 1.8 \times 10^{15}$ Hz is the UV frequency width. The total obscured UV luminosity density $F_{UV}^{\text{abs}} = F_{UV}^{\text{abs,local}} + F_{UV}^{\text{abs,diffuse}}$ and SFRs are shown in cols. 6 and 7 of Table 4.1.

As a check of the consistency between our method to derive star formation rates and the $H\alpha - 24\mu\text{m}$ SFR relation of Calzetti et al. (2007), we used the latter to derive SFR for the compact star formation regions in SQ which are the objects closest resembling galaxian star formation regions. The $H\alpha$ fluxes have been measured on the interference filter maps published in Xu et al. (1999) while the $24\mu\text{m}$ fluxes are those derived by aperture photometry (Sect. 2.2.1). The results are shown in cols. 2 and 3 of Table 4.1. As one can see comparing cols. 3 and 7 of that table, the SFR inferred with our method are consistent with the results found using the Calzetti relation (except for HII SW but in that case the SED fitting was performed without varying χ_{color} because of the non detection of the source at $160\mu\text{m}$.)

Source	$L(H\alpha)^a$ ($10^{40} \frac{\text{erg}}{\text{s}}$)	$SFR_{H\alpha}$ ($\frac{M_{\odot}}{\text{yr}}$)	F_{UV}^{direct} ($10^{27} \frac{\text{erg}}{\text{s Hz}}$)	$L_{\text{dust,UV}}$ ($10^{42} \frac{\text{erg}}{\text{s}}$)	F_{UV}^{abs} ($10^{27} \frac{\text{erg}}{\text{s Hz}}$)	SFR_{UV} ($\frac{M_{\odot}}{\text{yr}}$)	SFR_{UV}/A ($10^{-3} \frac{M_{\odot}}{\text{yr kpc}^2}$)	$\Sigma(HI)$ ($\frac{M_{\odot}}{\text{pc}^2}$)	$\Sigma(H2)$ ($\frac{M_{\odot}}{\text{pc}^2}$)	$\Sigma(H^+)$ ($\frac{M_{\odot}}{\text{pc}^2}$)	Z_d^b
SQ A	$9. \pm 2$	0.7 ± 0.2	2.75	8.09	4.49	0.78	6.4	7.9	6.0	-	0.002
HII SE	6.6 ± 1.5	0.5 ± 0.1	2.32	5.44	3.02	0.58	5.8	$< 0.40^3$	-	-	-
HII SW	3.9 ± 0.5	0.2 ± 0.04	2.11	1.99	1.10	0.35	5.5	3.2	$< 1.7^c$	-	-
SQ B	1.3 ± 0.3	0.2 ± 0.05	0.31	4.18	2.32	0.28	2.7	5.2	4.0	-	0.002
NGC7319	-	-	2.01	-	-	$\gtrsim 0.22$	-	-	-	-	-
Shock	-	-	6.98	5.09	2.83	1.05	3.1	-	9.1	3.0	0.007
Extended	-	-	22.7	30.21	16.78	4.26	1.0	-	-	2.4	0.01

Table 4.1: Measured optical–UV luminosities, star formation rates and gas amount for the detected SQ dust emitting sources. Col1: source name; col2: $H\alpha$ luminosity; col3: star formation rate derived from the $H\alpha$ and $24\mu\text{m}$ luminosity using the relation given by Calzetti et al.07; col4: observed GALEX FUV luminosity density corrected for Galactic extinction; col5: UV powered infrared dust luminosity; col6: absorbed UV luminosity density derived by dividing the UV powered dust luminosity $L_{\text{dust,UV}}$ by $\Delta\nu(UV) = 1.8 \times 10^{15}$ Hz; col7: SFR based on the inferred total (obscured and unobscured) UV luminosity density, using the relation by Salim et al.07; col8: star formation rates in col7 divided by the projected emission area; col9: average neutral hydrogen mass column density; col10: average molecular hydrogen mass column density; col11: average X-ray emitting plasma mass column density; col12: dust to gas ratio Z_d (note that for each source only the corresponding available gas masses are considered for the estimate of Z_d)

^a We measured the $H\alpha$ fluxes from the interference filter maps published in Xu et al.1999. The quoted flux uncertainties are the quadratic sum of background fluctuations and flux calibration uncertainty ($\approx 10\%$).

^b The dust to gas ratio is equal to $Z_d = M_d / (1.4 \times M_{\text{gas}})$ where M_d is the dust mass inferred by the SED fit, M_{gas} is equal to $N(H) \times \pi R^2$ with $R = FWHM(\text{rad}) \times \text{distance}$ the source size as derived from the $70\mu\text{m}$ source fit (the factor 1.4 is applied to take into account the contribution from noble gasses).

^c The value of $\Sigma(HI)$ for HII SE is an upper limit because HI is not detected at that position on the maps by Williams et al.02. No value is given for $\Sigma(H2)$ because the area wasn't observed by Lisenfeld et al.2002. The value of $\Sigma(H2)$ for HII SW is an upper limit because CO has not been detected at that position.

4.2.2 Gas Masses

In the absence of a homogeneous set of observations of gas tracers for the gas phases of interest, namely HI, H₂ and X-ray emitting plasma, we proceeded differently for the several sources in determining gas masses. For the star formation regions SQ A, HII SE, HII SW and SQ B we measured gas mass column densities from the HI map published by Williams et al. (2002), shown in Fig. 2.1, and the CO pointed observations of Lisenfeld et al. (2002), whose distribution on the SQ field is shown in Fig. 4.2. Specifically, we measured the average atomic and molecular hydrogen column density in the observed areas close to the position of the starburst regions. The inferred gas mass column densities are shown in col. 9 and 10 of Table 4.1 (note that for some values only upper limits are available and no CO observation are available for HII SE). Gas in the shock region is mainly in the form of X-ray emitting plasma and molecular gas (Guillard et al. 2009). From the X-ray luminosities, measured by Trinchieri et al. (2005), we determine the X-ray gas mass $M_X \approx 10^9 M_\odot$ (see Sect. 3.2.4 for details). Dividing the total gas mass by the physical area covered by the shock (330kpc^2), we obtained the hot gas mass surface density shown in col. 11 of Table 4.1. To determine the molecular gas mass surface density, we measured the average of several observed positions within the shock area on the CO maps by Lisenfeld et al. (2002) to obtain $\Sigma(H_2) = 9 M_\odot/\text{pc}^2$. As one can see from Fig. 4.2, most of the observations were performed in the upper part of the shock region. Guillard et al. (2010) and Appleton et al. (2006) found that the cold and warm molecular gas surface mass densities in the central parts of the shock region are respectively equal to $5 M_\odot/\text{pc}^2$ and $3.2 M_\odot/\text{pc}^2$. Interestingly enough, the sum of these two values is very close to the cold molecular gas surface density measured in the upper parts of the shock region. For the extended emission, the measurement of the corresponding neutral and molecular gas masses cannot be realistically performed because the extended emission cover irregular parts of the large HI distribution in SQ and there are no CO observations covering the whole group with enough sensitivity to detect a plausible extended molecular hydrogen distribution. The measurement of the corresponding X-ray emitting gas mass is

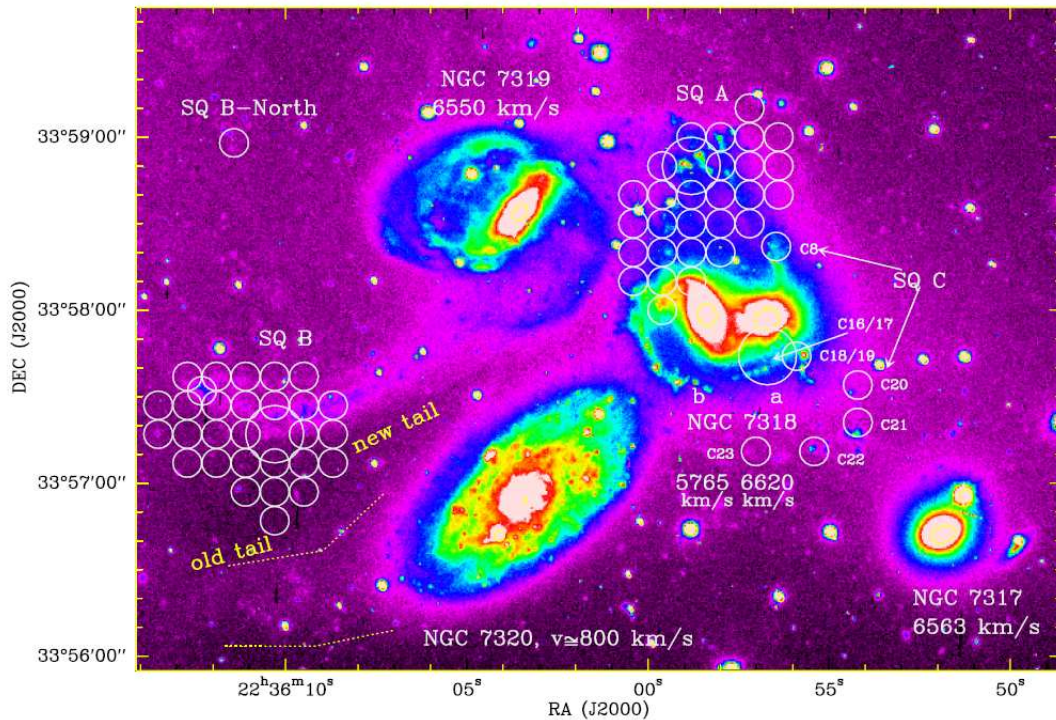


Figure 4.2: Fig. 1 from Lisenfeld et al. (2002) showing the positions of the CO observations presented in that paper

instead rather straightforward since it can be derived from the X-ray Halo luminosity, as for the shock region (Sect. 3.2.4). Dividing the total X-ray gas mass by the projected X-ray halo emission area (a circle of radius ≈ 40 kpc), we determined the hot gas mass surface density shown in col. 11 of Table 4.1.

4.3 Star formation in SQ

The results of the SED fitting to the constituent components of SQ (Sect. 3.1) indicate that star formation activity and photons from old stars are the major agents powering the observed global dust emission from the group, supplemented by photons produced by the accretion flows in the AGN and possibly, in the case of the X-ray emitting regions, by collisional heating. In our quantitative discussion of star formation activity in SQ we will adopt an initial working hypothesis that the

collisional heating mechanism is minor compared with photon heating in the X-ray sources. We will scrutinize this hypothesis in detail in Chapter 5.1, where we discuss physical constraints of the fraction of the infrared emission that can be collisionally powered.

Under this working hypothesis we can gather together the information from Table 4.1 to obtain a total global star formation rate of $7.5 M_{\odot}/yr$ for SQ in its entirety. This global star formation rate doesn't seem particularly discrepant from that typically found for most of the galaxies of similar mass in the local Universe that are clearly not so strongly interacting as SQ galaxies. Using the empirical relation between galaxy stellar mass and SFR for field galaxies shown in Fig. 17 of Brinchmann et al. (2004) (here reproduced in Fig. 4.3) we can estimate the typical SFR of galaxies having the same stellar mass of SQ galaxies, of order of $\approx 10^{11} M_{\odot}$ (see Table 4.2). For this value of the stellar mass, the mode of the distribution is at $SFR \approx 1 M_{\odot}/yr$. Therefore, the typical total star formation rate predicted for four galaxies of the same mass as SQ galaxies is $\approx 4 M_{\odot}/yr$, comparable with the value we have measured. Thus it seems that the star formation efficiency of SQ in relation to field galaxies is largely independent of whether the gas is inside or outside the main stellar disk. In fact, of the total global star formation rate of $7.5 M_{\odot}/yr$ for SQ, 2.2 and $5.3 M_{\odot}/yr$ can respectively be ascribed to the SED components for star formation regions and X-ray sources in Fig. 4.1. This is a very remarkable result indicating, as it does, that the bulk of star formation activity in SQ is apparently associated with X-ray emitting structures, occurring far away from the galaxy centers, either at the peripheries of the galaxies or in the intergalactic medium. Furthermore, the total extragalactic SFR is well in excess of the SFRs of the previously studied individual examples of extragalactic compact star formation regions, SQ A and SQ B.

To quantify the efficiency of star formation in the various components of SQ in relation to that of the disks of individual galaxies, we plotted in Fig. 4.4 the SFR per unit area for dust emission sources in SQ as a function of the gas mass surface density. On the same diagram, as reference, we plotted the relations found by Kennicutt et al. (2007) (K07) and Bigiel et al. (2008) (B08) for star formation regions inside nearby

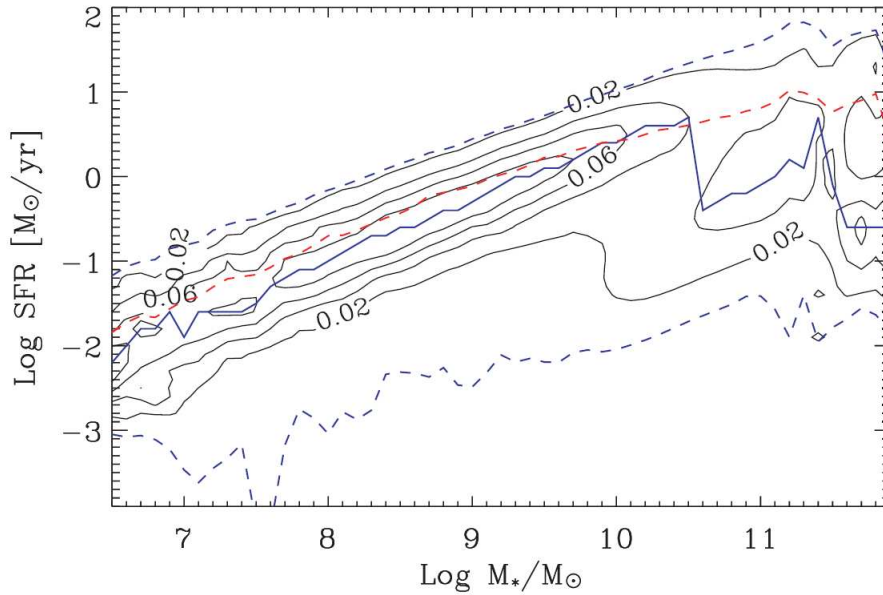


Figure 4.3: Figure 17 from Brinchmann et al. (2004) showing the relation between SFR and stellar mass as found in that paper. The contours show the conditional likelihood of SFR given a stellar mass. The red line shows the average at a given stellar mass, whereas the blue line shows the mode of the distribution. The dashed lines show the limits containing 95 per cent of the galaxies at a given stellar mass.

spiral galaxies. This figure shows a wide range of star formation efficiencies, which we discuss below for each of the structural components, with special emphasis on the extended component of star formation which dominates the global SF activity in SQ.

4.3.1 Discrete Star Formation Regions

Fig. 4.4 shows that SQ A and SQ B, have star formation rates very similar to those observed for galaxian regions with the same gas column density, despite their being located well outside the galaxies of the group. The situation is however different for the other two bright star formation regions, HII SE and HII SW, which present much higher SFRs than those predicted by the plotted relations. This might in principle be due to a more efficient mode of star formation happening in those

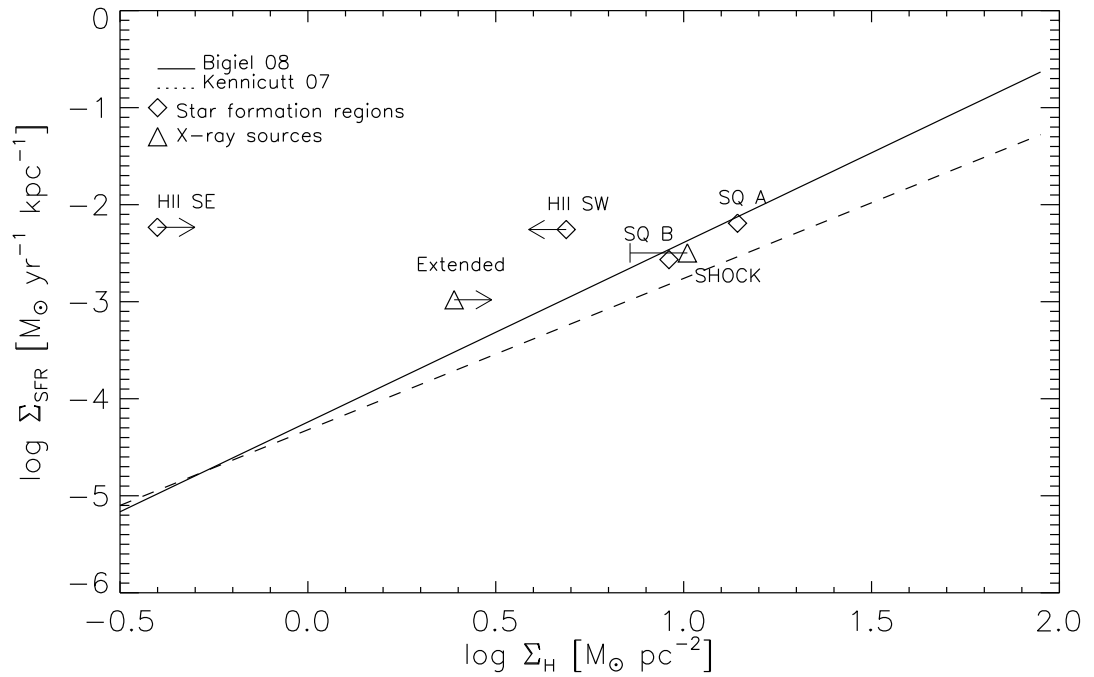


Figure 4.4: Star formation rate per unit area Σ_{SFR} ($M_{\odot}/\text{yr}/\text{kpc}^2$) vs total gas mass surface density Σ_{H} (M_{\odot}/pc^2) for dust emission sources in SQ. The plotted lines are the relations found by Kennicutt et al.07 and Bigiel et al.08. The arrows pointing towards right/left for some of the plotted measurements indicate that the corresponding Σ_{H} value is a lower/upper limit (see Table 4.1). In the case of the shock region point, whose Σ_{H} value is the sum of both cold and hot gas components, a bar extends towards the left until the point where Σ_{H} corresponds to the cold gas mass surface density for this source.

Source	g	r	M_*^1
NGC7319	13.58	12.83	1.6
NGC7318a	15.00	14.06	0.8
NGC7318b	13.31	12.55	2.1
NGC7317	14.58	13.78	0.8

Table 4.2: Galaxy optical photometry and stellar masses. Col1: source name; col2-3: SDSS g and r apparent magnitudes; col4: galaxy stellar mass ($10^{11}M_\odot$)

¹The stellar mass has been estimated using one of the relations given by Bell et al. 2003 to calculate the stellar mass to luminosity ratio from SDSS magnitudes: $\log_{10}(M/L_g) = -0.499 + 1.519 \times (g - r)$ (note that M/L_g is in solar units)

regions, particularly in the case of HII SE, which has an HI gas exhaustion timescale equal to $7 \times 10^7 yr$. It would be of interest to acquire more complete information on the gas content of these sources to further investigate this conjecture.

An alternative explanation for the high SFR found in HII SE and HII SW is that there is an additional component of UV emission produced by the radiative cooling of shocked gas. These UV photons, unrelated to star formation phenomena, can in principle contaminate the UV flux measurement but also power part of the observed dust emission, thus leading to an overestimation of the SFR. Optical spectra of these regions show evidences of line shock excitation (P.-A. Duc, private communication), therefore one cannot rule out this possibility.

4.3.2 Star formation associated with the Shock

The average SFR in the shock region ($3.1 \times 10^{-3} M_\odot/yr/kpc^2$) seems to be well in agreement with the empirical SFR–gas surface density relation in Fig. 4.4. Thus, at first sight, the shock does not seem to have had much effect on the star formation activity in the stripped interstellar gas, neither triggering enhanced star formation through shock–compression of dense clouds of gas, nor suppressing star formation through heating and dispersion of the clouds. The observational situation is however complex in that the star formation observed towards this region could be happening

inside the extended features connected with the incoming galaxy NGC7318b, seen through, but not obviously physically co-existent with the shock region. This is supported by the local morphology of the UV and MIR emission that seems to follow the optical shape of the intruder, instead of showing a linear north–south ridge resembling the shocked gas emission morphology. These two scenarios could in principle be combined since the ISM of the intruder galaxy has presumably been shocked as well and this could have triggered the observed star formation out of the gas associated with the intruder galaxy. In addition, it is conceivable that some fraction of the UV luminosity, albeit probably a minority, could be due to gas cooling rather than from massive stars.

It is also of interest to compare our constraints on the SFR in the shock region with the luminosity of the radio synchrotron emission from the shocked gas. Traditionally radio synchrotron measurements are compared to infrared emission measurements in the context of the radio–FIR correlation for individual galaxies, for which we use here the relation given by Pierini et al. (2003):

$$\log L_{1.4 \text{ GHz}} = 1.10 \times \log L_{FIR} - 18.53 \quad (4.6)$$

where $L_{1.4 \text{ GHz}}$ is the luminosity at $\nu = 1.4 \text{ GHz}$ in units of $W \text{ Hz}^{-1}$ and L_{FIR} is the total FIR luminosity in units of W . We used the relation from Pierini et al. (2003) since it was derived from data covering cold dust emission longwards of $> 100\mu\text{m}$, where, as in the case for the SQ shock region, most of the power is radiated. Using the value we measured for the shock region FIR luminosity, $L(FIR) = 1.5 \times 10^{36} \text{ W}$, we obtain for the predicted radio luminosity $L_{1.4 \text{ GHz}} = 1.8 \times 10^{21} \text{ W Hz}$. This value is 20 times smaller than the radio luminosity derived from the radio measurement in Xu et al. 03: $L_{1.4 \text{ GHz}} = 3.7 \times 10^{22} \text{ W Hz}$, thus lending further support to the hypothesis that the shock is not triggering enhanced star formation. The high radio/infrared luminosity ratio (which would be higher still with respect to the photon–powered component if collisional heating was important) instead points to the existence of an additional source of relativistic particles in the SQ shock, accelerated at the shock itself (see e.g. Blandford & Eichler 1987), which dominates the population of particles accelerated in sources more directly linked to star formation regions such as

supernova remnants. This confirms and strengthens the preliminary results of Xu et al. (2003), and, bearing in mind that the total radio emission from SQ is dominated by the emission from the shock region, suggests that caution is needed in using radio synchrotron measurements to infer star formation rates in groups involving strong dynamical interactions of galaxies with the IGM.

4.3.3 Star Formation associated with the Extended Emission

Our measurements have shown that both the obscured and visible components of the star formation in SQ are distributed in a widespread pattern, loosely coincident both with the overall dimensions of the group as well as with the extended “halo” of X-ray emission. As for HII SE and HII SW, the point on the Kennicutt–Schmidt diagram representing this extended emission is well removed from the relations found for spiral galaxies, raising the question whether a complete different mode of star formation activity is prevalent in this component of SQ.

Specifically we consider a scenario in which the hot intergalactic medium is cooling and condensing into clouds which are the sites of the star formation providing the UV powered component of the extended infrared emission. If this is occurring in a steady state, in which the rate at which the removal of hot gas by cooling is balanced by accretion of further primordial gas, we can write

$$SFR_{\text{hot}} \leq \frac{M_{\text{hot}}}{\tau_{\text{hot}}} \quad (4.7)$$

where M_{hot} and τ_{hot} respectively denote the mass and cooling timescale of the X-ray emitting medium, and the inequality denotes the fraction of the cooling gas that ultimately condenses into stars. If the observed X-ray emission is the main component of luminosity of the hot medium, and taking observational values for the X-ray emitting plasma from Trinchieri et al. (2005) of $M_{\text{hot}} = 1.0 \times 10^{10} M_{\odot}$ and $\tau_{\text{hot}} \sim 0.3 \times 10^{10} \text{yr}$ we obtain $SFR_{\text{hot}} \leq 3 M_{\odot} \text{yr}^{-1}$, comparable to the observed value of $4.3 M_{\odot} \text{yr}^{-1}$ for star formation seen towards the X-ray emitting halo. In reality, however, one would expect a large fraction of the cold gas resulting from

the cooling of the gas to be recycled into the hot medium due to the feedback of mechanical energy from the newly-formed stars, in which case SFR_{hot} would be substantially less the upper limit from Eqn.4.7. Thus, if X-ray emission driven by gas-gas collisions is the dominant cooling path for the X-ray halo, one would conclude that the bulk of the star formation would not be directly fuelled out of the IGM. On the other hand, as shown in Sect.5.3, our Spitzer FIR data, coupled with astrophysical constraints on the injection rate of grains into the hot medium do not at present rule out the possibility that the dominant cooling mechanism of the halo is FIR emission driven by gas-grain collisions. At present, therefore, we cannot rule out star formation out of a primordial IGM purely on considerations of gas fuelling.

A more powerful constraint would be to consider the efficiency at which such a mode would have to operate at. Unfortunately, the total mass of molecular cold gas, M_{cold} on a global scale in the halo is unknown, preventing a direct empirical measurement of star formation efficiency of the halo on the KS diagram. One can however estimate M_{cold} under our simple steady state scenario by writing

$$\frac{M_{\text{hot}}}{\tau_{\text{hot}}} \approx \frac{M_{\text{cold}}}{\tau_{\text{cold}}} \quad (4.8)$$

where τ_{cold} is the typical time scale spent by the gas in the cold molecular phase before being converted into stars, which is the timescale for the collapse of a molecular clouds to form stars, multiplied by the mean number of times the cold gas is recycled into the hot medium through mechanical feedback before condensing into a star. Even allowing for several cooling cycles of the hot gas before condensing into stars, the very short collapse timescale of a few million years for molecular clouds - some two orders of magnitude shorter than τ_{hot} - makes it likely that $\tau_{\text{hot}} \gg \tau_{\text{cold}}$, which in turn implies $M_{\text{hot}} \gg M_{\text{cold}}$. If this is the case, the cold gas amount, related to the extended emission, that we should add to Σ_{gas} would be negligible, and the position of the point for the SQ halo on the KS diagram would be well to the left of the relation for star-forming galaxies, as shown in Fig. 4.4. This would require a more efficient star formation process in the IGM than is typically observed to occur in the disks of star-forming field galaxies, which would seem to be counter-intuitive to the naive expectation that denser, colder reservoirs of gas closer to the minimum

of the gravitational potential wells associated with individual galaxies should form stars more easily. On the other hand a definition of efficiency in terms of gas surface density over scales much larger than the star formation regions may have limited predictive power in this context. Furthermore, any star formation in a cooling hot IGM would not be expected to occurring in rotationally supported systems similar to the galaxies used to define the KS relation, so may have a different relation to the local gas density.

The second, more conventional scenario to explain the widespread star formation in the extended halo component of SQ, is to invoke interstellar gas as the source of cold gas fuelling the star formation. In this scenario tidal interactions between galaxies or hydrodynamical interactions of the ISM with the IGM remove cold galaxy material that, for SQ, produces a similar SFR as would have been the case for a similar amount of gas inside field galaxies. For groups in general the statistical relation of neutral gas observed within and outside the member galaxies to the X-ray emission characteristics of the IGM indeed indicates that at least some of the cold gas in the IGM medium originates in the galaxies, and that at least some of the X-ray emitting gas also has an interstellar origin (eg. Verdes-Montenegro et al. 2001; Rasmussen et al. 2008).

In SQ, there is direct morphological evidence for bursting sources associated with tidally removed interstellar gas in the form of SQ A and SQ B, and a hint that other less prominent components of the FIR emission in the IGM may also be associated with tidal features, such as the enhancement of $H\alpha$ and MIR/FIR emission seen towards the bridge linking the intruder galaxy with the AGN host galaxy. In this picture the extended emission is a conglomeration of discrete sources similar in nature to SQ A and SQ B but much more numerous and of lower power. The fact that SQ A and SQ B are likely to have a fundamentally interstellar origin despite their present location outside the galaxies is further supported by the rather high value of the dust to gas ratio we have found for these sources, $Z_d = 0.002$, which is a signature of a high gas metallicity. The one puzzling aspect of the extension of this scenario to the global star formation in the IGM of SQ is however the lack of prominent star formation associated with the bulk of the HI in the IGM located to

the South and East of the group.

Finally, we remark that if stripped neutral and molecular interstellar gas was the only source of cold gas powering star formation, one would expect a rapid quenching of star formation activity in SQ in the future, whereas if the star formation were fuelled by a cooling primordial IGM, the star formation activity would simply follow the accretion rate onto the group of the primordial IGM.

4.4 The AGN galaxy NGC7319 dust emission

The Seyfert2 galaxy NGC7319 is the most powerful source of IR emission in SQ and is the only galaxy where we found enhanced infrared emission in the central regions. The total IR luminosity is 9.6×10^{43} erg/s. Of this, we deduced from the SED fitting using a combination of the AGN torus template and the diffuse dust emission component (see Sect. 3.1.2) that 4.1×10^{43} erg/s are emitted by dust in the torus and 5.5×10^{43} erg/s by diffuse dust. As one can see from the SED best fit, shown in Fig. 3.2, the $24\mu\text{m}$ MIR emission is dominated by the torus emission which also contributes $\approx 25\%$ of the $8\mu\text{m}$ emission. This is consistent with the observed morphology at 8 and $24\mu\text{m}$ emission, which is a combination of a central source plus a disk component in the case of the $8\mu\text{m}$ map and a dominant central source in the case of the $24\mu\text{m}$ map (see Fig. 2.1). According to the SED fit, the FIR 70 and $160\mu\text{m}$ emission is due to diffuse dust emission. This is also consistent with the brightness distributions on the Spitzer FIR maps which show the emission to be partially resolved, with extents inferred from the FIR map fitting technique of 5 and 12 *kpc* at 70 and $160\mu\text{m}$ respectively. This extended FIR emission is centred at the position of the AGN, potentially indicating the presence of star formation regions distributed on *kpc* scales in the surrounding areas. However, as one can see from Fig. 4.5, reproducing Fig. 1c from Gao et al. (2000), the CO emission is predominantly from the northern regions of this galaxy. Therefore the locations of the bulk of cold gas, where the star formation sites should be, and the cold dust emission are not coincident suggesting that star formation may not be the main phenomena powering the FIR dust emission.

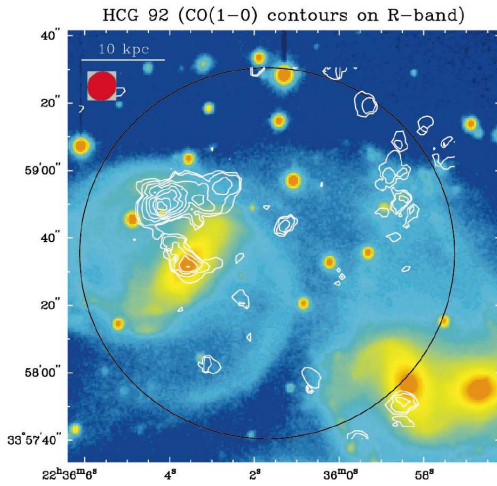


Figure 4.5: Figure 1c from Gao et al. (2000) showing the contours of the distribution of molecular gas in the galaxy NGC7319 overlaid on an R-band image.

Overall, the diffuse dust emission in the inner disk, together with the absence of HI (Williams et al. 2002) and the displacement of the molecular hydrogen emission suggest that galaxy–galaxy interactions have removed gas from the central regions on kpc scales, as has plainly also happened in the other late-type SQ galaxies. In the case of NGC7319, the interactions have apparently also induced gas flows that have triggered AGN activity. This raises the question whether the AGN itself might be the source of photons powering the surrounding diffuse dust emission in this galaxy. According to the standard AGN unification theory, the AGN torus of a Seyfert 2 galaxy is viewed edge on, which, in the case of NGC7319, would imply that the plane of the torus is almost perpendicular to the galaxy disk, since NGC7319 is seen basically face on (see SDSS g-band map in Fig. 2.1). In this configuration, it would indeed be plausible that accretion powered radiation, escaping into the polar direction from the AGN torus structure could propagate into the galaxy disk and contribute to the diffuse radiation field in the central parts of the galaxy. An especially efficient coupling between the dust and radiation would be expected if the polar axis of the AGN torus were to be parallel to the diffuse dusty disk of the host galaxy.

One indirect indication that the radiation from an AGN with this orientation may

be responsible for at least part of the diffuse FIR emission in NGC 7319 comes from the rather low observed UV/FIR luminosity ratio, which is qualitatively consistent with the expected strong attenuation of the direct UV light from an AGN to which the line-of-sight passes through the torus. From the measured FUV luminosity, $L_{FUV} = 4 \times 10^{42}$ erg/s, and from the 60 and 100 μ m luminosities extrapolated from the SED best fit, $L_{60\mu\text{m}} = 2 \times 10^{43}$ erg/s and $L_{100\mu\text{m}} = 3.7 \times 10^{43}$ erg/s, we have found $L_{FUV}/L_{60\mu\text{m}} = 0.2$ and $L_{FUV}/L_{100\mu\text{m}} = 0.1$. These values are several factors lower than the average values found by Popescu et al. (2002) for galaxies of similar morphological type ($L_{UV}/L_{60\mu\text{m}} = 1$ and $L_{UV}/L_{100\mu\text{m}} = 0.6$) and by Xu et al. (2006) for galaxies of similar $L_{FUV} + L_{60\mu\text{m}}$ total luminosity ($L_{UV}/L_{60\mu\text{m}} = 0.5$).

A scenario in which the diffuse dust emission in NGC7319 is powered by the AGN also seems to be broadly consistent with simple constraints on the UV luminosity of the AGN derived from the observed hard X-ray luminosity. Specifically, for $L_{2-10 \text{ keV}} = 2.8 \times 10^{42}$ erg/s (Trinchieri et al. 2005) and adopting the bolometric corrections for AGN galaxies with similar $L_{2-10 \text{ keV}}$ by Vasudevan et al. (2010), $\kappa_{2-10 \text{ keV}} \approx 10 - 30$, one predicts a total UV luminosity from the AGN of $L_{AGN} = \kappa_{2-10 \text{ keV}} L_{2-10 \text{ keV}} = 2.8 - 8.4 \times 10^{43}$ erg/s. The upper end of this range is comparable to the total MIR/FIR luminosity of the AGN and AGN host galaxy. If the AGN were indeed powering the diffuse dust emission in the inner disk one would expect that future FIR observations of angular resolution sufficient to image the diffuse dust emission could be used to determine some basic geometrical properties of the AGN. Specifically, one would expect a cone structure for the component of diffuse dust heated by the AGN, blurred only by the effect of scattering, with a strong radial colour gradient, and with a symmetry axis aligned with the polar axis of the torus.

Finally, we draw attention to a further FIR-emitting feature potentially connected to the AGN, whose origin has still to be clarified. This is the bridge which apparently connects the AGN to the center of the shock region, appearing in the X-ray (Trinchieri et al. 2005), $H\alpha$ (Xu et al. 1999) and warm H_2 line emission (Cluver et al. 2010). The presence of a cold dust emission from this feature is hinted by a slight asymmetry of the FIR emission on the 160 μ m residual map (see Fig. 2.4).

High resolution FIR observations would also be useful to elucidate the correspondence between dust emission and the gas distribution in this bridge feature.

Chapter 5

Dust emission from SQ X-ray emitting regions

5.1 Introduction

Previous searches for infrared emission counterparts of the hot X-ray emitting components of the intergalactic medium of nearby objects have almost exclusively targeted the intracluster medium (ICM) of rich galaxy clusters, either using a stacking analysis for X-ray or optical selected clusters from the IRAS all sky survey (Giard et al. 2008; Roncarelli et al. 2010) or in detailed imaging observations of the Coma Cluster and other clusters with ISO or Spitzer (Stickel et al. 1998; Quillen et al. 1999; Stickel et al. 2002; Bai et al. 2007; Kitayama et al. 2009). All these studies have either yielded upper limits or marginal apparent detections of the ICM at FIR brightness levels far fainter than those we have measured towards the X-ray emitting IGM of SQ with Spitzer. Furthermore, even the apparent detections of the ICM were susceptible to confusion with foreground cirrus due to the accidental similarity (Popescu et al. 2000) in FIR colour of the collisionally- and photon-heated emissions, so realistically must be treated as upper limits to any collisionally heated emission from the ICM (Bai et al. 2007). Although intracluster dust has been unambiguously detected at optical wavelengths, through statistical studies of the reddening of background sources through large numbers of clusters (Chelouche

et al. 2007) this has been at a low abundance of about 10^{-4} in the dust-to-gas mass ratio, consistent both with the non-detections of the ICM in infrared emission and with specific predictions by Popescu et al. (2000) of the dust content of typical ICMs.

In the present work we have been able to sidestep the confusion problems afflicting the previous attempts to detect infrared emission from the ICM in clusters only by virtue of the much higher FIR brightness levels measured towards the X-ray emitting structures in SQ. These high brightness levels, together with the correspondence of the infrared emission morphologies with those seen in the UV, and the evidence from our fits to the infrared emission SEDs described in Sect. 3.1.3 however suggest that a major part of the dust emission is photon heated. This, in turn, raises an apparent paradox that the closest spatial correlation between dust emission and gas column density is not, as might be expected for photon heating, with the cool gas component, but rather with the hot X-ray emitting component. In our discussion on star formation in SQ we identified a possible way out of this paradox by postulating that the extragalactic star formation in SQ is fuelled by gas from a hot IGM whose cooling is enhanced by grains injected into the hot IGM.

In this chapter, we use the relative levels of detected emission at infrared, X-ray and UV/optical wavelengths to constrain the possible sources of grains and the resulting collisionally driven cooling of the hot plasmas, considering separately the two main X-ray emitting structures corresponding to the shock (Sect. 5.2) and the halo (Sect. 5.3) regions.

5.2 The shock region

The main constraint on the collisional heating of dust in the X-ray emitting plasma downstream of the shock is given by the high dust-to-gas mass ratio that would be required to reproduce the FIR measurements in the case that grain heating by a diffuse radiation field can be neglected. For pure collisionally heated emission from grains in a homogeneous medium, a dust mass $M_d = 2 \times 10^7 M_\odot$ (see Sect. 3.1.3) would be required, which, taken together with the measured X-ray emitting gas

mass, $M_X \approx 10^9 M_\odot$ (see Sect. 3.2.4), would imply a dust-to-gas ratio for the hot plasma of $Z_d = 0.02$. This value is high in comparison with expectations based on a balance between injection of grains and their removal through sputtering. Assuming that the shock is propagating into a stripped interstellar medium or through the ISM of the intruder galaxy, characterized by a dust-to-gas ratio comparable to the Milky way value, we can derive the amount of dust mass per unit time \dot{M}_D that is injected downstream of the shock:

$$\dot{M}_D = V_{\text{sh}} A \rho_{\text{up}} Z_{\text{d,up}} \quad (5.1)$$

where $V_{\text{sh}} = 600 \text{ km/s}$ is the shock velocity (Guillard et al. 2009), $A = 330 \text{ kpc}^2$ is the projected area of the shock front (corresponding to $20 \times 80 \text{ arcs}^2$ on the sky), $\rho_{\text{up}} \approx 1.1 n_H m_H = 4.5 \times 10^{-27} \text{ g/cm}^3$ is the upstream gas density ($n_H = 0.01/4. \text{ cm}^{-3}$) and $Z_{\text{d,up}} = 0.01$ is the assumed dust to gas ratio for the gas upstream of the shock front. The resulting dust injection rate is $\dot{M}_D = 0.14 M_\odot/\text{yr}$. To estimate grain destruction through sputtering in collisions with heavy particles we use the formula of Draine et al. (1979) for the dust sputtering time scale:

$$\tau_{\text{sp}} = 2 \times 10^6 \frac{a}{n_H} \text{ yr} \quad (5.2)$$

where a is the dust size in μm and n_H is the proton number density in cm^{-3} . Assuming $n_H \approx 0.01 \text{ cm}^{-3}$ and $a = 0.1 \mu\text{m}$, we get $\tau_{\text{sp}} = 2 \times 10^7 \text{ yr}$. We will show in Chap. 6 that explicit calculation of the cooling of the shock gas due to gas-gas and gas-grain collisions, taking into account the evolution of the grain size distribution (under the assumption that there are no further sources of grains), show that the gas cooling time scale is $t_{\text{cool}} \approx 7 \times 10^7 \text{ yr}$, more than three times larger than τ_{sp} . Under these circumstances a conservative estimate for the dust to gas ratio downstream of the shock can be derived by dividing the total mass of dust predicted to be at any time downstream of the shock to the measured hot gas mass, that is:

$$Z_{\text{d,down}} = \frac{\dot{M}_D \tau_{\text{sp}}}{M_X} \quad (5.3)$$

Applying this formula, the expected value for the X-ray plasma dust to gas ratio is $Z_{\text{d,down}} \approx 3 \times 10^{-3}$, a factor ≈ 7 smaller than the value inferred from the data, for the case where the entire FIR dust emission is powered by collisional heating. This

is only a crude estimate for the dust abundance, which might take higher values if the line of sight depth of the shock was assumed to be larger than the projected width seen on the sky, but which on the other hand is an overestimate compared to predictions taking into account the true evolution of grain size downstream of the shock (see Chap. 6). In any case, it is evident that the measured dust to gas ratio is much larger than the predicted $Z_{d,down}$, and a further source of dust grains would be required if collisional heating were to be a significant driver of the FIR emission.

The most obvious such source would be the reservoir of grains in the cold component of the gas in the shock region, which could be potentially released into the hot gas by ablation if the clouds were in relative motion to the hot gas. As already mentioned the presence of cold gas is implied by the detection of $8\mu\text{m}$ emission and has been directly demonstrated by the detection of molecular hydrogen in the MIR rotational lines (Cluver et al. 2010). Guillard et al. 2009 modelled the H_2 emitting clouds as cooling pre-existing clouds in the upstream medium, a scenario which would predict the clouds to be in relative motion to the hot gas downstream of the shock. Another possibility which might potentially account for a FIR counterpart to the shock is to invoke heating of grains upstream of the shock by the UV radiation from the cooling clouds downstream of the shock. A quantitative treatment of all these effects would however require a self consistent model for the passage of the shock through a two phase medium which tracked the exchange of photons, gas and dust between the phases, which is beyond the scope of this work.

It's appropriate to emphasize here that even in the case that the collisional heating is relatively unimportant in bolometric terms, the effect on the gas cooling time scale is not negligible. Detailed calculations, shown in Sect. 6, for a steady state 1D homogeneous model, considering dust sputtering and dust cooling, show that the cooling time scale is shorter by a factor $\approx 2-3$ for shock velocities and gas densities similar to those characteristic of the shock in SQ. From this perspective it would be important to have more direct empirical constraints on the gas cooling mechanism using the improved sensitivity, angular resolution and wavelength coverage of the Herschel Space Observatory. Using the simple approach described above, we estimate the surface brightness of the radiation emitted by collisionally heated dust to

be equal to 1.4 MJy/sr at $150\mu\text{m}$, the wavelength where the flux density is predicted to peak according to the collisional heated dust model we used for the shock region SED fit (see Fig. 3.3).

5.3 The extended emission

As for the shock, the detection of substantial $8\mu\text{m}$ emission towards the extended X-ray emitting halo indicates the presence of a component of dust in cold gas phases, shielded from collisions with electrons and ions in the hot plasma, which can only be heated by photons. Rather interestingly, the curves of growth we constructed after removing or masking the galaxies and the compact star formation regions from the infrared and FUV maps (Fig. 2.9) show a very similar profile at all wavelengths. This is a strong indication that FUV sources are associated with the FIR extended emission and, therefore, star formation is the main mechanism powering the extended emission.

The total luminosity of the extended dust emission is 4×10^{43} erg/s, a factor ≈ 130 higher than the X-ray Halo luminosity (Trinchieri et al. 2005, see also Sect. 3.2.4). This large difference between the dust emission and X-ray luminosities implies that collisional heating of dust grains could still be important for the cooling of the hot halo gas even if it only powers a small fraction of the dust luminosity. We define the fraction F_{coll} of dust emission that is collisionally powered, by the relation:

$$L_{\text{IR}}^{\text{coll}} = F_{\text{coll}} L_{\text{IR}} \quad (5.4)$$

where $L_{\text{IR}}^{\text{coll}}$ is the dust luminosity that is powered by collisional heating.

A first physical constraint on F_{coll} that we can apply is the requirement that the gas cooling time scale τ_{cool} is not larger than the dynamical hot gas time scale, given by the sound crossing time τ_{cross} . Including dust cooling, τ_{cool} is equal to:

$$\tau_{\text{cool}} = \frac{3}{2} \frac{kT}{\mu m_H} \frac{M_X}{L_X + F_{\text{coll}} L_{\text{IR}}} \quad (5.5)$$

where $T = 6 \times 10^6$ K is the gas temperature, $M_X = 1.0 \times 10^{10} M_{\odot}$ is the X-ray emitting gas mass, and L_X and L_{IR} are the X-ray and infrared luminosities.

Requiring that $\tau_{\text{cool}} > \tau_{\text{cross}} = 2R_{\text{halo}}/c_s$, where $R = 35$ kpc is the halo radius and $c_s \approx 300$ km/s is the sound speed, one obtains $F_{\text{coll}} < 0.05$.

Another constraint can be derived from an estimation of the dust injection rate into the hot gas. For equilibrium between dust injection and sputtering, one would have:

$$\dot{M}_d = F_{\text{coll}} \frac{M_d}{\tau_{\text{sp}}} = 2.4 F_{\text{coll}} \frac{M_{\odot}}{\text{yr}} \quad (5.6)$$

where \dot{M}_d is the dust injection rate, $\tau_{\text{sp}} = 2 \times 10^8$ yr is the sputtering time scale (calculated using formula 5.2 with $n_H = 0.001 \text{cm}^{-3}$ and $a = 0.1 \mu\text{m}$), and $M_d = 4.7 \times 10^8 M_{\odot}$ is the inferred dust mass producing the extended emission.

The first dust injection sources we consider are the halo stars. In Sect. 5.A we derive an upper limit to the dust injection rate from halo stars based on the observed R-band halo surface brightness (Moles et al. 1998) and the theoretical predictions for stardust injection by Zhukovska et al.08: $\dot{M}_d = 0.075 M_{\odot}/\text{yr}$. Substituting this value in Eqn. 5.6, we get $F_{\text{coll}} < 0.03$. A similar procedure could be followed considering the dust injection from type II supernovae given the inferred SFR associated with the extended emission. Empirical studies of Galactic supernova remnants have shown the yield of condensate per supernova event to be of the order of 0.01 to 0.1 M_{\odot} (e.g. Fischera et al. 2002, Green et al. 2004). Relating the frequency of core collapse supernova events to the SFR in the extended component of SQ, we estimated $\dot{M}_d = 7 \times 10^{-4} M_{\odot}/\text{yr}$ assuming 0.01 M_{\odot} of dust produced in each supernova. Therefore supernovae dust injection cannot be considered important in replenishing dust in the hot medium. Finally we considered the mechanism proposed by Popescu et al. (2000) where dust in IGM external to a cluster can be introduced into the hot intracluster medium in the supersonic accretion flow of barions onto the cluster. In the case of SQ the baryonic accretion rate can be estimated to be of the order the current IGM seen in X-ray divided by a Hubble time which is $\approx 2 M_{\odot}/\text{yr}$. Even if we consider that there is maybe a cooler component of the accreting IGM not visible in the X-ray (Mulchaey et al. 2000), it does not seem plausible to achieve dust accretion rate for the particular case of SQ much greater than 0.01 M_{\odot}/yr for reasonable values of the dust to gas ratio in the accreting material.

Given these estimates, we can conclude that if there is a contribution of colli-

sional heated dust to the total observed dust emission, this should only be of the order of a few percent and maintained by direct injection from the in situ stellar population. This however is sufficient to maintain a collisionally powered FIR luminosity of up to $\approx 10^{42}$ erg/s, which is several times the X-ray luminosity.

– Consequences for the budget of baryons in groups

Such a level of FIR cooling could help to provide a natural explanation for the rather low value, ~ 0.02 , for the ratio of the mass of baryons in the hot X-ray emitting halo of $\sim M_X = 2 \times 10^{10} M_\odot$ to the dynamical mass of $\sim 10^{12} M_\odot$ (see Sect. 5.B). For the concordance CDM cosmology, this ratio should be ~ 0.09 in the absence of significant dissipative effects. Recalling that the total baryonic mass currently locked in stars in SQ of $\sim 10^{11} M_\odot$ is comparable to the expected total mass of baryons, it is apparent that this scenario is also quantitatively consistent with the efficient condensation of the IGM accreting onto the group into stars, as postulated in Sect. 7.1. Some empirical indication of efficient star formation in groups has been found by Tran et al. (2009), who showed that the group environment is more conducive to star formation than either the cluster or field environment. In general, enhanced cooling due to a FIR collisionally powered luminosity of a few times L_X would also provide an alternative explanation for the steeper $L_X - T_X$ relation observed for groups with lower virial velocities, an effect that is otherwise attributed to thermal or kinetic feedback from AGNs (eg Cavaliere et al. 2008).

In summary, the detection and recognition of the putative collisionally heated component of FIR emission from SQ will be a crucial measurement with wide ranging implications for the nature of star formation in the group, the division of Baryons between hot gas, cold gas and stars, and the thermodynamic properties of the IGM in SQ. Such a detection will however be very challenging, requiring a combination of excellent surface brightness sensitivity and angular resolution at submm wavelengths, as illustrated by the following estimates: assuming the upper limit $F_{\text{coll}} = 0.03$, we predict the SED of the collisionally powered component of the extended emission to peak at a level of 0.15 MJy/sr at $190\mu\text{m}$.

5.A Estimate of an upper limit to the dust injection rate from halo stars in SQ

An upper limit to the dust injection rate from halo stars in SQ can be inferred from the halo R-band surface brightness, $S_R = 24.4 \text{ mag/arcsec}^2$ (Moles et al. 1998), and using theoretical predictions for the stardust injection. We assumed that all the R-band halo luminosity is produced by $3 M_\odot$ stars. According to table A.1 in Zhukovska et al. (2008), a $3 M_\odot$ star with metallicity $Z = 0.02$ injects $M_d = 1.2 \times 10^{-2} M_\odot$ of dust during its all life. Given the lifetime of such star, $\tau_{\text{life}} \approx 3 \times 10^8 \text{ yr}$, one can derive the average dust injection rate: $\dot{M}_d = M_d/\tau_{\text{life}} = 3.5 \times 10^{-11} M_\odot/\text{yr}$. Since a star spends most of its life time in the main sequence phase, we approximate the R-band flux of a single halo star as that of a blackbody sphere with parameters characteristic of a main sequence $3 M_\odot$ star:

$$F_R = \pi B_R(T) \frac{R^2}{d^2} \quad (5.7)$$

where $B_R(T)$ is the blackbody R-band flux density at temperature $T = 12000 \text{ K}$, $R = 2R_\odot$ is the star radius and $d = 94 \text{ Mpc}$ is the distance from SQ. The prediction for the R-band flux density produced by a single halo star and observed from the earth is $F_R = 1.35 \times 10^{-23} \text{ ergs/cm}^2/\text{s}/\text{A}$. Dividing \dot{M}_d to F_R , we obtain the dust injection rate per observed R-band flux density: $\dot{M}_d/F_R = 2.6 \times 10^{12} M_\odot/\text{yr}(\text{ergs/cm}^2/\text{s}/\text{A})^{-1}$. Combining the observed R-band surface brightness and the solid angle Ω covering the halo region of SQ, one can obtain the total received flux $F_R^{\text{obs}} = 2.9 \times 10^{-14} \text{ ergs/cm}^2/\text{s}/\text{A}$. Then the dust injection rate from halo stars is equal to:

$$\dot{M}_d = \left(\frac{\dot{M}_d}{F_R} \right) F_R^{\text{obs}} \quad (5.8)$$

Using this simple approach we found $\dot{M}_d = 0.075 M_\odot/\text{yr}$. This value should be considered as an upper limit since one can show, using the theoretical predictions for low–intermediate mass star dust injection rates in Zhukovska et al. (2008), that $3 M_\odot$ stars have the highest value of the dust injection rate per R-band flux \dot{M}_d/F_R .

5.B SQ dark matter halo mass

The dark matter halo mass in the SQ group can be estimated from the observed galaxy velocity dispersion. Assuming virial equilibrium and that the kinetic energy and gravitational energy are dominated respectively by galaxy motion and by a spherical uniform dark matter distribution, one obtains the following relation:

$$M_{\text{gal}}\sigma_v^2 = G\frac{5M_{\text{DM}}^2}{3R_{\text{DM}}} \quad (5.9)$$

where M_{gal} is the total galaxy mass, σ is the 3D galaxy velocity dispersion, M_{DM} and R_{DM} are respectively the mass and the radius of the spherical dark matter halo. The galaxy velocity dispersion can be calculated by the galaxy recession velocities (Table 1.1), using the formula given by Osmond & Ponman (2004):

$$\sigma_v = \sqrt{\frac{\sum(v - \bar{v})^2}{N - \frac{3}{2}}} \quad (5.10)$$

Including all the galaxies of the group but NGC7318b that is not in equilibrium with the rest of the group, one obtains $\sigma_v = 81\text{km/s}$. Assuming $M_{\text{gal}} = 4 \times 10^{11}M_{\odot}$ (see Table 4.2) and $R_{\text{DM}} = 40\text{kpc}$, a dark matter halo mass $M_{\text{DM}} = 2 \times 10^{11}M_{\odot}$ is derived after inverting Equ.5.9.

Another way to estimate the DM halo mass is from the observed temperature of the X-ray halo, assumed in hydrostatic equilibrium. In fact, in this case temperature T_{200} and halo mass M_{200} are connected by the following relation (Voit 2005):

$$\kappa_B T_{200} = \frac{GM_{200}\mu m_p}{2r_{200}} \quad (5.11)$$

where r_{200} is the dark matter halo radius and the subscript 200 refers to quantities at or within the radius where the gas density is 200 times higher than the critical density $\rho_{\text{crit}} = 3H_0^2/8\pi G$. Assuming $T_{200} = 6 \times 10^6\text{K}$ (Sect.3.2.4) and $r_{200} = 40\text{kpc}$, after inverting equation 5.11 one gets for the dark matter halo mass $M_{200} = 1.8 \times 10^{12}M_{\odot}$.

The two estimates presented differ by an order of magnitude. However the estimate based on the galaxy velocity dispersion is heavily hampered by the low number of galaxies and the consequently inaccurate value for σ_v . Therefore, although the hypothesis of hydrostatic equilibrium might not be completely appropriate for

the hot gas in SQ halo, the second estimate should provide a more realistic value for the dark matter halo mass.

Chapter 6

A shock model with dust cooling

6.1 Introduction

The effect of collisions between dust grains and plasma particles on hot gas cooling has been investigated by several authors. Dwek et al. (1996) presented a shock model, designed to describe the cooling of interstellar gas heated by the passage of supernovae blast waves. In their model they included both dust cooling and dust sputtering, the former providing an extra channel for the cooling of the shocked gas and the latter limiting the overall efficiency of this extra cooling mechanism by quickly destroying the dust grains. These authors found that dust cooling is predominant over gas radiative cooling when gas ionization losses are not efficient anymore, that is, after an initial phase when gas is hot but not completely ionized, and until the abundance of dust is high enough. They concluded that the main effect of dust cooling is to make the shock to become radiative sooner. Smith et al. (1996) and Guillard et al. (2009) modelled the cooling of hot gas in isothermal and/or isobaric conditions. They both found that, although predominant in certain phases, dust cooling has little effect on the thermal history of the gas. This happens because at the high initial temperatures, $T \gtrsim 10^6$ K, produced by strong shocks with velocities v_s higher than ~ 100 km/s, dust sputtering destroys dust before gas has cooled substantially while at temperatures $T \lesssim 10^6$ K ($v_s \lesssim 100$ km/s) dust collisional heating is inefficient and therefore dust–plasma particles collisions don't

contribute to gas cooling.

It is therefore commonly accepted in the literature that dust cooling is an efficient process for short time intervals but removes only a minor part of the gas enthalpy and kinetic energy. However, at the same time, dust cooling is efficient in a temperature range where gas radiative processes are rather inefficient. Therefore it is interesting to quantify how much the gas cooling time is shortened by this additional mechanism. The effect of dust on the gas cooling could be non negligible in this respect, as already stated by Dwek et al. (1996). In addition, for the purposes of this work, we needed a model to predict the FIR $160\mu\text{m}/70\mu\text{m}$ flux ratio produced by dust collisionally heated in a radiative shock with $v_s \approx 600\text{km/s}$, to be compared with the observed flux ratio we found for the SQ shock region. This motivated us to write a code to calculate the post-shock structure profiles of a radiative 1D shock, including dust cooling and destruction and coupled with our program to calculate the infrared emission from stochastically heated grains. Details of the model and results for a set of shock velocities and initial gas densities are shown in the next sections.

6.2 The model

The shock model code we have created is similar to those presented by Dwek et al. (1996) and Guillard et al. (2009) and it is suitable to follow gas cooling in post-shock regions with initial post-shock temperatures $T \gtrsim 10^6$ K. We assumed that dust and gas are completely coupled, that means gas-grains relative motions are neglected, and we included only thermal sputtering as a dust destruction process. This is appropriate for initial post-shock temperatures above $T = 10^6$ K (Dwek et al. 1996). In principle the gas chemical composition should be treated as time-dependent because of the gas metal enrichment following the removal of metals from grains by dust sputtering. However we didn't include this effect in our model.

The basic equations to calculate the fluid evolution in a post-shock region are the Rankine-Hugoniot jump conditions equations that, following Dopita et al. (1996),

can be written as the following set of equations:

$$\rho V = \rho_o V_o \quad (6.1)$$

$$\rho V^2 + P + \frac{B^2}{8\pi} = \rho_o V_o^2 + P_o + \frac{B_o^2}{8\pi} \quad (6.2)$$

$$\frac{B}{\rho} = \frac{B_o}{\rho_o} \quad (6.3)$$

$$\frac{V^2}{2} + U + \frac{P}{\rho} + \frac{B^2}{4\pi} + \bar{\Lambda} \times (t - t_o) = \frac{V_o^2}{2} + U_o + \frac{P_o}{\rho_o} + \frac{B_o^2}{4\pi} \quad (6.4)$$

where $\rho, V, P, B, U = P/[\rho(\gamma - 1)]$ are respectively the fluid density, velocity, pressure, magnetic field and internal energy; the subscript “o” refers to the preshock parameters; $\bar{\Lambda}$ is the average cooling rate over the time interval $t - t_o$; γ is the ratio of specific heats (equal to 5/3 in the monoatomic gas case). These equations are derived from the standard set of hydrodynamical fluid equations, representing the conservation of mass, momentum and energy in the stationary case (that is in the reference frame where the shock front is at rest), together with the condition that the magnetic field is frozen in the fluid. Combining the equations above, the following relation is obtained for the fluid velocity ν :

$$a_1 \nu^4 + a_2 \nu^3 + a_3 \nu^2 + a_4 \nu + a_5 = 0 \quad (6.5)$$

where

$$\begin{aligned} a_1 &= \Gamma - 1, \quad \Gamma = \frac{2\gamma}{\gamma - 1} \\ a_2 &= -\Gamma \left(\frac{P_o}{\rho_o V_o} + V_o + \frac{B_o^2}{8\pi \rho_o V_o} \right) \\ a_3 &= V_o^2 + \Gamma \frac{P_o}{V_o} - 2\bar{\Lambda} \times (t - t_o) + \frac{B_o^2}{2\pi} \\ a_4 &= \Gamma V_o \frac{B_o^2}{8\pi \rho_o} \\ a_5 &= V_o^2 \frac{B_o}{2\pi} \end{aligned}$$

Given the preshock fluid parameters, one can solve 6.5 for the fluid velocity ν at any time t (and then derive all the other fluid physical parameters) if an expression for the cooling rate per unit mass Λ is provided. In our model Λ is given by

$$\Lambda(\rho, T) = \Lambda_{\text{gas}} + \Lambda_{\text{dust}} \quad (6.6)$$

where Λ_{gas} and Λ_{dust} are the cooling rate per unit mass due to respectively gas radiative processes and dust–gas particle collisions. Λ_{gas} is equal to

$$\Lambda_{\text{gas}} = \Lambda_{\text{SD}}(T)n_t n_e / \rho \quad (6.7)$$

where Λ_{SD} is the non-equilibrium cooling function taken from Sutherland et al. (1993) (assuming solar chemical composition, full diffuse field and initial temperature $\log(T_o) = 7.5$) while n_t and n_e are the ion and electron number densities. Λ_{dust} is equal to

$$\Lambda_{\text{dust}} = \frac{L_{\text{dust}}(\rho, T)}{M_{\text{dust}}} \times Z_d \quad (6.8)$$

where $L_{\text{dust}}/M_{\text{dust}}$ is the collisionally heated dust luminosity per unit dust mass and Z_d is the dust to gas ratio. Given the local physical properties of the gas, $L_{\text{dust}}/M_{\text{dust}}$ is calculated using a collisionally heated dust emission code (see Sect. 3.2.4 for details) which provides also the emission SED, from each position downstream of the shock front, taking into account the stochastic heating of small grains.

Modelling the exact evolution of the Z_d term is fundamental to determine the efficiency of dust cooling in the post shock region. In the calculations we performed, we assumed that the dust to gas ratio in the preshock gas is equal to the standard Milky Way local value $Z_d = 0.008$. The initial mixture of dust grains includes graphites and silicates following a power law grain size distribution $n(a) \propto k^{-3.5}$ with sizes between $a_{\text{min}} = 0.001\mu\text{m}$ and $a_{\text{max}} = 0.25\mu\text{m}$. However in the post shock region the value of Z_d decreases with time because dust sputtering gradually removes metals from the grains. Therefore to calculate the dust cooling term Λ_{dust} , directly proportional to Z_d , one has to derive the value of Z_d at each post shock time $t - t_o$. This is done by reconstructing the grain size distribution at each time t in the following way. After a time step $\Delta t = t_i - t_{i-1}$, the size of each grain is reduced by an amount $\Delta a = Y(T)n_h \Delta t$, where $Y(T)$ is the average of the graphite and silicates sputtering yields given in Table 4 of Tielens et al. (1994). The new size distribution at each step is simply given by

$$n(a, t_i) = n(a + \Delta a, t_{i-1}) \quad (6.9)$$

We assumed that when grains become smaller than a_{\min} , they are considered destroyed. The new Z_d is calculated integrating the new grain size distribution $n(a, t_i)$:

$$Z_d = \int_{a_{\min}}^{a_{\max}} \frac{4}{3} \pi \rho_{\text{dust}} a^3 n(a, t_i) da \quad (6.10)$$

Because of the temperature range covered by the cooling function from Sutherland et al. (1993), we followed gas cooling only until temperatures $T \approx 10^4$ K.

6.3 Results

Table 6.1 shows the results for a grid of models with shock velocities $v_s = 500 - 1000$ km/s and pre-shock proton densities $n_H^o = 0.01/4 - 0.1/4$ cm⁻³ (if gas is completely ionized, $n_{\text{gas}} \approx 2.30 \times n_H$). We chose such low values for the pre-shock densities because we wanted to estimate the cooling time of tenuous plasma shock-heated in a high velocity collision as the one in SQ. For the sake of simplicity we neglected the magnetic field that would provide additional internal pressure, delaying gas cooling (however, applying energy equipartition arguments, the magnetic field energy density in the shock region of SQ seems to be much lower than the thermal energy density, see Xu et al. 2003). For each set of input parameters, listed in Table 6.1, we ran a model including only gas cooling and a model including both dust and gas cooling. The different cooling time (defined as the time required to reach $T = 10^4$ K) in the two cases are shown in col.2 and 3 of Table 6.1. For the model where both mechanisms are on, the gas cooling time is shortened by a factor ≈ 3 when $v_s = 500$ km/s. This factor decreases with increasing shock velocities and becomes ≈ 1.4 at $v_s = 1000$ km/s. Therefore we can say that the presence of dust, with Galactic abundance, in the pre shock medium reduces the gas cooling time of a factor of a few but the effect is reduced going towards higher velocities.

It is interesting to notice that the amount of enthalpy plus kinetic energy per unit mass radiated by dust emission range from 10% to 30% (col.10, Table 6.1). This means that dust radiates only a small fraction of the available energy for the fluid but nonetheless the cooling time scale is considerably reduced. The reason for this is that the transfer of energy from the gas to the dust, through dust-gas particle

collisions, is very efficient at high temperatures ($T > 10^6$ K) where gas radiative cooling is very low compared to that at lower temperatures ($T \approx 10^4 - 10^5$ K) where ionization losses make gas cool faster. Therefore dust accelerates the cooling at early phases, that otherwise would be the slowest ones.

Figs.6.1–6.3 show the density, temperature and velocity post shock profiles for a model with $n_H^o = 0.01/4 \text{ cm}^{-3}$ and $v_s = 600 \text{ km/s}$. These parameters are chosen to reproduce the X-ray emitting plasma physical properties of the shock region in SQ (Guillard et al.2009). In each figure the profiles for both purely radiative cooling and radiative plus dust cooling models are shown. It is evident how dust cooling shortens the gas cooling time that drops from $\approx 14 \times 10^7$ yr to $\approx 7 \times 10^7$ yr. The initial rise of density and the steep decrease of temperature and velocity for the dust + radiation model is due to dust cooling. Figs.6.4–6.6 help to understand better what happens during these early phases. Fig. 6.6 shows the dust to gas ratio profile. As can be seen, Z_d drops very quickly because of dust destruction. At $t = 1.8 \times 10^7$ yr, much before than gas cooling is complete, $Z_d = 10^{-6}$. However even before, at $t = 0.8 \times 10^7$ yr, gas radiative cooling has already become the dominant cooling mechanism as one can see in Fig. 6.5 that shows the fraction of total cooling due to dust and gas radiative processes at each point of the post shock region. Fig. 6.4 shows the cooling rate path followed by the fluid as a function of temperature. Initially gas is very hot ($T \approx 5 \times 10^6$ K) and the cooling rate is high because dust is abundant and dust–electrons collisions are the main gas cooling mechanism. The cooling rate drops quickly but nonetheless the decrease of temperature brings the fluid closer to a temperature regime where radiative cooling becomes very efficient. In addition the gas density is enhanced earlier compared to the model where only radiative cooling operates (see Fig. 6.1). The combination of these effects markedly reduces the gas cooling time. In Fig. 6.7 we show how the dust size distribution is modified by dust sputtering. As one can see, the number of small grains is rapidly reduced compared to the bigger ones, in agreement with the findings of by Dwek et al. (1996).

In Fig. 6.8 we show the output spectra integrated along the whole radiative shock profile. The predicted $160\mu\text{m} - 70\mu\text{m}$ flux ratio is equal to 2.4, less than a half

of the FIR flux ratio observed in the SQ shock region ($F(160\mu\text{m})/F(70\mu\text{m}) \approx 6$). As shown in col.9 of Table 6.1, the FIR flux ratio values range between 0.4 and 3 but no models produce such a cold FIR color as we found for SQ shock region. In Table 6.1 we also report the width of the radiative zone (from the shock front until $T = 10^4$ K) and the total dust luminosity produced by a column of shocked material with unit cross section. In case of the model adopted for comparison with SQ shock region, the radiative zone width is ≈ 6 kpc, smaller than the characteristic widths of the SQ shock ridge. Multiplying the total luminosity per unit area ($\approx 1.5 * 10^{-4}$ erg/s/cm²) by the area of the shock region (≈ 330 kpc), we obtain $L(IR) = 4.7 \times 10^{41}$ erg/s. Therefore, in the simple picture where we are looking at the shock front face-on and behind each surface element on the sky there is an entire radiative region, the predicted collisionally heated dust luminosity would be about 30 times smaller than the observed one ($L(IR) \approx 1.5 \times 10^{43}$ erg/s). These results confirm that, in absence of additional sources of dust grains into the hot plasma, the bulk of the observed infrared emission from the shock region in SQ cannot be ascribed to collisionally heated dust emission.

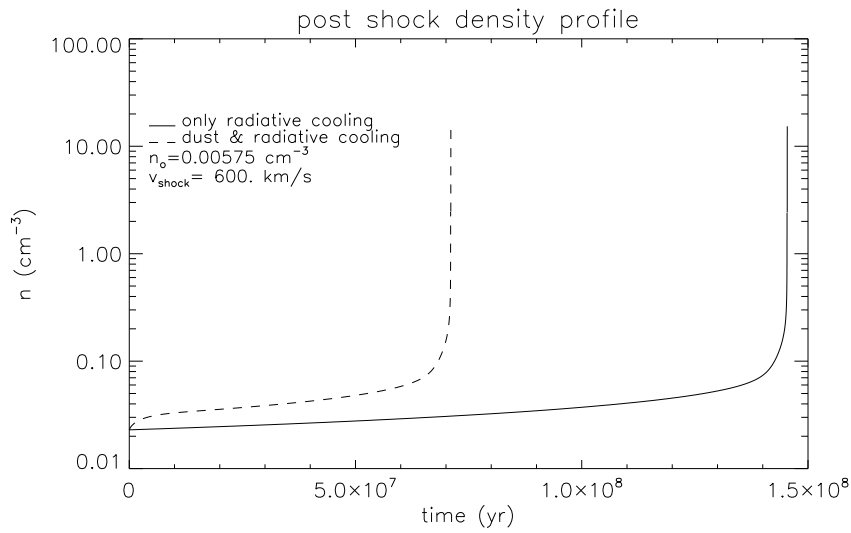


Figure 6.1: Post-shock density profiles in the two cases where dust cooling is included or not. The preshock parameters in this and the following figures are chosen to reproduce the physical conditions of the X-ray plasma in SQ in the region immediately downstream of the shock front.

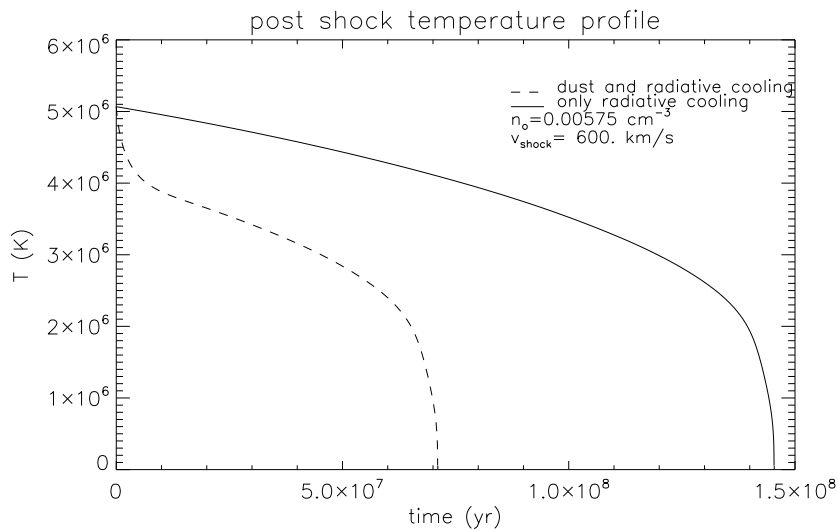


Figure 6.2: Post-shock temperature profiles in case dust and/or radiative cooling are included.

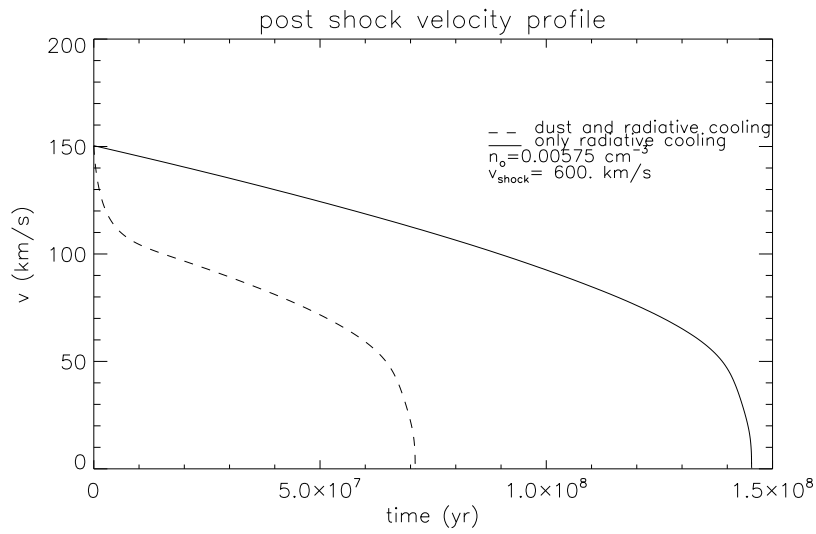


Figure 6.3: Post-shock velocity profiles in case dust and/or radiative cooling are included.

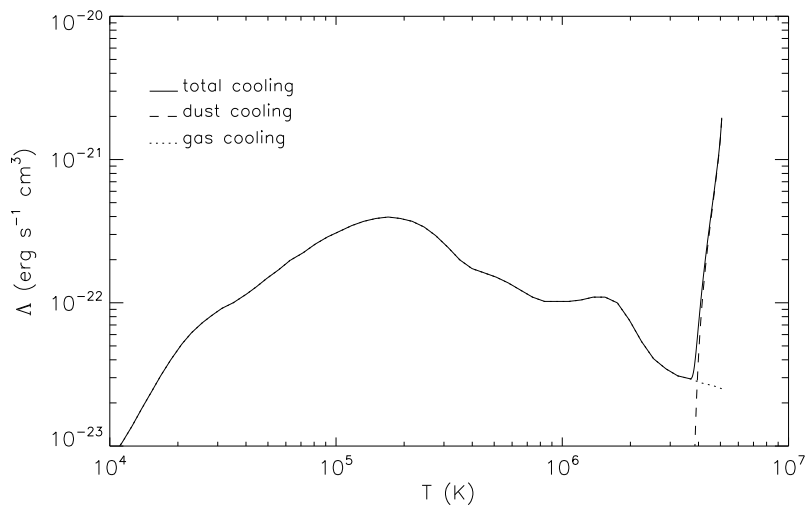


Figure 6.4: Cooling rate vs temperature for a shock model with $n_{H_0} = 0.01/4\text{cm}^{-3}$ and $v_s = 600 \text{ km/s}$. The contributions from dust and radiative cooling are plotted.

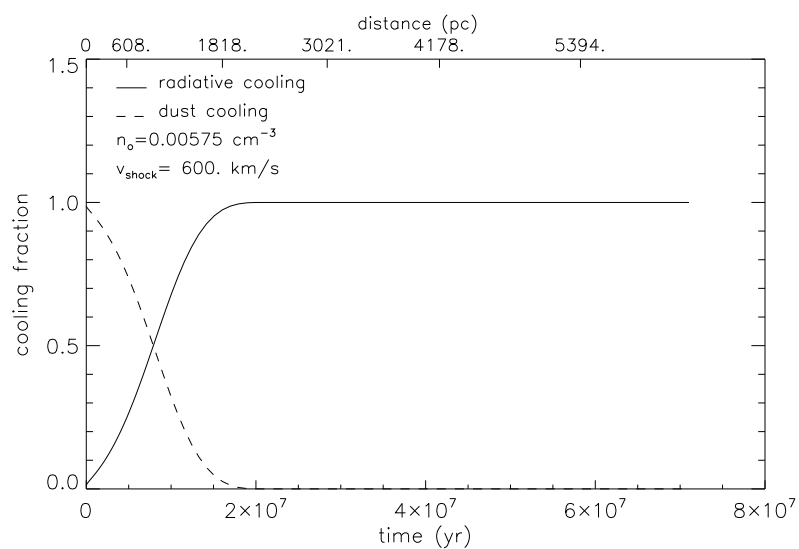


Figure 6.5: Dust and radiative cooling fraction as a function of time and distance from the shock front.

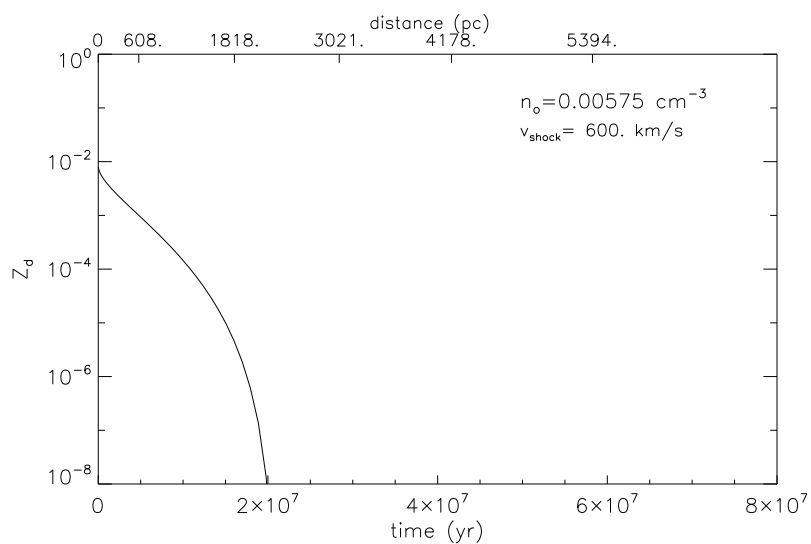


Figure 6.6: Dust to gas ratio profile in the post shock region

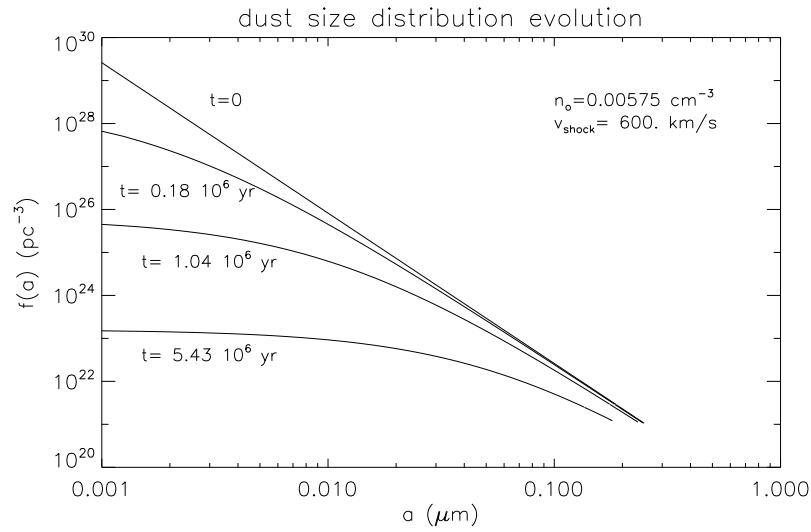


Figure 6.7: Dust size distribution when 0,20,50 and 90% of dust has been destroyed. The time corresponding to these phases is shown near each line.

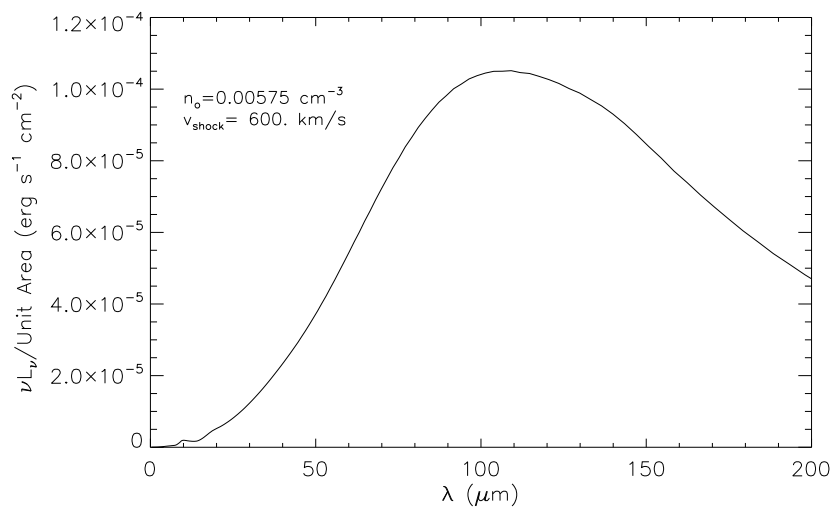


Figure 6.8: Total output dust luminosity from a column of post-shocked gas.

v_s	n_o	τ_{cool}^{rad}	$\tau_{cool}^{rad/dust}$	$\tau_{switch}^{rad/dust}$	$\tau_{nodust}^{rad/dust}$	Width	Lum	$\frac{F_{160}}{F_{70}}$	Λ_{dust}^{tot}
500.	0.00575	75.0	25.6	7.1	24.2	1.78	1.116	3.1	0.284
500.	0.01150	37.5	12.9	3.5	12.1	0.89	2.137	2.2	0.283
500.	0.02875	15.0	5.2	1.4	4.8	0.36	5.142	1.3	0.283
500.	0.05750	7.5	2.6	0.7	2.4	0.18	10.170	0.9	0.282
600.	0.00575	145.4	71.1	8.1	17.9	5.99	1.471	2.4	0.223
600.	0.01150	72.7	35.6	3.8	9.1	3.01	2.835	1.7	0.223
600.	0.02875	29.1	14.3	1.5	3.5	1.21	6.913	1.0	0.222
600.	0.05750	14.5	7.1	0.8	1.7	0.60	13.778	0.7	0.222
800.	0.00575	315.4	214.4	6.5	11.7	24.46	2.358	1.8	0.157
800.	0.01150	157.7	107.4	3.3	6.0	12.26	4.600	1.2	0.156
800.	0.02875	63.1	43.0	1.3	2.5	4.91	11.397	0.7	0.155
800.	0.05750	31.5	21.5	0.7	1.3	2.46	22.862	0.5	0.155
1000.	0.00575	530.9	386.5	6.0	12.7	55.73	3.493	1.5	0.121
1000.	0.01150	265.5	193.7	3.1	6.7	27.95	6.856	1.0	0.120
1000.	0.02875	106.2	77.6	1.3	1.9	11.22	17.066	0.6	0.119
1000.	0.05750	53.1	38.8	0.7	1.0	5.62	34.302	0.4	0.119

Table 6.1: Results from a grid of shock models. Col1: shock velocity (km/s); col2:pre-shock particle number density (cm^{-3}); col3: cooling time for models including only radiative cooling (10^6 yr); col4: cooling time for models including both dust and radiative cooling (10^6 yr); col5: time at which radiative cooling becomes predominant over dust cooling (10^6 yr); col6: time at which the dust to gas ratio is equal to 10^{-6} (10^6 yr); col7: Width of the radiative zone (from the shock front until $T = 10^4$ K) in models where both cooling mechanisms are included (kpc); col8: total shock output infrared luminosity per unit area (10^{-4}erg/s/cm^2); col9: predicted $160\mu\text{m}$ - $70\mu\text{m}$ flux density ratio from the radiative shock; col10: fraction of post-shock specific enthalpy plus specific kinetic energy radiated by dust

Summary and conclusions

In this work we have presented an extensive analysis of the infrared emission from Stephan's Quintet, based on the Spitzer MIR and FIR maps and including multi-wavelength data from optical/UV, Radio and X-ray (see Fig. 2.1). The main aim has been understanding the nature of the FIR dust emission seen on the Spitzer $70\mu\text{m}$ and $160\mu\text{m}$ maps and its implications for star formation and hot gas cooling for this galaxy group. The technical part of our analysis can be summarized in four points:

- 1) We have identified the FIR sources seen on the Spitzer FIR maps and extracted photometry for them from the MIR and FIR maps. The FIR photometry has been performed with a novel source fitting technique that we used to model the source emission on the maps (see Figs. 2.2 and 2.3). We measured MIR fluxes using aperture photometry (see Figs. 2.6 and 2.7). The inferred total flux densities are shown in Table 2.2.

- 2) We have created FIR residual maps, which were obtained from the FIR $70\mu\text{m}$ and $160\mu\text{m}$ maps after the subtraction of the two galaxies NGC7319 and NGC7320 and the discrete star formation regions. We have compared the emission on these maps with maps of the HI distribution, X-ray emission and UV emission (see Fig. 2.4). This comparison shows that the residual FIR emission, dominated by the emission from the shock region and a previously undetected extended component, is correlated with X-ray emission and anticorrelated with the HI distribution. At the same time, the area covered by the FIR residual emission is populated by an

extended distribution of UV sources associated with tidal features and intergalactic star formation regions. From the FIR residual maps we derived the photometry for the shock region and the extended component of emission. The fluxes associated with these components can be found in Table 2.2.

3) We have modelled the inferred infrared source SEDs using combinations of dust emission templates (see Figs. 3.1–3.5). These templates, described in Sect.3.2, are used to model the emission from PDR/HII regions, diffuse photon-powered dust emission, collisionally powered dust emission and infrared emission from the AGN torus. Among the immediate outcomes of the SED fitting procedure there are the dust mass required to produce the observed emission, the total dust infrared luminosity and the amount of UV powered dust emission (see Table 3.1).

4) Combining the amount of absorbed UV luminosity, obtained from the infrared SED fitting, with the observed UV luminosity, measured directly on the GALEX FUV maps, we determined the star formation rate for each dust emitting source (see Sect.4.2 for details). We also measured gas masses/column densities from the observed radio HI and CO lines and soft X-ray fluxes and, combining these measurements with the dust masses inferred from the infrared SED fits, we estimated the dust to gas ratios for several sources. Results are summarized in Table 4.1.

From morphological comparisons and the measurements obtained from map photometry and source SED fitting, together with simple predictions for the hot gas cooling time scale and the dust injection rate in hot plasma, we derived the following conclusions:

1) The total star formation rate, within a circular area of radius $90''$ containing the four group galaxies in close proximity, is $7.5M_{\odot}/yr$. The star formation regions in the group are localized at the edges of the galaxies, on tidal features and in the intergalactic medium; no evidences for star formation have been found towards galaxy centers. Although the location of star formation sites is very different from the case

of normal galaxies, the total star formation rate is of the same order of the values observed in nearby galaxies with the same stellar mass of SQ galaxies (see Sect.4.3).

2) The star formation efficiency for the star formation regions SQ A and SQ B, localized on tidal features, is close to that observed for star formation regions within nearby spiral galaxy disks (see Fig. 4.4). Star formation in HII-SE and HII-SW seems to be much more efficient but the lack of complete gas measurements and the possible contribution to UV radiation from radiative shocks doesn't allow a definite conclusion for these sources.

3) The star formation efficiency in the shock region seems to be consistent with the star formation observed in nearby spiral galaxies. However, because part of the distorted disk of the intruder galaxy NGC7318b is seen through the shock region, it is not clear if the observed star formation in that area is associated with the shocked gas or not. The observed radio-IR luminosity ratio is 20 times higher than the value predicted by the radio-infrared relation derived by Pierini et al. (2003), given the observed amount of infrared luminosity. This reinforces the result obtained by Xu et al. (2003), confirming that the acceleration of relativistic particles in the shock region is not associated with star formation.

4) 70% of the total star formation in SQ is associated with an extended component of FIR emission. The star formation efficiency for this component is rather higher than that observed in spiral galaxies. This could in principle be due to a new mode of star formation operating in the group and involving cooling of the X-ray halo gas, possibly enhanced by dust-plasma particle collisions. However the lack of cold molecular gas measurements associated with the extended emission makes this hypothesis difficult to check at the present time. In addition the evidence of tidal interactions and star formation in tidally displaced cold gas, like SQ A or SQ B, suggest that the distributed star formation observed in the group is in part occurring out of gas of galaxian origin.

5) For both the shock region and the extended emission we have measured substantial $8\mu\text{m}$ flux, which we take to be mainly due to PAH molecule line emission and, therefore, tracer of cold gas phases. This, together with simple estimates of the dust injection rate across the shock front and in the halo of the group, demonstrates that the mechanism powering most of the dust emission seen on the FIR residual maps is not dust collisional heating. However, given the high FIR–X-ray luminosity ratio, the current data do not exclude that the majority of the hot gas cooling can still be due to dust–plasma particle collisions rather than X-ray emission. For dust in the group halo we estimated that dust collisional heating can power up to 10^{42}erg/s of the dust luminosity.

6) We have found that the morphology of the FIR dust emission in the Seyfert 2 galaxy NGC7319 does not reflect the cold gas distribution. Therefore, the FIR emission in this galaxy is not obviously related to star formation. Given the AGN UV luminosity, estimated from the observed hard X-ray flux, and from considerations on the particular torus–galaxy disk geometry, we deduced that accretion powered radiation from the AGN, propagating through the disk of the galaxy, can power most of the observed dust infrared emission.

At the end of the thesis, we have presented a theoretical model of a 1D steady state shock including the effect of dust cooling and dust destruction by sputtering in hot plasmas. Given a broad range of initial gas densities and shock velocities (see Table 6.1), we have calculated post–shock profiles for several quantities, as the physical properties of the gas or the fraction of cooling provided by dust–plasma particle collisions, and compared the results with the case where dust cooling is not included. In particular, a model with post–shock parameters close to the observed gas properties in the SQ shock has been calculated (see Figs. 6.1–6.8). This model shows that, eventhough radiative cooling is still the most important cooling mechanism in terms of total radiated energy, the presence of dust reduces the cooling time by a factor ~ 2 . This effect is due to the accelerated cooling in the hot region ($T \sim 10^6\text{K}$) immediately downstream of the shock.

Future outlook

The photometry technique we applied on the Spitzer FIR maps of Stephan's Quintet has helped us to obtain information which are at the limits of what is reachable with Spitzer data. The higher sensitivity, resolution and the larger wavelength coverage of the Herschel space telescope will allow a much deeper investigation of the scientific problems we discussed in this thesis. The PACS instrument on Herschel will produce maps with an angular resolution of $5''$ and $12''$ at respectively $70\mu\text{m}$ and $160\mu\text{m}$, compared to $18''$ and $40''$ resolutions characteristic of the Spitzer MIPS instrument. This will have a dramatic effect for the FIR source photometry, considerably reducing the high level of confusion between sources that has pushed us to devise the FIR map fitting technique. In addition Herschel will provide images in the wavelength range $250\mu\text{m}$ - $500\mu\text{m}$ with the SPIRE instrument, mapping any cold dust emission component missed by Spitzer. Specifically, a future mapping of Stephan's Quintet with the Herschel observatory will allow to:

- 1) improve the FIR photometry for discrete star formation regions, as SQ A and SQ B. The photometry of these sources on Spitzer data is particularly hampered by the confusion problem because of the presence of nearby minor sources.

- 2) separate clumpy and diffuse components of dust emission in the shock region, associated with star formation regions and shocked gas. As we saw in Fig. 2.3, the map fitting technique applied on the $160\mu\text{m}$ map gave a strong hint for the presence of a linear north-south structure coincident with the shock ridge. This structure is not seen at MIR wavelengths and it will be important to verify its existence in

the FIR on the higher resolution Herschel maps. Because of the presence of huge amount of cold molecular gas in the shock region, recently detected by P. Guillard (private communication), cold dust emission is indeed expected from this area.

3) determine the origin of the extended FIR emission. The analysis we performed has shown that this emission is mainly connected with discrete star formation regions at the periphery of the galaxies or in intergalactic medium. It will be interesting to see if the Herschel maps will show a true diffuse component associated with the halo of the group.

4) verify that the FIR dust emission in the AGN galaxy NGC7319 is mainly powered by AGN radiation. As we proposed in Sect. 4.4, in this case we expect to see a cone structure in the nuclear dust emission, signature of the dust illumination by the AGN radiation preferentially escaping in the polar direction of the accretion disk.

5) better constrain the results of the source SED fitting. The possibility of integrating in the analysis photometric measurements longwards of $160\mu\text{m}$ will be of key importance to constrain dust masses. Also the properties of the radiation field and consequently the absorbed fraction of UV photons will be measured with higher accuracy with possible consequences on our understanding of star formation and gas cooling in this group.

The angular resolutions of the longest wavelengths covered by Herschel, with the SPIRE instrument, are comparable to those of the Spitzer FIR bands. Therefore one might say that in the Herschel era the source confusion problem in SQ will be shifted from $\sim 100\mu\text{m}$ to $\sim 350\mu\text{m}$. In this regard the map fitting technique we created can still be used for the photometry of sources at very long FIR wavelengths and also to identify FIR source counterparts on highest resolution multiwavelength data.

Finally our work motivates possible studies regarding the exact evolution of clumpy gas of galaxian origin involved in high velocity collisions on galactic scales.

From the observational point of view, multiwavelength studies of collisional events happening in other objects than Stephan's Quintet will surely be interesting. The "Taffy" galaxy pair (Condon et al. 1993, Jarrett et al. 1999, Zhu et al. 2007), for example, is a natural choice since the galaxies in that system were involved in an head-on collision which shocked their ISMs and created a bridge of cold gas between the galaxies. This object can be considered as representative of a later phase of a direct collision compared to the on-going collision in SQ. From the theoretical point of view, detailed hydrodynamical simulations of shocks in clumpy mediums taking into account chemical processes as the formation of molecular hydrogen, physical processes as the destruction of dust and the mixing of hot and cold gas due to cloud ablation, combined with radiation transfer calculations to determine the infrared emission produced by photon heated and collisionally heated dust, will be an important step to understand the complex evolution of gas shocked in intergalactic collisions and to interpret correctly the multiwavelength signatures tracing these events in the Universe.

Bibliography

Aoki, K., Kosugi, G., Wilson, A. S., Yoshida, M.,1999,ApJ,521,565

Appleton, P. N., Xu, Kevin C., Reach, W., Dopita, M. A., et al.2006,ApJ,639,51

Arp, H.,1973,ApJ,183,411

Bai, L., Rieke, G. H., Rieke, M. J.,2007,ApJ,668,5

Bell, E. F., Wolf, C., Meisenheimer, K., Rix, H.-W.,2004,ApJ,608,752

Bendo, G. J., Draine, B. T., Engelbracht, C. W., Helou, G., et al.2008,MNRAS,389,629

Bevington, P.R., Robinson, D.K. 1992, 'Data reduction and error analysis for the physical sciences', McGraw-Hill,Inc

Bigiel, F., Leroy, A., Walter, F., Brinks, E., et al.2008,AJ,136,2846

Blandford, R.,Eichler, D.,1987,Phys. Rep., 154, 1

Braine, J., Duc, P.-A., Lisenfeld, U., Charmandaris, V., Vallejo, O., Leon, S., Brinks, E.,2001,A&A,378,51

Brinchmann, J., Charlot, S., White, S. D. M., Tremonti, C.,2004,MNRAS,351,1151

Calzetti, D., Kennicutt, R. C., Engelbracht, C. W., Leitherer, C., et al.2007,ApJ,666,870

Cavaliere, A., Lapi, A.,2008,ApJ,673,5

Chelouche, D., Koester, B. P., Bowen, D. V., 2007, *ApJ*, 671, 97

Cluver, M. E., Appleton, P. N., Boulanger, F., Guillard, P., et al. 2010, *ApJ*, 710, 248

Colless, M., Dalton, G., Maddox, S., et al. 2001, *MNRAS*, 328, 1039

Condon, J. J., Helou, G., Sanders, D. B., Soifer, B. T., 1993, *AJ*, 105, 1730

Conti, P. S., Crowther, P. A., 2004, *MNRAS*, 355, 899

Dale, D. A., Bendo, G. J., Engelbracht, C. W., Gordon, K. D., et al. 2005, *ApJ*, 633, 857

Dekel, A., Birnboim, Y., 2006, *MNRAS*, 368, 2

Dolag, K., Meneghetti, M., Moscardini, L., Rasia, E., Bonaldi, A., 2006, *MNRAS*, 370, 656

Dopita, M. A., Groves, B. A., Fischera, J., Sutherland, R. S., et al. 2005, *ApJ*, 619, 755

Dopita, M. A., Sutherland, R. S., 1996, *ApJS*, 102, 161

Draine, B. T., Salpeter, E. E., 1979, *ApJ*, 231, 77

Dwek, E., 1987, *ApJ*, 322, 812

Dwek, E., Foster, S. M., Vancura, O., 1996, *ApJ*, 457, 244

Dwek, E., Rephaeli, Y., Mather, J. C., 1990, *ApJ*, 350, 104

Dwek, E., Werner, M. W., 1981, *ApJ*, 248, 138

Fazio, G. G., Hora, J. L., Allen, L. E., Ashby, M. L. N., et al., 2004, *ApJS*, 154, 10

Fischera, J., Dopita, M. A., 2008, *ApJS*, 176, 164

Fischera, J., Tuffs, R. J., Vlk, H. J., 2002, *A&A*, 395, 189

Fritz, J., Franceschini, A., Hatziminaoglou, E., 2006, *MNRAS*, 366, 767

Gallagher, S. C., Charlton, J. C., Hunsberger, S. D., Zaritsky, D., 2001, *AJ*, 122, 163

Gao, Y., Xu, C.,2000,ApJ,542,83

Giard, M., Montier, L., Pointecouteau, E., Simmat, E., 2008,A&A,490,547

Gordon, K. D., Engelbracht, C. W., Rieke, G. H., Misselt, K. A.,2008,ApJ,682,336

Green, D. A., Tuffs, R. J., Popescu, C. C.,2004,MNRAS,355,1315

Groves, B., Dopita, M. A., Sutherland, R. S., et al. 2008,ApJS,176,438

Guhathakurta, P., Draine, B. T.,1989,ApJ,345,230

Guillard, P., Boulanger, F., Pineau Des Forêts, G., Appleton, P. N.,2009,A&A,502,515

Helou, G., Roussel, H., Appleton, P., Frayer, D., et al. 2004,ApJS,154,253

Hickson, P.,1997,ARA&A,35,357

Huchra, J. P., Wyatt, W. F., Davis, M.,1982,AJ,87,1628

Ilbert, O., Salvato, M., Le Floch, E., Aussel, H., et al.,2010,ApJ,709,644

Jarrett, T. H., Helou, G., Van Buren, D., Valjavec, E., Condon, J. J.,1999,AJ,118,2132

Jog, C. J., Solomon, P. M.,1992,ApJ,387,152

Kauffmann, G., Heckman, T. M., White, S. D. M., Charlot, S.,et al.2003,MNRAS,341,33

Kennicutt, R. C., 1998,ARA&A,36,189

Kennicutt, R. C., Calzetti, D., Walter, F., Helou, G.,et al. 2007,ApJ,671,333

Kereš, D., Katz, N., Fardal, M., Davé, R., Weinberg, D. H.,2009,MNRAS,395,160

Kitayama, T., Ito, Y., Okada, Y., Kaneda, H. et al.2009,ApJ,695,1191

Leger, A., Puget, J. L.,1984,A&A,137,5

Lisenfeld, U., Braine, J., Duc, P.-A., Leon, S., et al. 2002, *A&A*, 394, 823

Mathis, J. S., Mezger, P. G., Panagia, N., 1983, *A&A*, 128, 212

Mathis, J. S., Rimpl, W., Nordsieck, K. H., 1977, *ApJ*, 217, 425

Micelotta, E. R., Jones, A. P., Tielens, A. G. G. M., 2010, *A&A*, 510, 37

Moles, M., Marquez, I., Sulentic, J. W., 1998, *A&A*, 334, 473

Montier, L. A.; Giard, M., 2004, *AAP*, 417, 401

Mulchaey, J. S., 2000, *ARA&A*, 38, 289

O'Sullivan, E., Giacintucci, S., Vrtilik, J. M., Raychaudhury, S., David, L. P., 2009, *ApJ*, 701, 1560

Osmond, J. P. F., Ponman, T. J., 2004, *MNRAS*, 350, 1511O

Pierini, D., Popescu, C. C., Tuffs, R. J., Völk, H. J., 2003, *A&A*, 409, 907

Popescu, C. C., Misiriotis, A., Kylafis, N. D., Tuffs, R. J., Fischera, J., 2000, *A&A*, 362, 138

Popescu, C. C., Tuffs, R. J., 2002, *MNRAS*, 335, 41

Popescu, C. C., Tuffs, R. J., Fischera, J., Völk, H., 2000 *A&A*, 354, 480

Quillen, A. C., Rieke, G. H., Rieke, M. J., Caldwell, N., Engelbracht, C. W., 1999, *ApJ*, 518, 632

Rasmussen, J., Ponman, T. J., Verdes-Montenegro, L., Yun, M. S., Borthakur, S., 2008, *MNRAS*, 388, 1245

Rieke, G. H., Young, E. T., Engelbracht, C. W., Kelly, D. M., et al., 2004, *ApJS*, 154, 25

Roncarelli, M., Pointecouteau, E., Giard, M., Montier, L., Pello, R., 2010, *A&A*, 512, 20

Salim, S., Rich, R. M., Charlot, S., Brinchmann, J., 2007, *ApJS*, 173, 267

Schlegel, D. J., Finkbeiner, D. P., Davis, M.,1998,ApJ,500,525

Smith, R. K., Krzewina, L. G., Cox, D. P., Edgar, R. J., Miller, W. W. III,1996,ApJ,473,864

Springel, V., White, S. D. M., Jenkins, A., Frenk, C. S. et al.2005,Natur,435,629

Stickel, M., Klaas, U., Lemke, D., Mattila, K.,2002,A&A,383,367

Stickel, M., Lemke, D., Mattila, K., Haikala, L. K., Haas, M.,1998,A&A,329,55

Struck, C.,2006,115,'Astrophysics Update 2', by John W. Mason, published by Springer Verlag

Sulentic, J.W., Rosado, M., Dultzin-Hacyan,D. et al. 2001, AJ, 122, 2993

Sutherland, R. S., Dopita, M. A.,1993,ApJS,88,253

Tielens, A. G. G. M., McKee, C. F., Seab, C. G.,Hollenbach, D. J.,1994,ApJ,431,321

Tran, K. H., Saintonge, A., Moustakas, J., Bai, L.,2009,ApJ,705,809

Trinchieri, G., Sulentic, J., Pietsch, W., Breitschwerdt, D. 2005 , A&A,444,697

van Gorkom, J. H.,'Clusters of Galaxies: Probes of Cosmological Structure and Galaxy Evolution', published by Cambridge University Press, edited by J.S. Mulchaey, A. Dressler, and A. Oemler, 2004, p. 305.

Vasudevan, R. V., Fabian, A. C., Gandhi, P., Winter, L. M., Mushotzky, R. F.,2010,MNRAS,402,1081

Verdes-Montenegro, L., Yun, M. S., Williams, B. A., Huchtmeier, W. K.,et al.2001,A&A,377,812

Voit, G. M.,2005,RvMP,77,207

Xu, C. K., Buat, V., Iglesias-Pramo, J., Takeuchi, T. T.,2006,ApJ,646,834

Xu, C. K., Sulentic, J.W., Tuffs,R.J. 1999,ApJ,512,178

Xu, C. K., Iglesias-Páramo, J., Burgarella, D., Rich, R. M. 2005,ApJ,619,95

Xu, C.K., Lu, N., Condon,J.J.,Dopita,M.,Tuffs,R.J. 2003, ApJ, 595, 665

York, D. G., Adelman, J., Anderson, Jr., J. E., et al.2000, AJ, 120, 1579

Williams, B. A., Yun, M. S., Verdes-Montenegro, L. 2002, AJ, 123, 2417

Wyder, T. K., Martin, D. C., Schiminovich, D.,2007,ApJS,173,293

Zhukovska, S., Gail, H.-P., Tieloff, M.,2008,A&A,479,453

Zhu, M., Gao, Y., Seaquist, E. R., Dunne, L.,2007,AJ,134,118

Zubko, V., Dwek, E., Arendt, R. G.,2004,ApJS,152,211

Table of abbreviations

AGN = Active galactic nuclei

BCD = Basic calibrated data

CIE = Collisional ionization equilibrium

DEC = Declination

DMH = Dark matter halo

FIR = Far-infrared

FWHM = Full width half maximum

HST = Hubble Space Telescope

ICM = Intracluster medium

IGM = Intergalactic medium

IRAC = Infrared Array Camera on the Spitzer Space Telescope

IRAS = Infrared Astronomical Satellite

ISM = Interstellar medium

ISO = Infrared Space Observatory

KS = Kennicutt-Schmidt (law)

Λ -CDM = Λ -Cold dark matter

MIPS = Multi-Band Imaging Photometer on the Spitzer Space Telescope

MIR = Mid-infrared

PAH = Polycyclic aromatic hydrocarbons

PDR = Photo-dissociation region

PSF = Point spread function

RA = Right ascension

SDSS = Sloan Digital Sky Survey

SED = Spectral energy distribution

SFR = Star formation rate

SQ = Stephan's Quintet

UV = Ultraviolet

Acknowledgments

Doing a PhD is a bit like climbing a mountain, with the difference that nobody can tell you before how tall the mountain is.... however, that was it! Done! After a lot of climbing you stop somewhere and realize you reached some place, whose height depends on many things, including the people you met during this “journey”.

It is my pleasure to thank my supervisor Dr. Richard Tuffs for all the things he taught me, especially the attitude to keep always an open mind, without accepting blindly what is believed by anyone else. I wish to thank the members of my examination committee: Prof. Werner Hofmann, Prof. Eva Grebel, Prof. Francois Boulanger and Prof. Christian Fendt. Christian, thanks for your support during all these three years.

I cannot count all the people I met during my PhD studies but I would like to thank all of them for having made my PhD a very enriching experience.

In particular I would like to thank my MPIK colleagues and friends: Brian, Olaf, Dave, Emma, Valenti, Mitya, Eva, Anne, Sabrina, Elisa, Iwona, Ioanna, Ellen, Ervin, Francesca, Claudine, Sirin, Martin, Markus, Yolanda, Gabi, Anna, Slavo, Andrew, Frank, Roland, Prof. Kirk, Prof. Völk, Prof. Kelner, Prof. Krätschmer, thanks everyone for the nice time at MPIK.

I thank the numerous officemates I had the pleasure (or the burden... :P) to share MY office with, in particular Lisa, Gabriela, Joerg, Meiert, Pol, Martina and Daniel.

I thank my Pfälzer str. 19 flatmates: Osvaldo, Marijana, Katha, Milena and Maud. Thanks for all the nice evenings and fun time together.

I thank the “Steffi–Music” band, with whom I had a great time rehearsing in Walldorf: Stephanie, Paco, Mike, Andy and Jochen. Thanks for everything you taught me about music and everything else.

I thank all the amazing people I met in schools and conferences. Thanks Ute for having hosted me in Granada and our very useful discussions. Thanks Pierre for our chats on THE group of galaxies, i.e. Stephan’s Quintet. Thanks Edita for your friendship, and all your emails of course...

I thank all the people I met in Heidelberg and that made my time in Germany so unique. Massimo, Baybars, Olga, Kelly, thank you for your friendship and for making me feel like at home all the time. Very special thanks go to Viviana, Claudia, Giulia, Giovanna, Sara, Isabel, Matteo, Jamie, Vivi, Federica, Teresa, Nicola, Denija, Stefano, Mark, Sophia, Leonard and all the other IMPRS students. It has been great to know all of you.

Finally, I thank my family and my friends in Italy: you are a continuous moral support for me and the great reason to go back to Caserta everytime.

Those who know me well know how important music is for me. Therefore, the only way I can conclude my PhD thesis is with a quote from a song. I chose this one: “Leggero, nel vestito migliore, senza andata né ritorno senza destinazione. Leggero, nel vestito migliore, sulla testa un po’ di sole ed in bocca una canzone” (from “Leggero”, Ligabue).